ISSN 2367-7570

Workshop
"Solar Influences on the Magnetosphere, Ionosphere and Atmosphere"

Book
of
Proceedings

Sixteenth Workshop

June, 2024

Organized by:
Space Research and Technologies Institute
Bulgarian Academy of Sciences

Editorial Board

Editors: **Katya Georgieva, Boian Kirov, Simeon Asenovski**

Acknowledgements

The Workshop’s organizers acknowledge the support by the Bulgarian National Science Fund, Grant No КП-06-МНФ/43, and the Bulgarian Academy of Sciences.

Scientific Organizing Committee

Katya Georgieva (Space Research and Technology Institute, Sofia, Bulgaria) – *Chair*
Atila Özgüc (Bogazici Univ. Kandilli Observatory, Istanbul, Turkey)
Crisan Demetrescu (Institute of Geodynamics, Romanian Academy)
Dragan Roša (Zagreb Astrronomical Observatory, Croatia)
Jean-Pierre Rozelot (Université Côte d’Azur)
Nat Gopalswamy (NASA Goddard Space Flight Center)
Olga Malandraki (IAASARS, National Observatory of Athens, Greece)
Petra Koucká-Knižová (Institute of Atmospheric Physics, Czech Republic)
Vladimir Obridko (IZMIRAN, Moscow, Russian Federation)

Preface

The Sixteenth Workshop "Solar Influences on the Magnetosphere, Ionosphere and Atmosphere" was held from June 3 to 7, 2024 in Primorsko, Bulgaria. 59 scientists from 14 countries participated in the workshop with 41 oral and 14 poster presentations. 16 papers are included in these Proceedings.

The Scientific Organizing Committee and the Editors of the Proceedings thank all the participants in the Workshop and the contributors to the Proceedings.

DOI: 10.31401/WS.2024.proc

CONTENT

Sun and Solar Activity

Solar Wind-Magnetosphere-Ionosphere Interactions

Instrumentation for Space Weather Monitoring

Solar Influences on the Lower Atmosphere and Climate

Data Processing and Modelling

Prediction of Solar Cycle 25 Using Simplex Projection Method: A Long-Term Analysis Based on F10.7

Gerceker K.[1], Kilcik A.[1]

[1]Akdeniz University, Institute of Science, Department of Space Sciences and Technologies
07070, Antalya, Turkiye, e-mail: kemalhangerceker@gmail.com

Abstract

This study aims to predict the amplitude and time of solar activity for the solar cycle 25 by applying the Simplex Projection method to the 27-day averaged 10.7 cm Solar Radio Flux (F10.7) data. For this purpose, F10.7 data from 1963 to 2019 (up to the end of Solar Cycle 24) were used, and the current values of the Solar Cycle 25 were excluded from the dataset. Consequently, the dataset consists of 746 points (approximately 700 months), with the first 460 points selected as the library set and the remaining 286 points as the prediction set. Simplex Projection is a method that analyzes the complexity and chaotic properties of dynamic systems and can generate predictions. Subsequently, it compares the data points in the prediction set with the library set for each embedding dimension, identifying similar points and producing forward predictions (i.e., similarities) according to the desired time to prediction (Tp). To obtain better predictions and partially eliminate unsuccessful ones, the Mean Absolute Error (MAE) was calculated between the observed first 71 data points of the current cycle (Solar Cycle 25). Predictions with an error of less than 15% were considered successful predictions. When evaluating successful predictions, a double-peaked pattern is expected for Solar Cycle 25. Accordingly, the first peak of solar activity for Solar Cycle 25 was observed around mid-2023, with the second peak, stronger than the first, anticipated to occur in early 2025 (January 2025), and the minimum of the next cycle expected in the middle or later stages of the year 2030 (July 2030). Finally, the effect of the initial conditions of the library set and the prediction set on the prediction performance is revealed.

Keywords: Solar activity; Solar cycle prediction; Space weather.

Introduction

The Sun can be defined as an active star considering its proximity to the Earth and this activity exhibits quasi-periodic behaviors. Various solar activity parameters/indicators (Sunspot Numbers (SSN), Sunspot Areas, Solar Flare (SF) Numbers, 10.7 cm Solar Radio Flux (F10.7), Coronal Mass Ejection (CME) Numbers and Speeds, Maximum Coronal Mass Ejection Speed Index (MCMESI), etc.) are used for tracking, temporal behavior. These structures/events are highly dynamic and affect life on Earth by changing the space around the Earth and space weather conditions. As of 2024, given the technological sophistication of civilization, the impact of space weather conditions on the Earth has become more important than in the past. Satellite systems, internet networks, electrical systems, and all technological and electronic systems used in every moment of life are extremely vulnerable to being affected by space weather. Therefore, it is critical to understand the Sun-Earth-Space Weather triangle and its interactions.

Understanding solar activity and making predictions for the future are directly related to the fate of our planet and the development of our civilization. One of the urgent problems in the research of Sun-Earth relations today is to analyze and predict the space weather caused by solar activity (Tlatov et al., 2017). Analyzing the nonlinearity/chaoticity of this relationship and related parameters is instructive for future predictions. From this point of view, a good prediction and understanding of the solar activity indices of the considered dynamical structure allows a more accurate presentation of the impact of space weather on the Earth and living life.

Solar radio flux at 10.7 cm (2800 MHz) is a very good indicator of solar activity (Tapping, 2013). This index, often abbreviated as F10.7, is one of the important representative records of solar activity. In addition, the F10.7 index is known to be very valuable in determining and predicting space weather. The measurement advantage of F10.7 is remarkable because it is not affected by atmospheric distortions. For example, observing sunspots can be a problem when the weather is cloudy and atmospheric conditions are challenging.

Although the indices of solar activity seem to follow a certain order/linearity, there is a disorder/chaos within the existing order and an order within this disorder. This situation is explained by "deterministic chaos". Therefore, it seems logical to try to predict the parameters of solar activity, which are dynamic and chaotic, based on linearity. The nonlinear approach has proven its capabilities in applications to chaotic (nonlinear) systems (Sugihara 1994; Maye et al., 2007; Tsonis et al., 2015) and a new method called Empirical Dynamic Modeling (EDM) and the Simplex Projection method based on EDM have made significant progress in such research (Sugihara et al., 2012; Deyle et al., 2013; Ye et al., 2015). EDM is an equation-free approach for modeling the nonlinear interaction of different variables of the same complex system. Therefore, it seems appropriate to use this approach to predict the solar activity parameters.

In this study, the chaotic nature and behavior of the 27-day average F10.7 data were investigated. Accordingly, the Simplex Projection method was used to predict the amplitude and time of Solar Cycle 25. The results and the performance of the prediction method as well as the importance of initial conditions/points are presented.

Data

In this study, 27-day average 10.7 cm Solar Radio Flux (F10.7) data were used. The F10.7 data were obtained from NASA-OMNIWeb (https://omniweb.gsfc.nasa.gov). The data from 1963 to the end of 2018 (the end of the solar cycle 24) were considered and the current values of the solar cycle 25 were excluded from the prediction dataset.

The data set consists of 746 points (approximately 700 months) and the first 460 points are selected as the library set and the remaining 286 points as the prediction set.

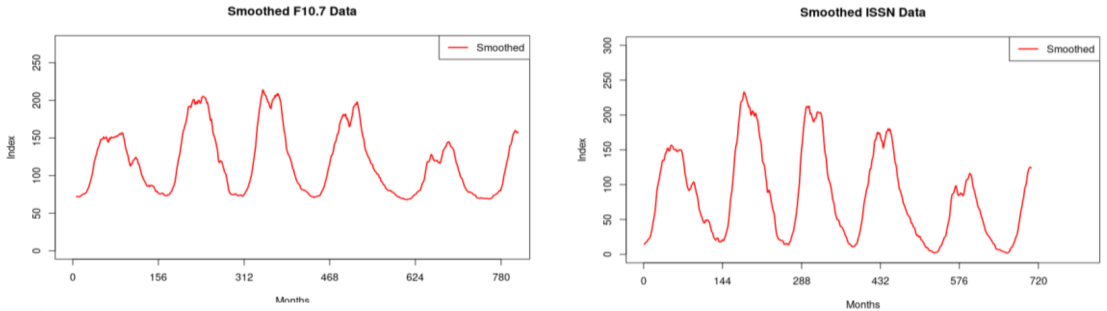

Figure 1. *Temporal variation of smoothed F10.7 (left panel) and smoothed SSN (right panel) for the last five cycles.*

As shown in Figure 1, both indicators show similar temporal variations.

SSN is a very advantageous data. Because, compared to other indicators, it has the oldest records (since the 1700s). F10.7, on the other hand, can be considered a short data set compared to SSN and others since its records started in 1963. Therefore, the fact that the data to be used for predicting is so limited and short-term should make us think about how the prediction performance will be for this data. If the prediction performance is confirmed in short-term data, it is thought that this will be an important finding for the used prediction method.

Methods

3.1. Simplex Projection

Simplex Projection is part of Empirical Dynamic Modelling (EDM) for analyzing nonlinear and chaotic systems developed by Sugihara. The method is used specifically to analyze time series data and predict future trends. It does this by using mathematical and geometric techniques to predict the future state from the past state of data.

The aim of EDM, and by extension Simplex Projection, is to reconstruct system dynamics from time series data. Time series are sequential observations of system behavior and therefore information about the rules governing system behavior (i.e. system dynamics) is hidden/embedded in the data. Takens Theorem (1981) expresses a way to recover this information using only a single time series.

$$X(t) = \{x(t), x(t-\tau), x(t-2\tau), \dots, x(t-(E-1)\tau)\} \quad (1)$$

Where X is a vector of the original state space, x is a sample in the time series t, τ (tau) is a time delay, and E represents the embedding dimension used to reconstruct the phase space.

The method proceeds as follows:

- First, the time series, i.e. the data, is placed/embedded in a phase space. This is made using the Takens Embedding Theorem. The state space is constructed accordingly. Takens embedding theorem is the reconstruction and representation of the state space of a dynamical system using time series data.
- Here, the method involves creating vectors that represent the state of the system for a given time after the phase space has been constructed. These vectors are generated using a given time delay (tau) and embedding dimension (E). This is called the embedding space.
- Next, in the embedding space, the nearest neighbors of the current state of the time series are identified. These neighbors are past states that were similar to the current state. This similarity is found by calculating the distances between the current vector of the state and all other vectors in the embedding space.
- In the last step, a projection (simplex) is created using similar neighbors. The weighted average of the distances of these similar neighbors is used to generate future values, i.e. predictions.

In simpler terms, the model created for F10.7 data looks at the past dynamics/states of the data, captures similarities, and produces predictions to predict future behavior.

3.2. Attractor Visualisation

The Simplex Projection method is known to be used for chaotic and non-linear time series and the solar activity indicators can be argued to meet this criterion. However, how does one know that F10.7 or any other data is non-linear and chaotic, or not too chaotic to make prediction possible? The attractor visualization helps with this and provides an understanding of the structure and nature of the time series.

This method is used to observe and analyze the trajectory of a dynamic system in state space. This visualization involves the projection of data from a time series onto a high-dimensional state space.

Attractor visualization is a technique used to understand the dynamic behavior of a time series. This technique aims to visually assess whether the time series has a chaotic or regular (patterned) structure.

Here, a two-dimensional (2D) attractor was used to verify this dynamic structure and to understand the chaotic nature of the system (see Figure 2).

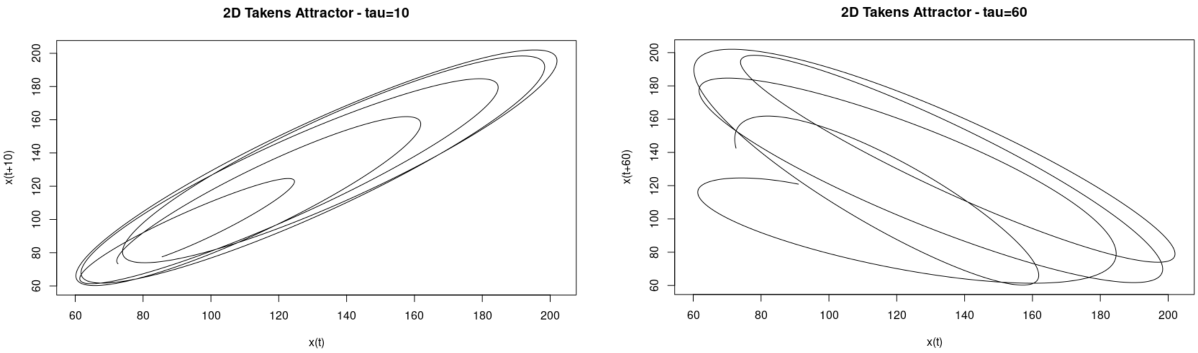

Figure 2. *Attractor Visualizations for F10.7 at 10 (left panel) and 60 (right panel) time delays.*

Although F10.7 was used for this analysis, unlike the prediction data, we used F10.7 data with low-pass filtering based on Fourier analysis (this also means moving the system from state space to frequency space). The reason for this is that the visualization is desired to be obtained with a clearer and more interpretable shape/structure.

Attractor results reveal the chaotic structure of F10.7. The circular features visible especially for 10 reveal the chaotic nature of the system. For 60, there are parallel stripes and this appearance reveals that the chaoticity is high. In the analysis, the aim is only to understand the nature and behavior of the system/data. Therefore, perhaps tau 60 and around may be an appropriate value for the original data and the prediction model.

Results

4.1. Prediction Results

The Simplex Projection method was used to generate predictions for each embedding dimension (E, ranging from 2 to 8) at various time delays. There were multiple successful predictions at varying time delays for various embedding dimensions.

Mean Absolute Error (MAE) was used as a success criterion and the first 71 known points of Solar Cycle 25 were compared with the first 71 points of the predictions. Predictions were considered successful if the MAE was below 15%.

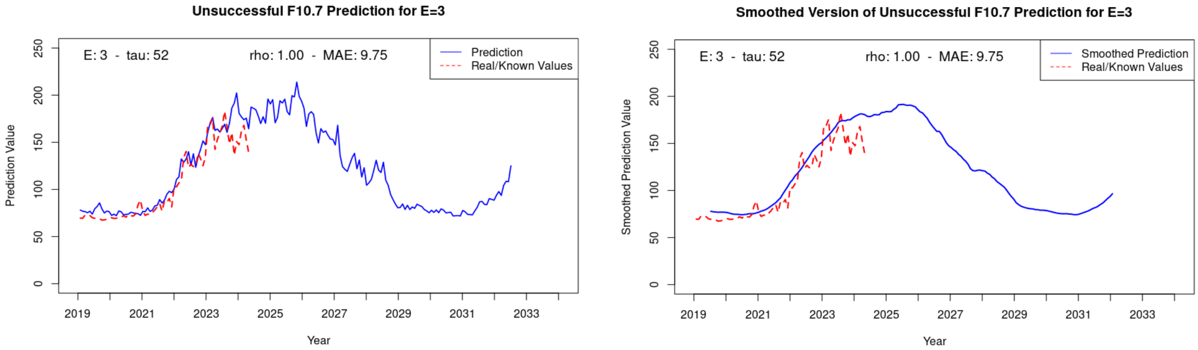

***Figure 3.** Original prediction (left panel) and smoothed version (right panel) of F10.7 with optimal tau (52) at embedding dimension E=3.*

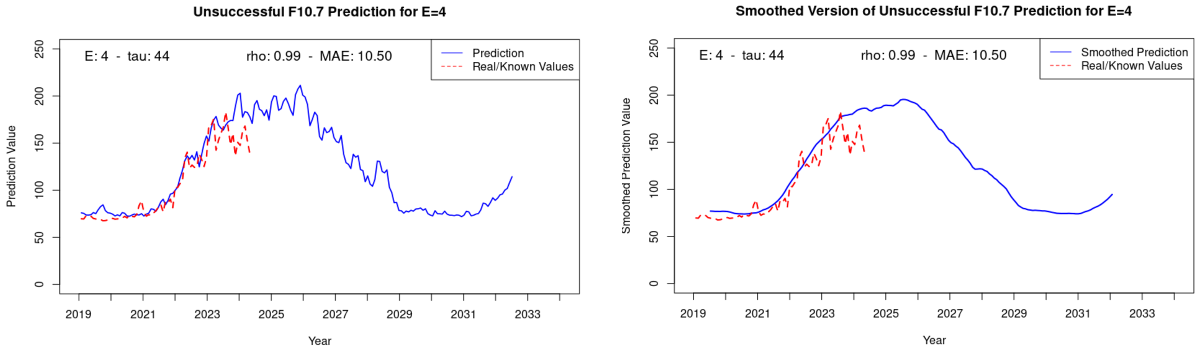

***Figure 4.** Original prediction (left panel) and smoothed version (right panel) of F10.7 with optimal tau (44) at embedding dimension E=4.*

Figures 3 and 4 show the most successful prediction results for different embedding dimensions. As can be seen, these results are similar to each other. However, it should be noted that when evaluating the results, the focus is mostly on E=3 and E=4. This is because higher embedding dimensions (such as E=6-7-8-9) are impractical for short data sets. With limited data, as the embedding dimension increases, the system dynamics are over-analyzed and the results become smoother.

For the predicted amplitude and times of maximum for Solar Cycle 25:

1. Solar Cycle 25 is expected to be stronger than Solar Cycle 24.
2. Predictions indicate that a double peak structure is more likely for Solar Cycle 25.
3. The first peak of solar activity for Solar Cycle 25 was observed around mid-2023. The second peak, which is expected to be stronger than the first one, is predicted in the early months of 2025 (January 2025). The end of the cycle/starting of the next cycle is predicted in mid-2030 (July 2030).

4.2. Adherence of model sets to initial conditions/points and unsuccessful predictions generated to demonstrate this

Chaos theory studies dynamical systems that are extremely sensitive to initial conditions. In chaotic systems, small changes in initial conditions can lead to large changes in the future behavior of the system.

In chaotic systems and models, the importance of the starting point of the prediction (or the end point of the data set) is known. While generating the predictions in this study, it was observed that the prediction performance does not only depend on the starting point of the prediction. The library set and the points where the prediction set starts and therefore ends are also important for the prediction performance.

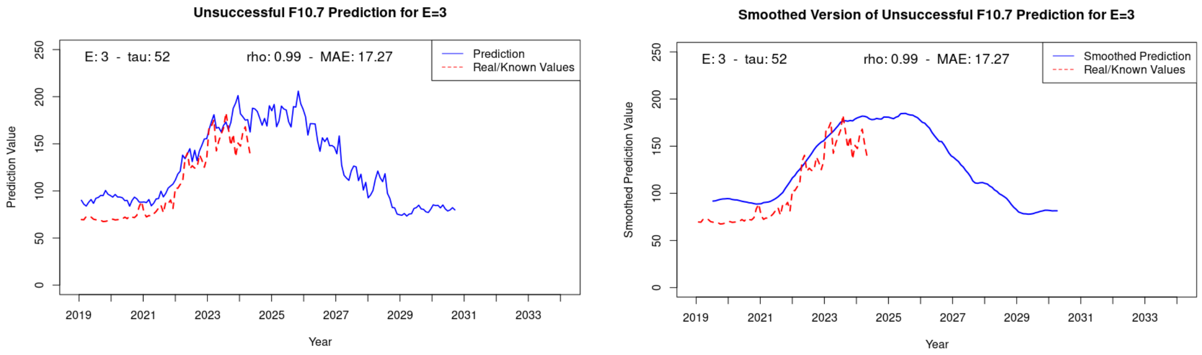

Figure 5. *Original (left panel) and smoothed version (right panel) of unsuccessful F10.7 prediction with non-optimal initial/starting point of sets with embedding dimension E=3.*

As can be seen in Figure 5, an unsuccessful prediction was produced. It should be noted that the same parameters were chosen for this prediction as for the successful prediction in Figure 3 (tau=52 for E=3). The reason for the unsuccessful prediction is that only one condition was changed: The point where the library set ends and the prediction set starts.

In Section 2, it was stated that the data set consisted of 746 points, the first 460 points were the library set and the remaining 286 points were the prediction set. For the unsuccessful prediction, this condition was changed and the sets were shifted. Accordingly, the optimal parameters from the successful prediction were taken, but the library set was set to 400 and the prediction set to 346. In other words, the last 60 points of the library set were shifted and added to the prediction set.

This case for the effect of the initial conditions of the sets on the prediction performance reveals an important fact. This can be seen in Figure 5, especially at the beginning (ascending phase) and at the end (descending phase) of the cycle prediction. There is an upward shift in amplitude in these regions. Also, on closer inspection, there is a downward shift in the center of the cycle (at maximum). The increase in the MAE (almost 10%) demonstrates this theoretically. As a result, the importance of the initial and end conditions of the data sets is thus revealed and specified.

Conclusion and Discussion

In this study, the Simplex Projection method is used to predict the amplitude and time of maximum for Solar Cycle 25. In addition, the initial conditions for the sets are analyzed and presented.

The findings of the study are as follows:

- Our predictions indicate that Solar Cycle 25 will be stronger than Solar Cycle 24.
- The predictions suggest that a double-peak maximum is more likely for Solar Cycle 25. The second peak of Solar Cycle 25, which is expected to be stronger

than the first, is predicted to occur in the early months of 2025 (January 2025), while the end of the Solar Cycle 25 is predicted to occur in the mid-2030s (July 2030).

- The success of the prediction directly depends on the initial condition/point of the sets. Changes in the initial and end points of the sets can significantly change the prediction. Therefore, it is very important to choose the optimal initial point.

In chaotic systems, the importance of the point where the prediction starts (or the point where the data set ends) is known when creating a model and obtaining a prediction. The importance of the initial/starting point of the prediction for solar activity data was first shown by Sarp, V. et al. (2018) using Simplex Projection. In our study, in addition to this finding for initial conditions, we revealed the sensitivity of the start and end points of the sets to the model and prediction. In addition, in the mentioned study in 2018, it was aimed to find the time and amplitude of Solar Cycle 25 using SSN and in parallel with our findings, it was predicted that Solar Cycle 25 would be stronger than Solar Cycle 24 with its double peak structure.

Simplex Projection (referred to as the Sugihara-May algorithm) was first applied to solar activity data by Kilcik et al. (2009). They predicted the amplitude and time of Solar Cycle 24 as of December 2012 with 87 sunspot units and first presented a successful example of the method.

The success of the Simplex Projection approach in nonlinear chaotic systems is demonstrated by its successful prediction performance for the relatively limited F10.7 data (approximately 700 months of data). Remarkably, this approach can obtain accurate predictions without the need for large amounts of data (e.g. more than 10 cycles).

Studies in the literature and various methods have been used for many years and can be considered successful. In this paper, we argue that the Simplex Projection approach is an alternative, for good prediction of solar cycle. Besides the advantages of the F10.7 data and its good representation of solar activity, we chose this data because it is limited data. The performance and success of the method are demonstrated by making a one-cycle prediction from only five cycles of information. In the future, we plan to continue prediction studies by improving both the method and our perspective.

Acknowledgements

This work was supported by Project 124N011 awarded by the Scientific and Technological Research Council of Turkey. All data used in the study were taken from the NASA-OMNIWeb (https://omniweb.gsfc.nasa.gov) database, and we are gratefully acknowledged. We would also like to thank the Bulgarian Academy of Sciences for their partial support.

References

Deyle, E. R., Fogarty, M., Hsieh, C. H., Kaufman, L., MacCall, A. D., Munch, S. B., ... & Sugihara, G. (2013). Predicting climate effects on Pacific sardine. Proceedings of the National Academy of Sciences, 110(16), 6430-6435.

Kilcik, A., Anderson, C. N. K., Rozelot, J. P., Ye, H., Sugihara, G., & Ozguc, A. (2009). Nonlinear prediction of solar cycle 24. The Astrophysical Journal, 693(2), 1173.

Maye, A., Hsieh, C. H., Sugihara, G., & Brembs, B. (2007). Order in spontaneous behavior. PloS one, 2(5), e443.

Sarp, V., Kilcik, A., Yurchyshyn, V., Rozelot, J. P., & Ozguc, A. (2018). Prediction of solar cycle 25: a non-linear approach. Monthly Notices of the Royal Astronomical Society, 481(3), 2981-2985.

Sugihara, G. (1994). Nonlinear forecasting for the classification of natural time series. Philosophical Transactions of the Royal Society of London. Series A: Physical and Engineering Sciences, 348(1688), 477-495.

Sugihara, G., May, R., Ye, H., Hsieh, C. H., Deyle, E., Fogarty, M., & Munch, S. (2012). Detecting causality in complex ecosystems. science, 338(6106), 496-500.

Takens, F. (2006, October). Detecting strange attractors in turbulence. In Dynamical Systems and Turbulence, Warwick 1980: proceedings of a symposium held at the University of Warwick 1979/80 (pp. 366-381). Berlin, Heidelberg: Springer Berlin Heidelberg.

Tapping, K. F. (2013). The 10.7 cm solar radio flux (F10. 7). Space weather, 11(7), 394-406.

Tlatov, A. G., Shramko, A. D., Chernov, Y. O., Strelkov, M. A., & Naga Varun, E. (2017). Space weather parameters: Modeling and prediction from the data of groundbased observations of solar activity. Geomagnetism and Aeronomy, 57, 854-858.

Tsonis, A. A., Deyle, E. R., May, R. M., Sugihara, G., Swanson, K., Verbeten, J. D., & Wang, G. (2015). Dynamical evidence for causality between galactic cosmic rays and interannual variation in global temperature. Proceedings of the National Academy of Sciences, 112(11), 3253-3256.

Ye, H., Beamish, R. J., Glaser, S. M., Grant, S. C., Hsieh, C. H., Richards, L. J., ... & Sugihara, G. (2015). Equation-free mechanistic ecosystem forecasting using empirical dynamic modeling. Proceedings of the National Academy of Sciences, 112(13), E1569-E1576.

The Backreaction of the Reduced Heliospheric Pressure on CMEs and Its Implications for the Strength of Solar Cycle 25

Gopalswamy N.[1], *Akiyama S.*[1,2], *Yashiro S.*[1,2], *Mäkelä P.*[1,2], *Xie H.*[1,2], *Michalek G.*[3]

[1]NASA Goddard Space Flight Center, Maryland, USA; nat.gopalswamy@nasa.gov
[2]The Catholic University of America, Washington DC, USA
[3]Jagiellonian University, Krakow, Poland

Abstract

We investigated the abundance of halo coronal mass ejections (CMEs), solar flares, and solar wind conditions that occurred during the first 49 months of solar cycles 23-25. We find that the halo CME abundance has an inverse relation with the solar cycle strength. The reduced heliospheric total pressure, whose backreaction on CMEs allows them to expand more, resulted in the higher halo CME abundance in the weaker cycle 24. This trend continues in cycle 25, indicating that this cycle is also weak. Related effects in weaker cycles are the wider longitudinal distribution of halo CME sources and the halo formation closer to the Sun at lower CME speeds. The size of soft X-ray flares is similar and the flare abundance is not significantly different in the three cycles, indicating that the weakened state of the heliosphere affects CMEs, but not flares. These results imply that cycle 25 is weaker than cycle 23 but similar in strength to cycle 24.

Keywords: Heliospheric pressure; Halo coronal mass ejections; Solar cycle prediction.

Introduction

The backreaction of the heliospheric pressure on the properties of coronal mass ejections (CMEs) was first recognized as the anomalous expansion of CMEs during the maximum phase of solar cycle (SC) 24 (Gopalswamy et al. 2014). While the width and speed of CMEs were well correlated as in SC 23, the slope of the speed-width relationship significantly increased in SC 24. The heliospheric backreaction has been found to manifest in many ways, including (i) enhanced halo CME abundance (Gopalswamy et al. 2015a: Dagnew et al. 2020a), (ii) halo formation closer to the Sun at lower CMEs speeds (Gopalswamy et al. 2022), (iii) wider longitudinal distribution of halo CMEs (Gopalswamy et al. 2015), (iv) change in slope of the CME expansion speed – CME radial speed relationship (Dagnew et al. 2020b), and (v) larger pressure balance distance for CME flux ropes (Gopalswamy et al. 2015b; Dagnew et al. 2022). The current SC 25 is in its maximum phase and has witnessed a significant number of CMEs in the first 4 years since its beginning in December 2019, providing an opportunity to test the heliospheric backreaction on CMEs and assess the strength of the cycle. Such an assessment is important in discriminating the widely varying predictions of the strength of SC 25 that vary from a sunspot number of 50 to >200 (Nandy 2021). Furthermore, using SC 25 data is important in confirming the results obtained by comparing just two SCs. In this paper, we revisit the properties of halo CMEs that occurred during SCs 23-25 and show that SC 25 is indeed weak, similar to SC 24 but slightly stronger (Gopalswamy et al. 2018; 2022; Bhowmik et al. 2018). Therefore, the space weather in SC 25 is expected to be milder than in SC 23.

Halo CME Observations

Halo CMEs observed by a given coronagraph discriminate energetic CMEs that expand rapidly early on, so they appear to surround the occulting disk (Howard et al. 1982; 1985; Zhao and Webb 2003; Gopalswamy et al. 2010). Halo CMEs are key players in space weather owing to their high energy and their direction of propagation close to the Sun-Earth line (Gopalswamy 2009; Zhang et al. 2021; Gopalswamy 2022). We make use of the halo CMEs manually identified, cataloged, and made available online at NASA’s CDAW Data Center (https://cdaw.gsfc.nasa.gov) with added information from the general CME catalog (Yashiro et al. 2004; Gopalswamy et al. 2009; 2024). Halo CMEs are identified in the coronagraph images obtained by the Large Angle Spectrometric Coronagraphs (LASCO, Brueckner et al. 1995) on board the Solar and Heliospheric Observatory (SOHO, Domingo et al. 1995).

Comparing halo CMEs in SCs 23 and 24 up to the maximum phase, Gopalswamy et al. (2015a) found that the halo CME abundance was higher in SC 24, even though the average sunspot number (SSN) declined by ~40%. The halo CME abundance was defined as the number of halo CMEs observed over a certain time interval divided by the daily SSN averaged over the same interval. Dagnew et al. (2020a) compared halo CMEs over the whole SCs 23 and 24 and confirmed the increase in halo CME abundance by ~44%, while the average SSN declined by ~46%. Here we compare the halo CME abundance over the first 49 months of SCs 23-25. The halo CME catalog (https://cdaw.gsfc.nasa.gov/, Gopalswamy et al. 2010) lists more than 800 halos since 1996. Figure 1 shows the semiannual variation of the number of halos in comparison with SSN. We see that the halo CME variation is in phase with the SSN variation, but the amplitudes are quite different. Such variation has also been found in the general population of CMEs as well (Petre 2015; Michalek et al. 2019). There were 100, 137, and 144 halos observed during the first 49 months of SCs 23, 24, and 25, respectively. We compare these numbers with respect to the average SSNs during these intervals.

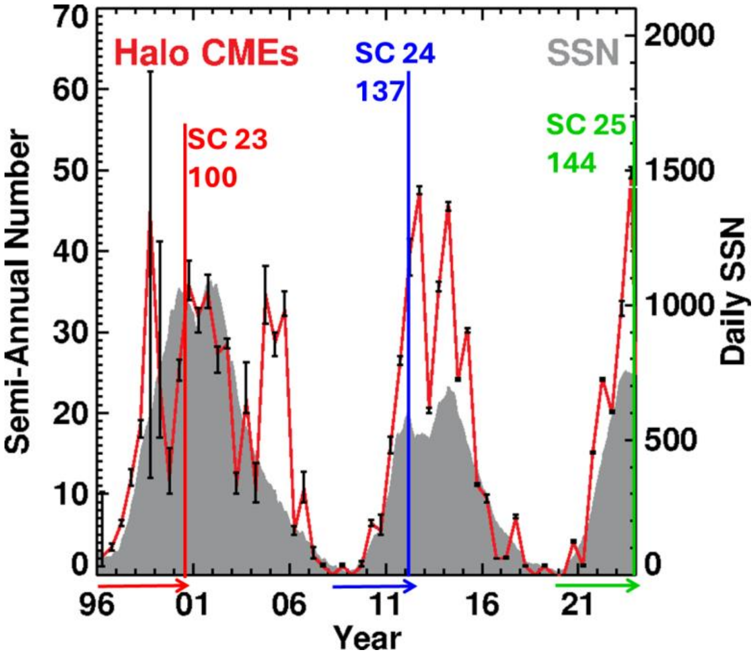

***Figure 1**. Semi-annual variation of the number of halo CMEs as a function of time since 1996 until the end of 2023. The daily SSN from SILSO (Sunspot Index and Long-term Solar Observations, **http://www.sidc.be/silso**) is shown for comparison. The arrows marked at the bottom of the plot indicate equal time intervals (49 months) from the beginning of each SC. The number of halos observed in these intervals are noted on the plot. The error bars are based on the data gaps in SOHO/LASCO observations.*

a. Halo CME abundances

Table 1 summarizes the number of halos, the halo CME abundance, and the percentage changes during the first 49 months in each SC. In SC 23, there were 100 halos. There was a 4-month data gap in SC 23 (3 months in 1998 and 1 month in 1999), so the 100 halos actually occurred in 45 months with an average rate of ~2.22 halos per month. If halos occurred at this rate during the data gap as well, we expect ~9 additional halos, yielding a total of ~109 halos during the first 49 months of SC 23. The number of halos in SCs 24 and 25 are 26% and 32% higher than the SC 23 number. During the first 49 months, the average sunspot number (<SSN>) decreased by 42% and 27% in SCs 24 and 25, respectively with respect to SC 23. Normalizing the number of halos to <SSN>, we get halo CME abundances of 1.32, 2.87, and 2.38 in SCs 23, 24, and 35 respectively. Clearly, the halo abundance is much higher in SCs 24 and 25, approximately doubling in SCs 24 (117% increase) and 25 (80% increase). Furthermore, the SC 25 halo abundance is in between SCs 23 and 24 but closer to SC 24.

b. Halo CME source locations

Figure 2 plots the heliographic coordinates of the source regions of the halo CMEs in SCs 23-25. Most halo CMEs originate from the latitude range 15°-30° in each hemisphere, which corresponds to the active region belt. This is because large amounts of free energy can be stored in the magnetic regions in the active region belt that can power the halo CMEs. There are no major differences in the latitudinal distributions in the three cycles. However, we see significant differences in the longitudinal distributions, which are much wider in SCs 24 and 25 than in SC 23. For example, the SC 23 data points (red) are generally concentrated close to the disk center, while the SC 24 (blue) and SC 25 (green) data points can be found in almost all longitudes. Halos originating from large central meridian distance are an indication that CMEs expand more in weaker cycles and hence increases their chance of becoming a halo (Gopalswamy et al. 2020b).

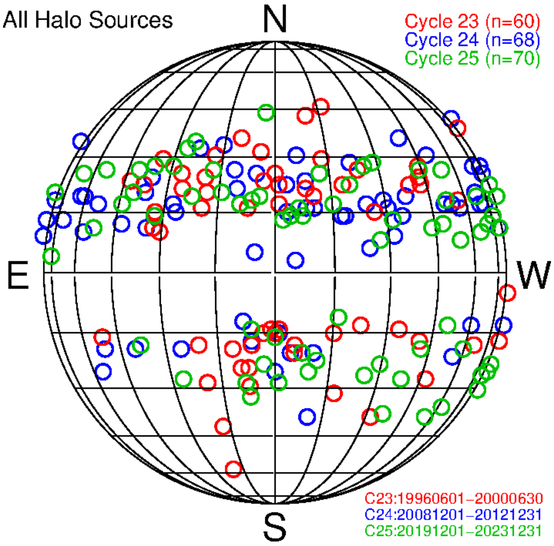

Figure 2. *Sources of halo CMEs during the first 49 months in SCs 23-25, distinguishing the cycles by different colors as indicated in the plot. No correction is made for the B0-angle of the source locations.*

Table 1. *Number of halos in the first 49 months of SCs 23-25 and <SSN>*

	SC 23	**SC 24**	**SC25**
Total number of halos	109	137 (+26%)	144 (+32%)
<SSN>	82.7	47.8 (-42%)	60.5 (-27%)
#halos/<SSN>	1.32	2.87 (+117%)	2.38 (+80%)

Figure 3 shows halo CMEs originating close to the limb in the three SCs. Here we have also included CMEs that originated slightly behind the limb (within 30°). There were only 6 limb halos in SC 23. In SC 24, there were 28 limb halos, about 5 times more than the number in SC 23. In SC 25, there were 20 limb halos, which is about 3 times the number in SC 23. Here also, we see that the strongest cycle has the lowest number and the weakest cycle has the largest number of limb halos. If we consider just the frontside events, there were 4, 17, and 15 limb halos in SCs 23, 24, and 25, respectively. This means, only ~7% (or 4/60) of SC 23 halos were at CMD >60°, which is much smaller than the 25% (17/68) in SC 24 and 21.4% (15/70) in SC 25. Once again, SCs 23 and 24 represent extremes, while SC 25 represents intermediate cases but closer to the SC 24 events.

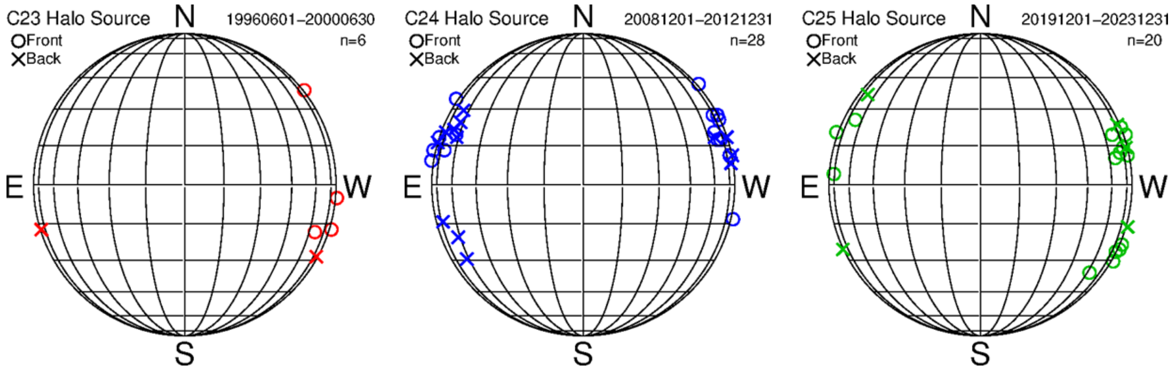

Figure 3. *Sources of halo CMEs during the first 49 months in SCs 23-25, distinguishing the cycles by different colors as indicated in the plot. No correction is made for the B0-angle of the source locations. Backside and frontside halos are indicated by crosses and circles, respectively.*

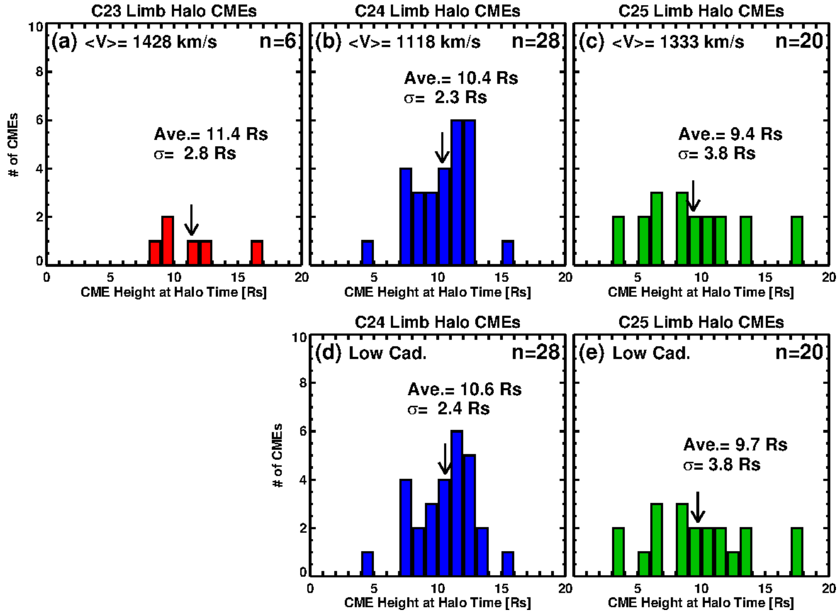

Figure 4. *Halo height distributions obtained from limb halos observed during the first 49 months in SCs 23-25. Halos in Fig. 3 are used for computing the halo heights. The mean (Ave.) and standard deviation (σ) of the distributions are given for each distribution. Also shown are the average speeds of the limb halos.*

c. Height of halo formation

The large number of halo CMEs originating close to the limb were used to determine the height attained by CMEs before becoming a halo (Gopalswamy et al. 2020b). This height, called halo height, was found to be smaller for the weaker SC 24 than for SC 23. This suggests that halos formed closer to the Sun at lower speeds in SC 24, another indication of the backreaction of the weak heliosphere on CMEs. In our previous study we used halos from the first 3 years of each cycle, so the sample sizes were small (Gopalswamy et al. 2023). Here we use an additional 12 months of data, increasing the sample size. We see a similar pattern when the halo heights for the first 49 months are compared in SCs 23-25: halo heights are smaller in SCs 24 and 25 than in SC 23. Furthermore, the average speed of limb halos is the highest in SC 23, followed by SC 25 and SC 24. Here also, SC 25 speed is intermediate between the SC 23 and SC 24 values.

d. Flare sizes in solar cycles 23-25

Figure 5 compares the limb flare sizes during the first 49 months of SCs 23-25. All flares with soft X-ray flare class ≥C3.0 originating within 30º from the limb are considered. All these flares associated with CMEs, but not necessarily halos. The number of flares declined in SCs 24 and 25 with respect to SC 23, but the reduction is not to the same extent as the SSN. When normalized to <SSN>, the number of flares become 2.19, 2.47, 2.51, respectively in SCs 23-25. Interestingly, these values are close to each other unlike the number of halos normalized to <SSN>. Furthermore, the average flare sizes are about the same in the three cycles. These observations suggest that the flares are not affected by the heliospheric state because the flare structures are anchored to the Sun while the CMEs propagate into the heliosphere and face the backreaction.

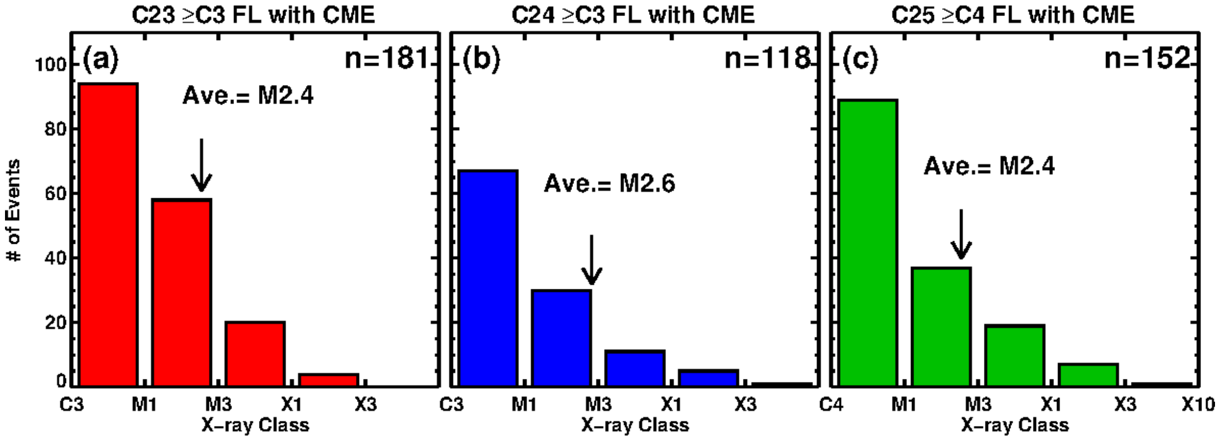

Figure 5. *Distributions of soft X-ray flare sizes reported by NOAA's Space Weather Prediction Center in SCs 23-25. Only flares associated with CMEs are considered. The means of the distributions are shown on the plots (Ave., pointed by arrows). For Cycle 25, ≥C4.0 flares are considered as opposed to ≥C3 flares in SCs 23 and 24. This is because, of rescaling of GOES data, which makes C4 level in SC 25 equivalent to C3 class to be on par with SC s 23 and 24. Details can be found in https://hesperia.gsfc.nasa.gov/goes/goes.html.*

e. Comparison of the number of intense space weather events

Earlier studies indicated that the number of intense space weather events declined significantly in SC 24 relative to SC 23, more than the decline in SSN (Gopalswamy et al. 2014; 2015b, c). Here we compare the intense space weather events during the first 49 months in SCs 23-25 (see Table 2). Intense space weather events we consider are ground level enhancement (GLE) in solar energetic particle events and intense geomagnetic storms (Dst ≤ -100 nT). The decline of intense space weather events is much steeper than that of <SSN>. The explanation for the reduction in the number of GLE events has been attributed to the reduction in ambient magnetic field strength in weaker cycles (Gopalswamy et al. 2014) because the acceleration efficiency is proportional to the ambient field strength. The geomagnetic storms are caused by southward component of the magnetic field in the CME sheath and/or in the magnetic cloud. The anomalous expansion dilutes the magnetic content of the CME and hence results in weaker storms (Gopalswamy et al. 2015c; Yermolaev et al. 2022).

***Table 2**. Intense space weather events during the first 49 months of SCs 23-25*

Parameter	SC 23	SC 24	SC 25
Dst ≤ -100 nT	26	9 (-65%)	6 (-77%)
GLEs	4	1 (-75%)	1 (-75%)
SSN	82.7	47.8 (-42%)	60.5 (-27%)

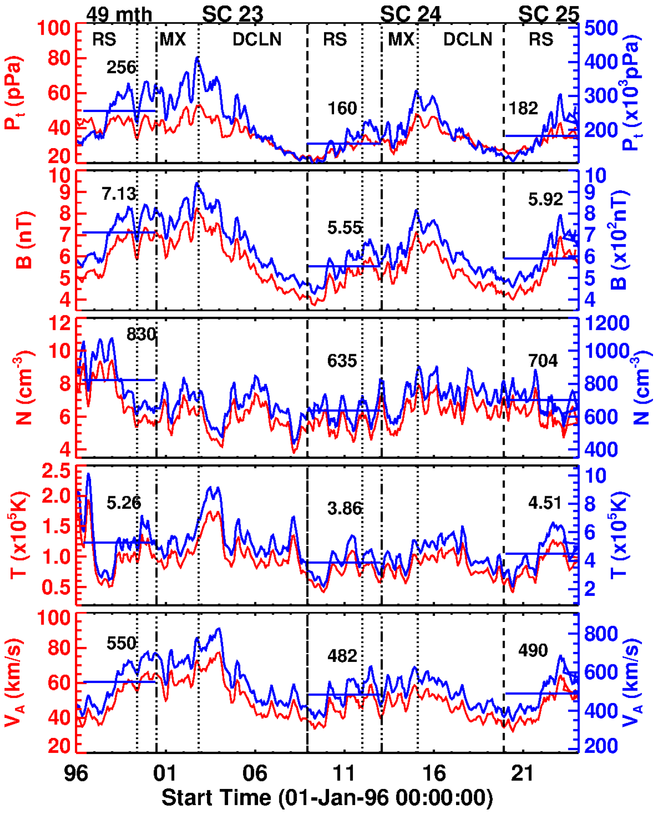

***Figure 6.** Total pressure (Pt), magnetic field magnitude (B), proton density (N), proton temperature (T), and the Alfvén speed (V_A) measured at 1 au are plotted in red. The same parameters extrapolated 20 Rs are shown in blue. The horizontal bars denote the average values over the first 49 months. The rise (RS) maximum (MX) and declining (DCLN) phases of the SCs are marked. All parameters are monthly averages obtained from NASA's OMNI web (http://omniweb.gsfc.nasa.gov).*

Heliospheric State

The weak state of the heliosphere referred to in the previous sections can be confirmed from actual observations of the heliosphere at 1 au using in-situ observations of the solar wind plasma and magnetic field. Figure 6 shows several solar wind parameters obtained from NASA's OMNI web for the period 1996 to end of 2023. Solar cycle variation is evident in all quantities related to solar wind magnetic field (total pressure, magnetic field strength, Alfven speed) because ultimately the magnetic field is related to the solar magnetic fields emerging from beneath the solar surface and filling the heliosphere. All parameters show reduction in SCs 24 and 25 with respect to SC 23. The largest reduction is in the total pressure: 38% in SC 24 and 29% in SC 25. The reduction in SC 25 is smaller in all parameters than in SC 24. This implies that SC 25 is slightly stronger than SC 24, but weaker than SC 23, consistent with the pattern seen in halo CME properties in the three cycles.

Table 3. Percentage of reduction of solar wind parameters in SCs 24 and 25 relative to SC 23

Parameter	**SC 24**	**SC 25**
Total Pressure	38%	29%
Magnetic Field	22%	17%
Density	23%	15%
Temperature	27%	14%
Alfven speed	12%	11%

Summary

Halo CMEs represent an energetic subset of CMEs that have above average speed and width. CMEs expand sufficiently so brightness enhancement appears all around the occulting disk in sky-plane projection. The brightness enhancement is most often caused by the CME-driven shock. We compared the number of halo CMEs observed during the first ~4 years in solar cycles 23-25 with the aim to see if the strength of solar cycle 25 can be assessed relative to the strengths of solar cycles 23 and 24. The strengths of cycles 23 and 24 have been reported as 180 and 113, respectively. The predicted strength of cycle 25 varies from about half to twice the strength of cycle 24. However, predictions based on polar magnetic field proxies indicate a strength of 136, which is intermediate between the strengths of cycles 23 and 24 (Nandy 2021). Our study is consistent with these precursor-based predictions. The main conclusions of this study are:

1. The halo CME abundance is larger cycles 24 and 25 relative to SC 23: The number of halo CMEs normalized to the average sunspot number during the first 49 months of solar cycles 23, 24, and 25 are 1.32, 2.87, and 2.38, respectively.
2. The halo CME source locations are widely distributed on the solar disk in cycles 24 and 25 compared to cycle 23, resulting in relatively large number of limb halos in cycles 24 and 25: only ~7% of SC 23 halos are at CMD >60° compared to 25% in SC 24 and 21.4% in SC 25.
3. Halo formation heights of CMEs in cycles 24 and 25 are similar but smaller than that in cycle 23.
4. The average speed of limb halos is 1428 km/s, 1118 km/s, and 1333 km/s in cycles 23, 24, and 25, respectively indicating once again that cycle 25 values are in between those of cycles 23 and 24.
5. The soft X-ray flare size distributions are about the same in the three cycles. The drop in the number of flares in cycles 24 and 25 is slightly smaller than the reduction in sunspot number.

The flare numbers normalized to the sunspot number are similar indicating that the backreaction of the heliospheric pressure does not affect the flares.

6. Solar wind parameters measured at 1 au confirm the weak state of the heliosphere in all parameters involving solar wind magnetic field strength, the primary one being the total pressure confirming the backreaction of the heliosphere on CMEs leading to higher halo abundance.

Acknowledgments. Work supported by NASA’s LWS program and the STEREO project.

References

Brueckner, G.E., Howard, R.A., Koomen, M.J., Korendyke, C.M., Michels, D.J., Moses, J.D., Socker, D.G., Dere, K.P., Lamy, P.L., Llebaria, A. et al. (1995). The Large Angle Spectroscopic Coronagraph (LASCO). Solar Physics, 162 (1-2), pp. 357–402. https://doi.org/10.1007/bf00733434

Dagnew, F.K., Gopalswamy, N., Tessema, S.B., Akiyama, S., Yashiro, S. and Tesfu, T.Y. (2020a). Intercycle and intracycle variation of halo CME rate obtained from SOHO/LASCO observations. The Astrophysical Journal, 903(2), p.118. https://doi.org/10.3847/1538-4357/abb887

Dagnew, F.K., Gopalswamy, N., Tessema, S.B., (2020b). A comparison of CME expansion speeds between solar cycles 23 and 24. Journal of Physics: Conference Series, 1620(1), pp.012003–012003. http://10.1088/1742-6596/1620/1/012003

Dagnew, F.K., Gopalswamy, N., Tessema, S.B., Akiyama, S. and Yashiro, S. (2022). Effect of the heliospheric state on CME evolution. The Astrophysical Journal, 936(2), p.122. https://doi.org/10.3847/1538-4357/ac8744;

Domingo, V., Fleck, B. and Poland, A.I. (1995). The SOHO mission: An overview. Solar Physics, 162(1-2), pp.1–37. https://doi.org/10.1007/bf00733425

Gopalswamy, N. (2009). Halo coronal mass ejections and geomagnetic storms. Earth, Planets and Space, 61(5), pp.595–597. https://doi.org/10.1186/bf03352930

Gopalswamy, N. (2022). The Sun and Space Weather. Atmosphere, 13(11), p.1781. https://doi.org/10.3390/atmos13111781

Gopalswamy, N., Yashiro, S., Michalek, G., Stenborg, G., Vourlidas, A., Freeland, S. and Howard, R (2009b). The SOHO/LASCO CME Catalog. Earth, Moon, and Planets, 104(1-4), pp.295–313. https://doi.org/10.1007/s11038-008-9282-7

Gopalswamy, N., Yashiro, S., Michalek, G., Xie, H., Mäkelä, P., Vourlidas, A. and Howard, R. (2010). A catalog of halo coronal mass ejections from SOHO. 5(1), pp.7–16. http://newserver.stil.bas.bg/SUNGEO/00SGArhiv/SG_v5_No1_2010-pp-7-16.pdf

Gopalswamy, N., Akiyama, S., Yashiro, S., Xie, H., Mäkelä, P. and Michalek, G. (2014). Anomalous expansion of coronal mass ejections during solar cycle 24 and its space weather implications. Geophysical Research Letters, 41(8), PP.2673-2680, https://doi.org/10.2014- g1059858

Gopalswamy, N., Xie, H., Akiyama, S., Mäkelä, P., Yashiro, S. and Michalek, G. (2015a). The peculiar behavior of halo coronal mass ejections in solar cycle 24. The Astrophysical Journal, 804(1), p.L23. https://doi.org/10.1088/2041-8205/804/1/l23

Gopalswamy, N., Yashiro, S., Xie, H., Akiyama, S. and Mäkelä, P. (2015b). Properties and geoeffectiveness of magnetic clouds during solar cycles 23 and 24. Journal of Geophysical Research: Space Physics,120(11), pp.9221–9245. https://doi.org/10.1002/2015-ja021446

Gopalswamy, N., Akiyama, S., Yashiro, S., Xie, H., Mäkelä, P. and Michalek, G. (2015c). The mild space weather in solar cycle 24. arXiv.org, https://doi.org/10.48550/arXiv- .1508.01603

Gopalswamy, N., Akiyama, S., & Yashiro, S. (2020a). The state of the heliosphere revealed by limb-halo coronal mass ejections in solar cycles 23 and 24. The Astrophysical Journal, 897(1), pp.L1–L1. https://doi.org/10.3847/2041-8213/ab9b7b

Gopalswamy, N., Akiyama, S., Yashiro, S., Michalek, G., Xie, H. and Mäkelä, P. (2020b). Effect of the weakened heliosphere in solar cycle 24 on the properties of coronal mass ejections. Journal of Physics: Conference Series, 1620(1), P012005. https://doi.org/10.1088/1742-6596/1620/1/012005

Gopalswamy, N., Mäkelä, P., Yashiro, S., Akiyama, S. and Xie, H. (2022). Solar activity and space weather. Journal of Physics: Conference Series, 2214(1), p.012021.https://doi.org/10.1088/1742-6596/2214/1/012021

Howard, R.A., Michels, D.J., Sheeley, N.R., Jr. and Koomen, M.J. (1982). The observation of a coronal transient directed at Earth. The Astrophysical Journal, 263, pp. L101–L104. https://doi.org/10.1086/183932

Howard, R.A., Sheeley, N.R., Koomen, M.J. and Michels, D.J. (1985). Coronal mass ejections: 1979–1981. Journal of Geophysical Research, 90(A9), p.8173. https://doi.org/10.1029/ja090ia09p08173

McComas, D.J., Angold, N.G., Elliott, H.A., Livadiotis, G., Schwadron, N.A., Skoug, R.M. and Smith, C.D. (2013). Weakest solar wind of the space age and the current 'mini' solar maximum. The Astrophysical Journal, 779(1), pp.2–2. https://doi.org/10.1088/0004-637x/779/1/2

Michalek, G., Gopalswamy, N. and Yashiro, S. (2019). On the coronal mass ejection detection rate during solar cycles 23 and 24. The Astrophysical Journal, 880(1), p.51. https://doi.org/10.3847/1538-4357/ab26a7

Nandy, D. (2021). Progress in solar cycle predictions: sunspot cycles 24–25 in perspective. Solar Physics, 296(3). https://doi.org/10.1007/s11207-021-01797-2

Petrie, G. (2015). On the enhanced coronal mass ejection detection rate since the solar cycle 23 polar field reversal. The Astrophysical Journal, 812(1), pp.74–74. https://doi.org/10.1088/0004-637x/812/1/74

Yashiro, S., Gopalswamy, N., Michalek, G., St. Cyr, O. C. Plunkett, S. P. Rich, N. B. Howard, R. A. (2004). A catalog of white light coronal mass ejections observed by the SOHO spacecraft. Journal of Geophysical Research, 109(A7). https://doi.org/10.1029/2003ja010282

Yermolaev, Y.I., Lodkina, I.G., Khokhlachev, A.A. and Yermolaev, M.Y. (2022). Peculiarities of the heliospheric state and the solar-wind/magnetosphere coupling in the era of weakened solar activity. Universe, 8(10), p.495. https://doi.org/10.3390/universe8100495

Zhang, J., Temmer, M., Gopalswamy, N., Malandraki, O., Nitta, N.V., Patsourakos, S., Shen, F., Vršnak, B., Wang, Y., Webb, D., Desai, M.I., (2021). Earth-affecting solar transients: a review of progresses in solar cycle 24. Progress in Earth and Planetary Science, 8(1). https://doi.org/10.1186/s40645-021-00426-7

Zhao, X.P. and Webb, D. F. (2003). Source regions and storm effectiveness of frontside full halo coronal mass ejections. Journal of Geophysical Research, 108(A6). https://doi.org/10.1029/2002ja009606

Temporal Variation of 10.7 cm Solar Radio Flux and Selected Cosmic, Geomagnetic, and Interplanetary Indicators during Solar Cycle 24

Özgüç A.[1], Kilcik A[2], Calisir M.[2]

[1]Kandilli Observatory and Earthquake Research Institute, Bogazici University, 34684 Istanbul,Turkey; ozguc@boun.edu.tr
[2]Department of Space Science and Technologies, Akdeniz University Faculty of Science, 07058, Antalya, Turkey; alikilcik@akdeniz.edu.tr; muhammed.calisirr@gmail.com

Abstract

On the basis of a temporal analysis of yearly values of the 10.7 cm solar radio flux (F10.7), the maximum coronal mass ejection (CME) speed index (MCMESI), interplanetary magnetic field strength (scalar B), the solar wind speed, cosmic ray intensity and the geomagnetic Ap, Dst and AE indices, we point out the particularities of solar and geomagnetic activity during the last Solar Cycle (Cycle 24). We also analyze the temporal offset between the F10.7 and the above-mentioned solar, geomagnetic, cosmic and interplanetary indices. It is found that this solar activity index, analyzed jointly with interplanetary parameters, cosmic ray intensity, and geomagnetic activity indices, shows a hysteresis phenomenon. It is observed that these parameters follow different paths for the ascending and descending phases of Cycle 24. The hysteresis phenomenon represents a clue in the search for physical processes responsible for linking the solar activity to near-Earth and geomagnetic responses.

Keywords: 10.7 cm solar radio flux; Solar and geomagnetic activity indices; Solar cycle 24; Hysteresis phenomenon.

Introduction

The dynamic nature of solar activity has profound effects on Earth's environment, making it a critical area of study in solar-terrestrial physics. Solar activity is characterized by various indices, including the 10.7 cm solar radio flux (F10.7), which measures the Sun’s radio emission and correlates with the level of solar activity (Barbieri & Mahmot, 2004). Another significant indicator is the maximum coronal mass ejection (CME) speed index (MCMESI), which highlights the power of CMEs, explosive events that eject solar material into space. These solar phenomena influence the interplanetary magnetic field (IMF), solar wind speed, cosmic ray intensity, and geomagnetic indices such as Ap, Dst, and AE.

Solar Cycle 24 (December 2008 - December 2019) exhibited unique characteristics, particularly its notably low solar activity. This cycle presents an invaluable opportunity to explore the interrelationships among various solar, geomagnetic, cosmic, and interplanetary parameters. The cyclic nature of solar activity influences the frequency and intensity of solar flares, CMEs, and other solar events that directly impact Earth's geomagnetic field (Hathaway et al., 2002; Özgüç et al., 2022).

The study of these interactions has shown that geomagnetic activity, measured through indices like Ap, Dst, and AE, is closely related to solar activity (Verbanac et al., 2011; Sarp & Kilcik, 2018). These geomagnetic indices help quantify the effects of solar phenomena on Earth's magnetic environment, illustrating how solar activity drives geomagnetic responses (Obridko & Shelting, 2009; Kirov et al., 2013).

A phenomenon of particular interest is hysteresis, where solar and geomagnetic parameters exhibit different behaviors during the different phases of a solar cycle. This behavior provides insights into the physical processes that link solar activity to geomagnetic effects (Demetrescu

& Dobrica, 2008). Understanding these relationships is crucial for improving our ability to predict space weather events and mitigate their impacts on technological systems and human activities on Earth.

In this study, we analyze the temporal variations, cross-correlations, and hysteresis patterns of the 10.7 cm solar radio flux, MCMESI, scalar B, solar wind speed, cosmic ray intensity, and geomagnetic indices during Solar Cycle 24. By examining these parameters, we aim to elucidate the complex interactions between solar and geomagnetic activity and contribute to the broader understanding of solar-terrestrial relationships. Data and methods are detailed in Section 2, results are presented in Section 3, and conclusions is provided in Section 4.

Data

This study uses datasets covering Solar Cycle 24 (December 2008 - December 2019) to analyze solar and geomagnetic activities. The data and their sources are detailed below:

i) 10.7 cm Solar Radio Flux (F10.7): The solar radio flux at 10.7 cm (2800 MHz) is an excellent indicator of solar activity. Often called the F10.7 index, it is one of the longest running records of solar activity. The F10.7 radio emissions originates high in the chromosphere and low in the corona of the solar atmosphere. It correlates well with the sunspot number as well as a number of UltraViolet (UV) and visible solar irradiance records. The F10.7 has been measured consistently in Canada since 1947, first at Ottawa, Ontario; and then at the Penticton Radio Observatory in British Columbia, Canada. Unlike many solar indices, the F10.7 radio flux can easily be measured reliably on a day-to-day basis from the Earth’s surface, in all conditions of weather. Therefore, it is a very robust data set with few gaps due to the calibration issues.

ii) Maximum Coronal Mass Ejection Speed Index (MCMESI): It introduced by Kilcik A, et al., (2011) as a new solar and geomagnetic activity index as a measure of the linear speed of the fastest CME observed in a day. The MCMESI displays better correlation with geomagnetic indices than the ISSN, which suggests that the MCMESI may be a powerful indicator of both solar and geomagnetic activity (Kilcik et al., 2011).

iii) Interplanetary Magnetic Field (IMF)/Scalar B: It includes solar magnetic fields that were carried into interplanetary space by the solar wind. The source of the fast solar wind is thought to be coronal holes, which are open magnetic-field regions on the Sun, while slow solar wind originates at closed magnetic regions thought to be associated with active regions. The structure and dynamics of the IMF (scalar B) are key for understanding space weather.

iv) Solar Wind Speed: The solar wind continuously flows outward from the Sun and consists mainly of protons and electrons in a state known as a plasma. Solar magnetic field is embedded in the plasma and flows outward with the solar wind. Different regions on the Sun produce solar wind of different speeds and densities. Coronal holes produce solar wind of high speed, ranging from 500 to 800 Km/s. The north and south poles of the Sun have large, persistent coronal holes, so high latitudes are filled with fast solar wind. In the equatorial plane, where the Earth and the other planets orbit, the most common state of the solar wind is the slow speed wind, with speeds of about 400 Km/s. High speed winds bring geomagnetic storms while slow speed winds bring calm space weather condition.

v) Cosmic-Ray Intensities (CRI): Cosmic rays are high energy particles that flow into our solar system from outer space. The intensity at which cosmic rays collide with the Earth’s atmosphere varies. It varies also with latitude, because the flux is modulated by the Earth’s magnetic field and cosmic rays are guided by the Earth’s magnetic field lines. The cosmic ray intensity also varies with altitude. The corrected cosmic ray intensity data used in this study are taken from Oulu/Finland nötron monitor station (https://cosmicrays.oulu.fi/#solar)

vi) Geomagnetic Ap Index: The K index is used to measure changes in the horizontal component of the magnetic field. However, since the K index is not directly related to geomagnetic activity the Kp index was introduced and it is derived from the mean standardized K index of 13 geomagnetic observatories located between ± 44 and ± 60 degrees of the geomagnetic latitude. This planetary index is designed to measure the magnetic effect of solar particle radiation. The 3-hourly ap index is derived from the Kp index and the Ap index used in this study is an average of the ap index over 24 hours (Bartels, Heck, and Johnston, 1939).

vii) Geomagnetic AE (Auroral Electrojet) Index: AE index is designed to provide a global, quantitative measure of auroral zone magnetic activity produced by enhanced Ionospheric currents flowing below and within the auroral oval. Ideally, It is the total range of deviation at an instant of time from quiet day values of the horizontal magnetic field (h) around the auroral oval. Defined and developed by Davis and Sugiura [1966], AE has been usefully employed both qualitatively as a correlative index in studies of substorm morphology, the behavior of communication satellites, radio propagation, radio scintillation, and the coupling between the interplanetary magnetic field and the earth's magnetosphere. AE data is maintained at WDC (World Data Center) Kyoto and NGDC (National Geophysical Data Center).

viii) Geomagnetic Disturbance Storm Time Index (Dst): It was proposed by Sugiura (1964) to measure the magnitude of magnetospheric currents that produce an axially symmetric disturbance field. This index is a measure of the variation of the field due to the ring current arising in the magnetosphere during a geomagnetic storm. Data from four observatories are used to derive the Dst index. Because of the need for good data, these observatories were chosen sufficiently far from the auroral and equatorial electrojet regions. Irregularities observed in the Dst index that have a negative sign and fluctuate within the $-50\ \text{nT} \leq \text{Dst} < -30\ \text{nT}$ range are called small storms, while those within the $-100\ \text{nT} \leq \text{Dst} < -50\ \text{nT}$ range are called moderate storms, $-200\ \text{nT} \leq \text{Dst} < -100\ \text{nT}$ fluctuations are called intense storms, and a Dst index below -250 nT defines big geomagnetic storms (Gonzalez, Tsurutani, and Clúa de Gonzalez, 1999).

Method and Results

Temporal Variation Analysis

As a first step, we plot the temporal variation of used data sets (Figure 1 and Table 1). To remove the short-term fluctuations all monthly mean data sets were smoothed with 11 step running average smoothing method.

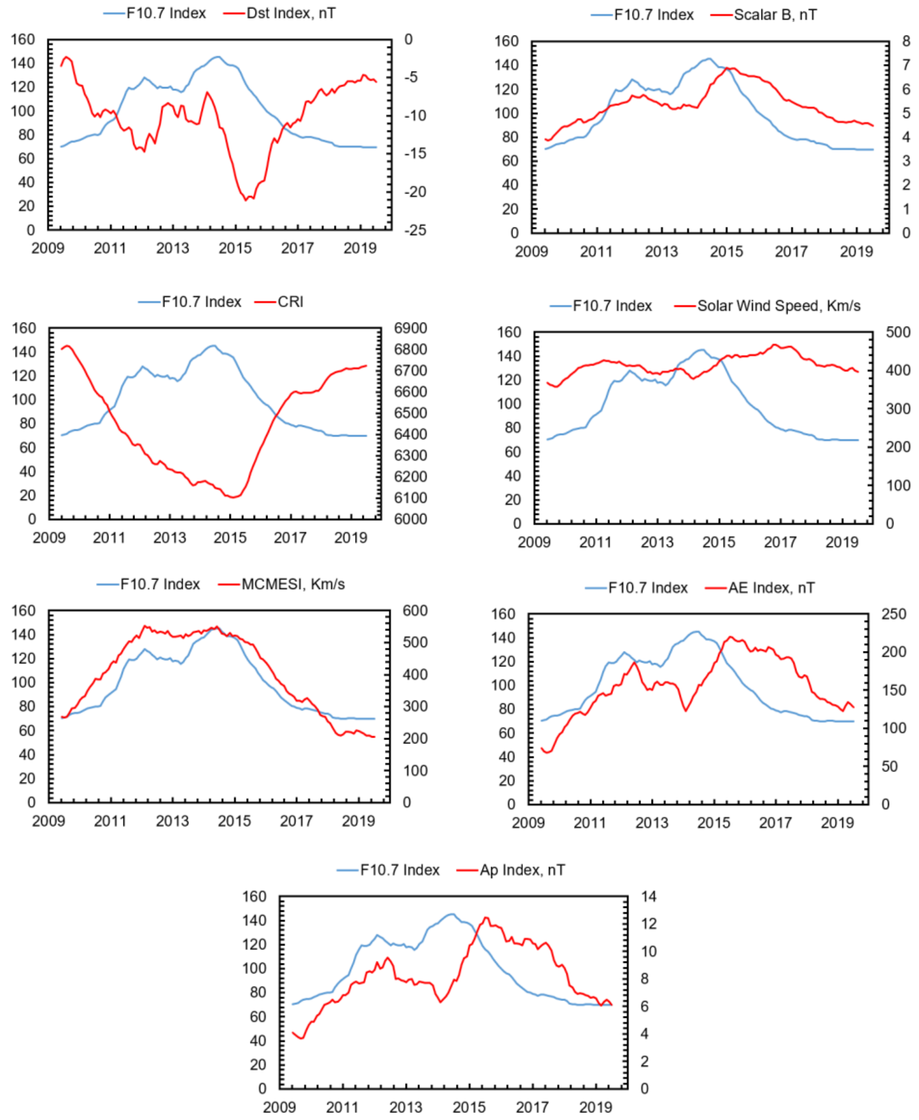

Figure 1. *Temporal variation analysis of the relationship between F10.7 and other indices.*

Table 1. *Results of temporal variation analysis*

Data	**Maximum Values**		**Delay between peaks (month)**
F10.7-Scalar B	145.35	6.9	6
F10.7-Dst	145.35	-21.12	10
F10.7-Ap	145.35	12.48	12
F10.7-CRI	145.35	6103.29	7
F10.7-Solar Wind Speed	145.35	467.42	28
F10.7-AE	145.35	220.33	12
F10.7-MCMESI	145.35	552.57	– 27

Cross Correlation Analysis

As a second step, we performed cross correlation analysis between F10.7 and other indices used (Figure 2 and Table 2). The method gives the maximum correlation between two data sets together with possible time delay. If the delay is negative that means the first parameter leads the second one and vice versa. The error level of obtained correlation coefficients were calculated by using Fisher's test that gives the upper and lower boundary of the correlation coefficient with 95 % confidence level.

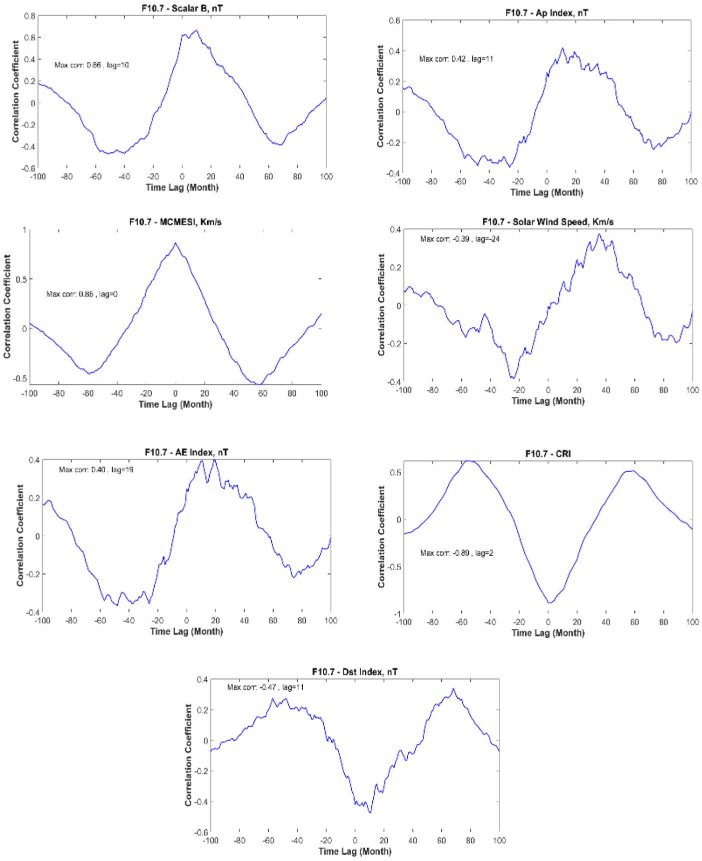

Figure 2. *Cross-correlation analysis results between F10.7 and other indices.*

Table 2. *Results of cross correlation analysis*

Data	**Correlation Coefficient**	**Time Lag**
F10.7-Scalar B	0.66 ± 0.07	10
F10.7-MCMESI	0.86 ± 0.04	0
F10.7-Dst	-0.47 ± 0.08	11
F10.7-AE	0.40 ± 0.08	19
F10.7-Solar Wind Speed	-0.39 ± 0.08	-24
F10.7-Ap	0.42 ± 0.08	11
F10.7-CRI	-0.89 ± 0.04	2

Hysteresis Analysis

As a last step of our analysis, we plotted the hysteresis behavior between the solar radio flux (F10.7) and the maximum (CME) speed index (MCMESI), Cosmic ray intensity (CRI), solar wind speed, Disturbance Storm Time (Dst) index, interplanetary magnetic field (IMF)/Scalar B, and geomagnetic Ap / AE index during solar cycle 24 (Figure 3). We choose the F10.7 solar activity index to be the abscissa of the plots with the equal scale in below figures to display the effects of hysteresis clearly. In general, all data sets show hysteresis behavior only around the maximum phase of the Cycle 24. Dst and CRI data sets show counter clockwise circulation, while the Scalar B, the MCMESI, Ap Index, Solar wind speed and AE index show clockwise circulation which is not a normal characteristic of hysteresis in magnetic materials.

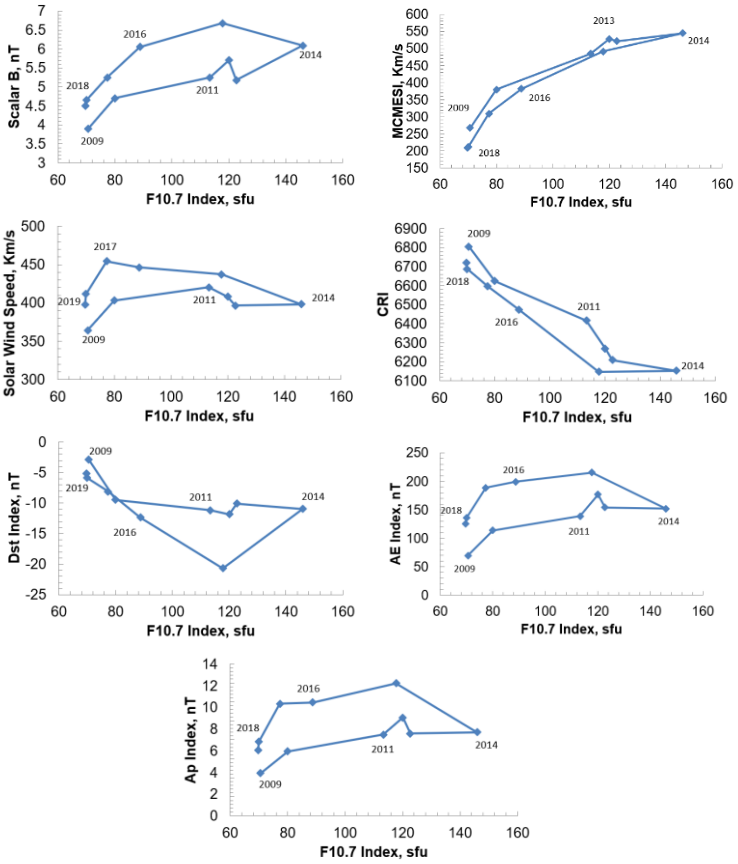

Figure 3. *The hysteresis behavior between the solar radio flux (F10.7) and the MCMESI, CRI, solar wind speed, Dst index, IMF/Scalar B, and Ap, AE index during solar cycle 24.*

Conclusion

We examined the relationship between solar, cosmic and geomagnetic activities during the last Solar Cycle (Cycle 24) on the basis of a temporal analysis, correlation coefficient calculations and hysteresis phenomena. Our main findings are as follows;

- In general, all data sets show hysteresis behavior only around the maximum phase of the Cycle 24. Dst and CRI data sets show counter clockwise circulation, while the Scalar B, the MCMESI, Ap Index, Solar wind speed and AE index show clockwise circulation which is not a normal characteristic of hysteresis in magnetic materials.

- It is observed that these parameters follow different paths for the ascending and descending phases of Cycle 24.

- The hysteresis phenomenon represents a clue in the search for physical processes responsible for linking the solar activity to near-Earth and geomagnetic responses.

- We analyzed the temporal offset between the F10.7 and the above-mentioned solar, geomagnetic, cosmic and interplanetary indices. We found that the peak of all parameters except the MCMESI show time delay with F10.7 and all data sets used here show meaningful correlation with F10.7.

References

Barbieri, L.P. and Mahmot, R.E. 2004, October–November 2003's space weather and operations lessons learned, Space Weather 2, S09002

Bartels, J., N. H. Heck, and H. F. Johnston (1939), The three-hour-range index measuring geomagnetic activity, Terr. Magn. Atmos. Electr., 44(4), 411–454, doi:10.1029/TE044i004p00411.

Davis, T. N., and M. Sugiura (1966), Auroral electrojet activity index AE and its universal time variations, J. Geophys. Res., 71(3), 785–801, doi:10.1029/JZ071i003p00785.

Demetrescu, C., Dobrica, V. (2008), Signature of Hale and Gleissberg solar cycles in the geomagnetic activity. JGRA, Vol 113, Issue A2, CiteID A02103, DOI:10.1029/2007JA012570

Gonzalez, W.D., Tsurutani, B.T. & Clúa de Gonzalez, A.L. Interplanetary origin of geomagnetic storms. Space Science Reviews 88, 529–562 (1999). https://doi.org/10.1023/A:1005160129098

Hathaway, D. H., Wilson, R. M., Reichmann, E. J.(2002). Group Sunspot Numbers: Sunspot Cycle Characteristics, Sol. Phys. 211, 357 – 370.

Kilcik, A., Yurchyshyn, V. B., Abramenko, V., Goode, P. R., Gopalswamy, N., Ozguc, A., & Rozelot, J. P. (2011a). Maximum coronal mass ejection speed as an indicator of solar and geomagnetic activities. The Astrophysical Journal, 727(1), 44.

Kilcik, A., Yurchyshyn, V. B., Abramenko, V., Goode, P., Ozguc, A., Rozelot, J. P., & Cao, W. (2011b). Time distribution of large and small sunspot groups over four solar cycles, The Astrophysical Journal, 730, 30–37.

Kirov, B., Obridko, V. N., Georgieva, K., Nepomnyashtaya, E. V., Shelting, B. D. (2013). Long-term variations of geomagnetic activity and their solar sources, Geomagnetism and Aeronomy, Vol 53, Issue 7, pp.813-817, DOI:10.1134/S0016793213070128

Obridko, V. N., Shelting, B. D. (2009). Anomalies in the evolution of global and large-scale solar magnetic fields as the precursors of several upcoming low solar cycles, Astronomy Letters, Vol 35, Issue 4, pp.247-252, DOI:10.1134/S1063773709040045.

Ozguc, A., Kilcik, A., Yurchyshyn, V. (2022). Temporal and Periodic Variations of the Solar Flare Index During the Last Four Solar Cycles and Their Association with Selected Geomagnetic-Activity Parameters, SolPhys, Vol 297, Issue 9, article id.112, DOI:10.1007/s11207-022-02049-7.

Sarp, V., Kilcik, A. (2018). Solar flare and geomagnetic activity relations, Turkish Journal of Physics, Vol 42, Issue 3, pp. 283-292, DOI:10.3906/fiz-1712-18.

Sugiura, M. (1964) Annals of the International Geophysical Year, Vol. 35. Pergamon Press, Oxford. 945.

Verbanac, G., Mandea, M., Vrsnak, B., Sentic, S. (2011), Evolution of solar and geomagnetic activity indices, and their relationship: 1960 – 2001. SolPhys. Issue 1-2, pp. 183-195, DOI:10.1007/s11207-011-9801-y.

A Needle in a Haystack: The Leptocline.

Rozelot J.P.[1], *Kilcik, A.*[2]

[1] Université de la Côte d’Azur (Emeritus), Grasse, 06130, France; jp.rozelot@orange.fr
[2] Department of Space Science and Technologies, Akdeniz University Faculty of Science,
07058, Antalya, Turkey.

Abstract.

Studies of solar (and stellar) dynamos face a problem of utter complexity, i.e., the interaction of a turbulent plasma in the convection zone, associated with latitudinal rotation together with magnetic field acting in a highly stratified medium, covering wide ranges of spatial and temporal scales. Recent theoretical models for the solar dynamo in complex 3-D simulations highlighted changes of the Sun’s stratification, mainly in the upper zones, pointing the role of the leptocline, a shallow and sharp shear layer in the top ~8-10 Mm. Here, we give here a brief history of the circumstances that led to the discovery of this layer, characterized by a strong radial rotational gradient at mid latitudes and self-organized meridional flows. We give an overview of the physical solar parameters that originate in this layer: opacity, superadiabicity and turbulent pressure changes; the hydrogen and helium ionization processes; sharp decrease in the sound speed; probably an oscillation phase of the seismic radius associated with a non-monotonic expansion with depth; probably temporal changes in photospheric zonal and sectorial modes and their associated gravitational moments. Likely also the initial place of the solar wind escape. In addition, the leptocline may play a key role in the formation of the magnetic butterfly diagram. Such results should be the starting point of systematic further investigations of structure and dynamics in this layer, leading to a better understanding of the solar cycle.

Keywords: Solar structure; Solar rotation; Solar convection.

Introduction.

Recent studies focused on the physical conditions prevailing in the Sun's subsurface layers aimed to understand how the solar rotation varies in latitude, in depth and with time. Indeed, the radiative interior of the Sun and its convective zone, are separated, at a depth of around 0.7 $R_\odot$, by a thin layer ($\approx$ 0.05 $R_\odot$), called the tachocline (Spiegel & Zahn, 1992), which is known to be the seat of the differential rotation. From this depth, once the latitude variations are underway, one might expect a uniform variation up to the surface. But this is not the case, as helioseismology show. Significant changes occurred in a near-surface shear layer (NSSL), occupying around the 5% of the solar interior, and, within this zone, around 2% (i.e. approximatively 10 Mm), it is not impossible that a nonlinear alpha-omega dynamo could be operating. Thus, the velocity shear may convert a part of the poloidal magnetic field into the toroidal field (in addition to the global dynamo operating in the tachocline region), strongly implicating the magneto-rotational instability (Vasil et al., 2024). It is thus suggested that the solar dynamo starts from this very thin sub-surface shallow layer, that we named by analogy to the tachocline, “leptocline” (Godier & Rozelot, 2001), from Greek “leptos’, thin and “klino”, tilt, or slope.

The aim of this paper is to briefly highlight the role of the leptocline.

A serendipitous discovery, albeit unnoticed.

Interpreting the solar limb shape distortions, Armstrong & Kuhn (1999) computed the density d_n and pressure s_n surfaces using a standard solar rotation profile, *n* being the order in a Legendre polynomial expansion of the contour of a shell of radius *r* (note that r < R⊙ is the radius of a thin shell enclosing a mass *dM*-or density $d\rho$). Figure 1 shows the results in the case of *n*=4 (hexadecapolar term). The tachocline, at *r* = 0.7 R⊙ is well marked, and a zoom for abscissa *r* between 0.960 R⊙ and 1 R⊙ shows a non-constant zone marked by a rise followed by a dip. This feature, overlooked at the time is the signature of the NSSL (near surface shear layer), obtained with a non helioseismic method.

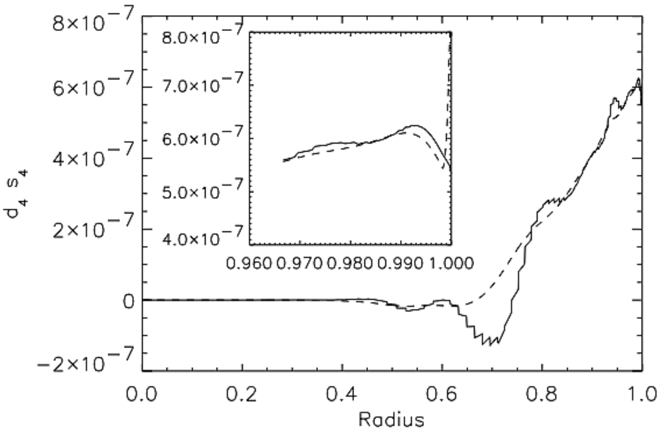

Figure 1. *The density (d) and pressure (s) surfaces variations with depth (radius), represented by the solid and dashed lines, respectively. After Armstrong & Kuhn (1999). The tachocline is well marked, and so is the leptocline (zoom in the upper figure), a feature that went unnoticed at the time.*

Solar rotation: a complex mechanism.

Solar rotation has been widely debated in recent years, through many books and articles, and can be summarized as follows (Figure 2):

- Below 0.68 R⊙, the radiative interior rotates almost rigidly, at about 430 nHz. The core itself may rotate faster.
- The transition from uniformly rotating radiation zone to differentially-rotating convection zone occurs in a thin layer from 0.68 R⊙ to 0.73 R⊙, called the **tachocline.**
- In the bulk of the convection zone (0.73 R⊙ < r < 0.96 R⊙), the rotation rate varies strongly with latitude. The equator rotates about 30% faster than the poles; from ~ 460 nHz at 0° latitude to ~ 340 nHz at 80° latitude.
- In a shallow layer > 0.96 R⊙ up to 1 R⊙, the rotation rate decreases by about 5% at all latitudes, showing however a more complex behavior near the surface. This layer is called the **Near Subsurface Shear Layer (NSSL).**
- A substructure of NSSL, so-called **leptocline**, located from the surface, covers about 10 Mm in depth within the convection zone (0.985 R⊙ < r < 1.0 R⊙).

- The contours of constant angular velocity are inclined by about 25° with respect to the rotational axis over a wide range of latitudes, i.e. rotation does not follow the Taylor-Proudman theorem[1].
- Within the leptocline unfolds an intricate behavior of the variation of the radial gradient $\partial \log \Omega / \partial \log r$, in latitude, depth and in time.

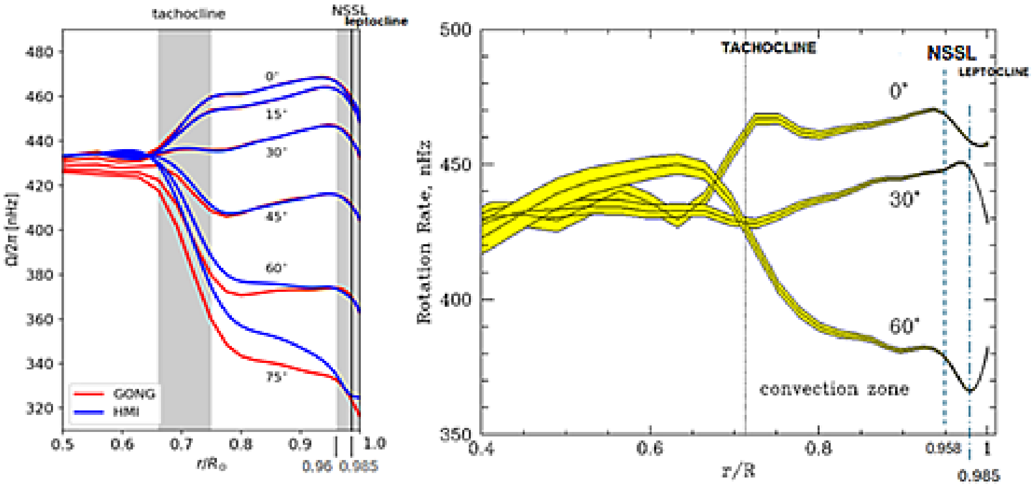

Figure 2. *Left. Internal profile of the solar rotation showing in grey shades (a) the tachocline (0.68 $R_\odot$ to 0.73 $R_\odot$); (b) the Near Surface Shear Layer (NSSL) beyond 0.96 $R_\odot$ (see Hotta et al., 2023) within which lies the leptocline (0.985 $R_\odot$ to 1.0 $R_\odot$). Results obtained by the Global Oscillation Network Group (GONG) (data courtesy of R. Howe, using the method of Howe et al. 2005) and the Helioseismic and Magnetic Imager (HMI) onboard the Solar Dynamics Observatory (SDO) (Larson and Schou, 2018). Note the sharp decrease of the velocity rate. Right. Solar profile after Kosovichev et al. (1997). The complex profile is clearly visible within the NSSL, sharply pronounced in the leptocline, where the rotation gradient displays large and significant variations in latitude, depth and time (cf. para 6).*

Solar radius with respect to the leptocline.

An accurate measure of the solar diameter[2] is still very difficult. The first reason is to agree on the definition of a diameter for a rotating fluid; the second is to highlight the physical reasons that have emerged between theoretical models and ground-based or space observations. A review of photospheric radius measurements R_{ph} has been made in Rozelot & Damiani (2012, upgraded in Rozelot et al. 2016), to which eclipse measurements can be supplemented (Lamy et al. 2015). Based on the work of Takada & Gough (2024), and to make things here easier, we

---

[1] Under certain conditions, when a solid body is moved slowly within a fluid that is steadily rotated with a high angular velocity Ω, the fluid velocity will be uniform along any line parallel to the axis of rotation. Ω must be large compared to the movement of the solid body in order to make the Coriolis force large compared to the acceleration terms.

[2] Radius and diameter are used interchangeably, with a few exceptions. For instance, in the case of observations by solar astrolabes, where the diameter is not twice the radius, a very small angle being introduced by construction between the measurement of the two opposite radii.

propose the following glossary as given in Table 1 (see also Kosovichev et al., 2025, for further details).

Table 1. *Proposed new glossary of the various solar radius in use (in brief). Modified from Takada & Gough (2024).*

Radius name	Label	Meaning
Photospheric	R_{ph}	Distance from the solar center to the photospheric surface, defined as the layer where the optical depth $\tau = 1$ for a particular wavelength, usually 500 nm.
Canonical	R_c	Adopted radius through a consensus, generally, at IAU GA. The radius used to calibrate models is labelled $R_\odot$
Seismic:	R_s	Radius calculated using helioseismology. In general, the radius is defined as the radial distance at which the temperature equals the effective temperature.
1. Fundamental	R_f	Fundamental photospheric radius scaled through f-modes, which is the distance from the solar center to the center of energy of each f-mode (essentially the peak in the kinetic-energy distribution).
2. Acoustic	R_{ac}	Acoustic photospheric radius scaled through p-modes, which is the distance from the center to the subphotospheric layer where the acoustic cut-off frequency changes extremely rapidly.

The two space missions SOHO (Solar and Heliospheric Observatory) (Scherrer et al., 1995) and SDO (Solar Dynamics Observatory) (Scherrer et al., 2012) has provided long time-series of solar oscillations that has been intensively analyzed. It has been shown that the radius of the Sun can be determined, that can be called the "seismic radius" of the Sun, to differentiated it from the conventional photospheric radius. Schou (1997) & Antia (1998) were the first in analyzing the data to find a "fundamental photospheric" radius calibrated through f-modes R_f, lower than the observed one through optical instruments (photospheric radius R_{ph}): by 310 km for the first author and 203 km for the second. This discrepancy seems to have been explained by Haberreiter et al. (2008) by a difference of 0.333 ± 0.008 Mm between the height at disk center where the optical depth at $\tau_{500} = 1$, and the inflection point of the intensity profile on the limb. However, Takada & Gough (2024) point out that the three models used by Haberreiter et al., (2008) close to those of Brown & Christensen-Dalsgaard (1998), "*do not lead to the same results, rendering this explanation premature*". Further effort to study this issue is required to clarifying the properties of the NSSL.

Kosovichev & Rozelot (2018), analyzed 21 years of helioseismology data (the Michelson Doppler Imager (MDI) on board SOHO - Scherrer et al. 1995) and the Helioseismic and Magnetic Imager (HMI on board SDO - Scherrer et al. 2012) to resolve previous uncertainties and compare variations of the seismic radius over two solar cycles. After removing the f-mode frequency changes associated with the surface activity, they find that the mean seismic radius is reduced by 1–2 km during the solar maxima and that most significant variations of the solar radius occur beneath the visible surface of the Sun at a depth of about 5 ± 2 Mm, where the radius is reduced by 5–8 km (Figure 3). Other authors have reached similar conclusions, see for instance Hernandez et al. 2009; Antia (2003) who reported "From our results, we can put a conservative upper limit of 2 km on radius variations during the last 6 yr, from 1996 May 1 to 2002 August 21", (but with a gap in data sets between 1998.5 and 1999.2).

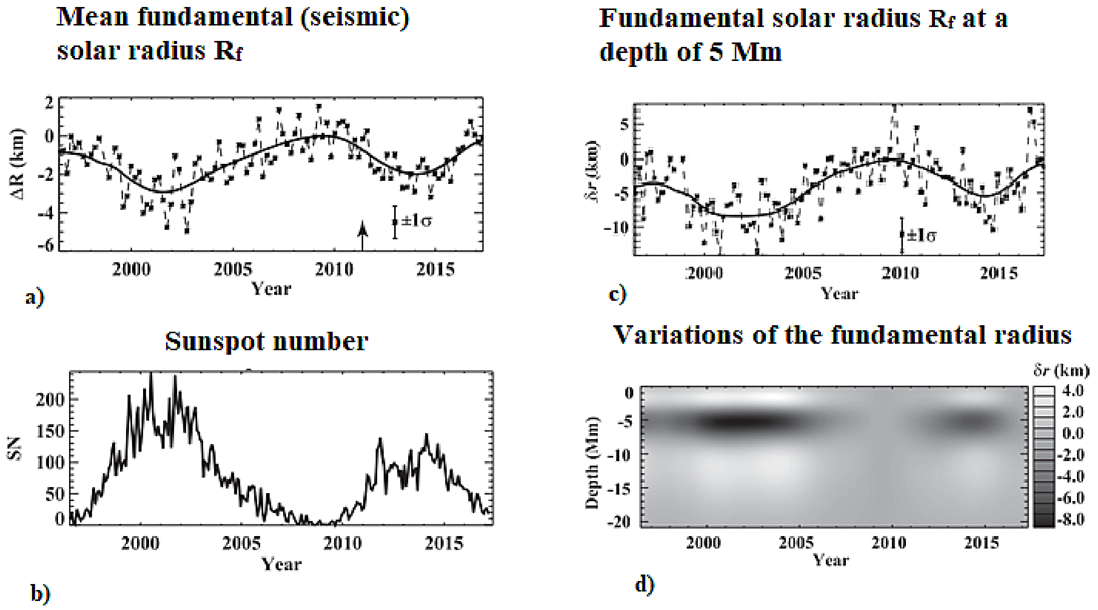

Mean fundamental (seismic) solar radius R_f

Fundamental solar radius R_f at a depth of 5 Mm

Sunspot number

Variations of the fundamental radius

Figure 3. *Solar cycle variations of (a) the mean fundamental seismic radius R_f (average over all values of degree ℓ, from ℓ = 137 to ℓ = 300); the arrow indicates the start of the HMI data set (after MDI data set); (b) the sunspot number averaged for the same time intervals as the helioseismology data: antiphase correlation is clearly visible; (c) changes of the fundamental seismic radius R_f at the depth of 5 Mm; (d) variations with time and depth beneath the solar surface. The dark color (negative values) corresponds to contraction and the light color (positive values) corresponds to expansion of subsurface layers (After Kosovichev & Rozelot, 2018).*

Such variations may seem insignificant and questionable in view of several factors: data errors (a change in systematic errors may lead to spurious variations of the same order), magnetic field variations below the outermost surface layers, density perturbations, turbulence, supergranulation… However, HMI has proved to be an extremely high precision instrument, able to measure the oscillations of the solar limb with a positional accuracy of the order of microseconds and a relative brightness accuracy of 10^{-6}. Figure 3 (a, b), show an antiphase correlation of the fundamental surface photospheric radius scaled through f-modes. It can be noticed that radius variations give a real insight into changes of the Sun's subsurface stratification, particularly around an average depth of 5 Mm (between 2 and 8 Mm, i.e. inside the leptocline). Kholikov & Hill (2008) using very low-p-modes found also a clear antiphase variation of the acoustic photospheric radius R_{ac} with solar activity.

Such results have been obtained assuming a homogeneous stratification. What happens if it is not the case? Assuming variations of $\delta r/r$, Lefebvre and Kosovichev (2005) and Lefebvre et al. (2007a, 2007b) found a change in the structure of the subsurface layers down to about 97 % of the photospheric radius. Even if (i) the contribution of the near-surface effects have been neglected, and (ii) the near-surface effects of turbulence and magnetic fields were not treated, Figure 4 (left) shows (i) no significant changes in the variation of the subsurface layers' depth below 0.97 $R_\odot$, and (ii) nonmonotonic changes in the stratification, with the inner layer (below 0.99 $R_\odot$); moving up during the increase of activity (compression) while the outer layer (above 0.99 $R_\odot$,) moves down (relaxation), giving substance to the leptocline. The precise localization could be ascertained by about less than 0.003 $R_\odot$.

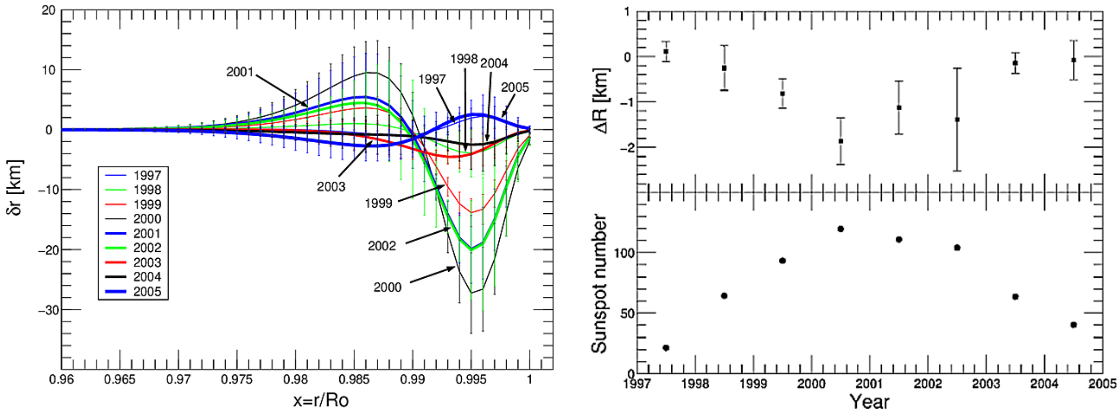

Figure 4. *Left: Radial variation δr (in km) of the solar stratification, as a function of the fractional radius $x = r/R_\odot$, obtained as a solution of the inversion of f-mode frequencies by a least-squares regularization technique (Lefebvre & Kosovichev, 2005). The reference year is 1996. The error bars are the standard deviation after averaging over a set of random noise added to the relative frequencies. The leptocline is well localized between 0.985 and 0.996, with a typical half-width of ~ 0.003 $R_\odot$. Right: temporal variation of ΔR near the solar surface at $r = R_\odot$, plotted together with the variation of the sunspot number for the same period. The variation of the seismic radius at the surface is found to be in antiphase with the solar cycle, with an amplitude of about 2 km. It is important to keep in mind that without information at high degree ℓ we cannot constrain the surface radius better and that, in reality, this variation at the surface could be larger provided if it is more localized.*

Figure 4 (right) shows temporal variation of the radius near the solar surface (R_{ph}), together with the variation of the sunspot number for the same period. The variation of the seismic radius at the surface is in antiphase with the solar cycle, with an amplitude of about 2 km. All these results are nevertheless subject to the fact that the lack of very high f-mode degrees prevents to understand the very outer layers (above ~3 Mm). One might think that it would be enough to expand the degree ℓ to infinity to converge R_f to R_{ph}, but then, the surface is undefined (a fantom, as Takada & Gough, 2024 showed).

5. Rotational gradient with respect to the leptocline.

Komm (2022) made an exhaustive study of the radial gradient of the solar rotation rate in the near-surface shear layer (NSSL), from about 0.950 $R_\odot$ to the solar surface, using the ring-diagram analysis applied to Global Oscillation Network Group (GONG) and Helioseismic and Magnetic Imager (HMI) Dopplergrams. He thus explored the variation of the radial gradient, over latitudes, density, depth and time (Solar Cycles 23 and 24). The results, which are very extensive, can be summed up as follows (see also Figures 5 and 6):

- The average radial gradient is $\partial \log \Omega / \partial \log r = -1.0 \pm 0.1$ at a depth of $0.990\ R_{\odot}$ (in agreement with previous studies);
- The average radial gradient is rather flat within ± 40° latitude from about $0.970\ R_{\odot}$ to the solar surface;
- The average radial gradient is $\partial \log \Omega / \partial \log r = -0.11 \pm 0.01$ at $0.950\ R_{\odot}$, (base of the NSSL), increasing in amplitude to $-0.42 \pm .02$ at $0.97 R_{\odot}$ and then to -1.04 ± 0.06 at $0.990 R_{\odot}$;
- Between $0.990 R_{\odot}$ and $0.998 R_{\odot}$, the average radial gradient is steeper than -1 within the observed latitude range:
  - (i) the steeper slope $\partial \log \Omega / \partial \log r = -2.6 \pm 0.2$ is obtained at $0.998\ R_{\odot}$ (or 1.5 Mm in depth), derived from HMI data; a radial gradient steeper than −2 close to the surface agrees with recent global results using a new technique that allows to fit high degree modes (as previously seen, Reiter et al., 2020);
  - (ii) such high radial gradient indicates that the NSSL consists of two separate regimes. The first one, near the surface, coincides with a shallow shear layer within 10 Mm from the surface (leptocline), as found in a numerical model of the NSSL with radial gradients far steeper than −1 (Kitiashvili et al., 2022);

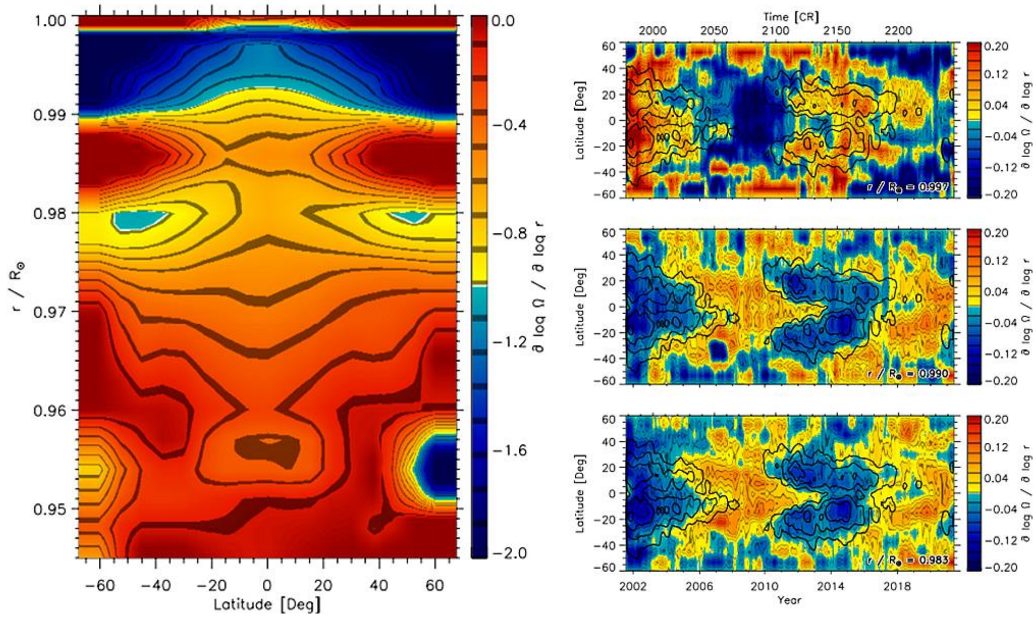

Figure 5. *Left: The radial gradient of the solar rotation rate as a function of latitude and radius using 30°-tile Ring Diagram Analysis (RDA) results derived from HMI data averaged over Solar Cycle 24. The values have been interpolated on an equidistant grid in radius and onto the 7.5° grid in latitude used by 15°-tile RDA.*

Right: The temporal variation of the residual gradient of the solar rotation rate after subtracting the average offset and subtracting the temporal mean at every latitude at three depths (top: $0.997R_{\odot}$, middle: $0.990R_{\odot}$, bottom: $0.983R_{\odot}$). The time coordinate is given in years (bottom x-axis) and

Carrington Rotations (CRs, top x-axis). Black contours indicate magnetic activity (5, 10, 20, 40 G) smoothed over five CRs. A variation with the solar cycle is noticeable at all three depths. The residual gradient is larger (in amplitude) than average at locations of high magnetic activity at $0.990R_\odot$ *and* $0.983R_\odot$ *and smaller than average at quiet locations. However, it is the opposite behavior at* $0.997R_\odot$ *with the residual gradient being smaller (in amplitude), than average at locations of high magnetic flux. (See Komm, 2022).*

(iii) a value of −1.5 occurs on average at $0.996R_\odot$ (or about 3 Mm in depth), which coincides with the maximum of the flow divergence of quiet regions, which represents supergranular flows; the divergence decreases to half its maximum amplitude by a depth of about 8 Mm, which might imply that the upper layer of the NSSL is heavily influenced by supergranule;

- The radial gradient of the solar rotation rate varies with the solar cycle:
  At locations of high magnetic activity, the radial gradient is more negative than average, from about $0.970\ R_\odot$ to $0.990\ R_\odot$, while in quiet regions the radial gradient is less negative than average at these depths. Close to the surface, at $0.997\ R_\odot$, this relationship appears to be reversed.
- The variation of the radial gradient more likely indicates the presence or absence of magnetic flux (above a certain threshold).

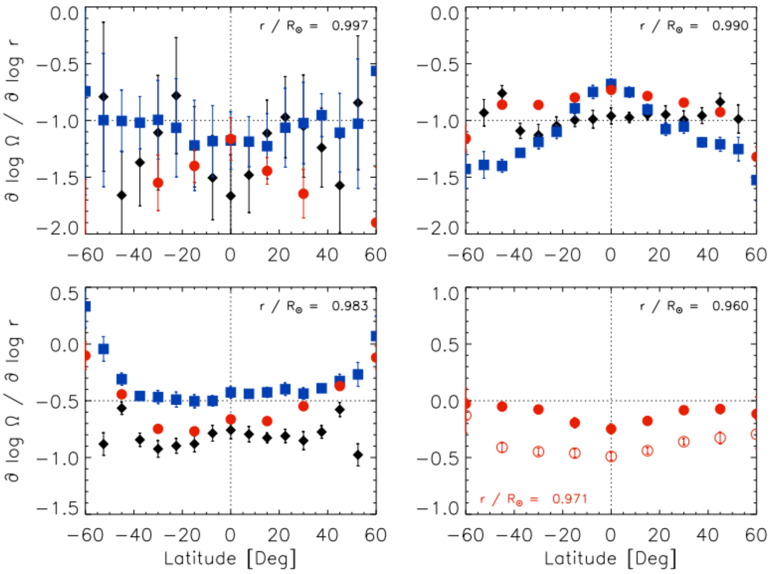

Figure 6*. The radial gradient of the solar rotation rate as a function of latitude at four depths (top-left:* $0.997R_\odot$*, top-right:*$0.990R_\odot$*, bottom-left:* $0.983R_\odot$*, bottom-right:* $0.960R_\odot$*), using 15°-tile Ring Diagram Analysis (RDA) (black diamonds: GONG, blue squares: HMI) and 30°-tile RDA (red circles: HMI) averaged over Solar Cycle 24. The open symbols indicate values at* $0.971R_\odot$ *(bottom-right). (See Komm, 2022).*

Attempts to modelize the NSSL.

From a theoretical point of view the influence of magnetic fields on incident acoustic waves is a complex phenomenon and there is still a need to better understand all the physical processes involved. However, progress in numerical simulations provide new insight in that field. Kitiasvilli et al. (2023) analyze realistic 3D radiative hydrodynamics simulations of solar subsurface dynamics in the presence of rotation in a local domain 80 Mm wide and 25 Mm deep, located at 30° latitude. The simulation results reveal the development of a shallow 10-Mm deep substructure of the Near-Surface Shear Layer (NSSL), characterized by a strong radial rotational gradient and self-organized meridional flows. This shallow layer ("leptocline") is located in the hydrogen ionization zone associated with enhanced anisotropic overshooting-type flows into a less unstable layer between the H and He II ionization zones. Their results, shown in Figure 8, reveal a significant decrease in the azimuthal rotation velocity with depth by 38 m/s in a 2 Mm deep layer below the photosphere. Below 7 Mm, the rotation rate is slower than the imposed mean rotation rate by about 5 m/s. The rotation rate with depth is not uniform: it increases by 6 − 7 m/s per Mm from the sub-photospheric layers to about 4 Mm below, while below 4 Mm, the flow accelerates by about 2 m/s per Mm. So, they identified a 10-Mm thick near-surface shear layer (the leptocline), clearly visible in the relative differential rotation profile. Moreover, their study shows strong negative values of the gradient of rotation, about −4 in subsurface layers, and an increase in the deeper layers (Figure 7). They also evidenced that the outer layers of the NSSL form a distinct substructure characterized by enhanced turbulent convection and strong rotational shear. So, we can argue that the leptocline constitutes the upper part of the Near-Surface Shear Layer, of about 10 Mm thick. The interface between the leptocline and deeper layers is characterized by overshooting downdrafts, which may intensify the turbulent mixing below this layer.

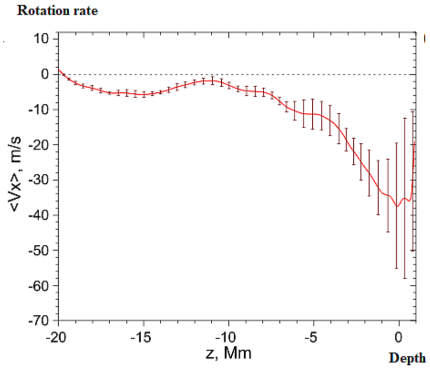

Figure 7. *Theoretical mean radial profiles of deviations of the azimuthal flow speed from the imposed rotation rate at 30° latitude (5m/s). Note the change in the 10 Mm depth below the surface, within the leptocline. Kitiashvili et al. (2023).*

Conclusion.

As pointed out by Reiter et al. (2015) local and global helioseismology[3] has proven to be extremely powerful tools for the investigation of the internal structure and dynamical motions of the Sun. Their combined outcomes show that the structure of the Near Surface Shear Layer

---

[3] The term "global helioseismology" refers either to studies that employ the low- and intermediate-degree p-modes whose lifetimes are truly long enough for them to be globally coherent, or to studies that employ spherical harmonic decompositions that are computed from nearly the entire visible solar hemisphere. Studies that do not use modes that have such long lifetimes or are computed from observations that cover much smaller portions of the visible hemisphere are considered to employ the tools of "local helioseismology" (Reiter et al. 2015).

is now well-resolved, especially for the subsurface rotational shear layer, the leptocline. Results also suggest that the heat transport properties may be significantly different from the predictions of the mixing-length theory.

It can be advanced that the frequency shifts observed in high-degree p-modes (characterizing conditions in the shear layer just below the solar surface) are caused by a combination of strong fields present at the tachocline and weak turbulent fields present in the near-surface shear layer (Kiefer & Roth, 2018). Such an issue has been confirmed by Baird et al. (2024) but should be explored in greater detail in the future.

Hemispheric asymmetry observed in sunspots (and other solar activity proxies) is an important aspect of solar cycles as it provides important clues for understanding dynamical processes in the interior of the Sun. Inceoglu et al. (2017) found that the two hemispheres are decoupled when comparing separately their total magnetic energy. Baird et al. (2024) confirmed that the magnetic activity in each hemisphere evolves independently. As solar activity decreases with time, the amplitude of frequency shifts is also found to decrease in both hemispheres, but more rapidly in the southern hemisphere, indicating that frequency shifts follow this evolution closely. The role of the leptocline in such findings is also certainly to be clarified.

Lastly, the study of the gradient of rotation varies from close to zero at 0.985 R⊙ to steeper than −1 at 0.978 R⊙. The decrease toward zero with greater depth is the same within about 20° latitude, while at latitudes poleward of 40° this decrease is not monotonic. It appears to reverse close to the surface at 0.997 R⊙, indicating that the dominant processes differ at the base of the NSSL and in the leptocline. It also varies with time and could be used as a precursor to detect changes of the solar cycles. Moreover, the change in the steepness of the radial gradient below and above 0.989R⊙ (rapid increase toward the solar surface from 0.986 R⊙ to 0.998 R⊙, and slower decrease with increasing depth below this range) shows a “saddle” point near 0.989 R⊙. This point has been already detected in the non-monotonic variation with depth of the solar radius (see Figure 6). This issue may confirm that the leptocline is constituted of two regimes, that is beginning to be clearly modelized in 3-D.

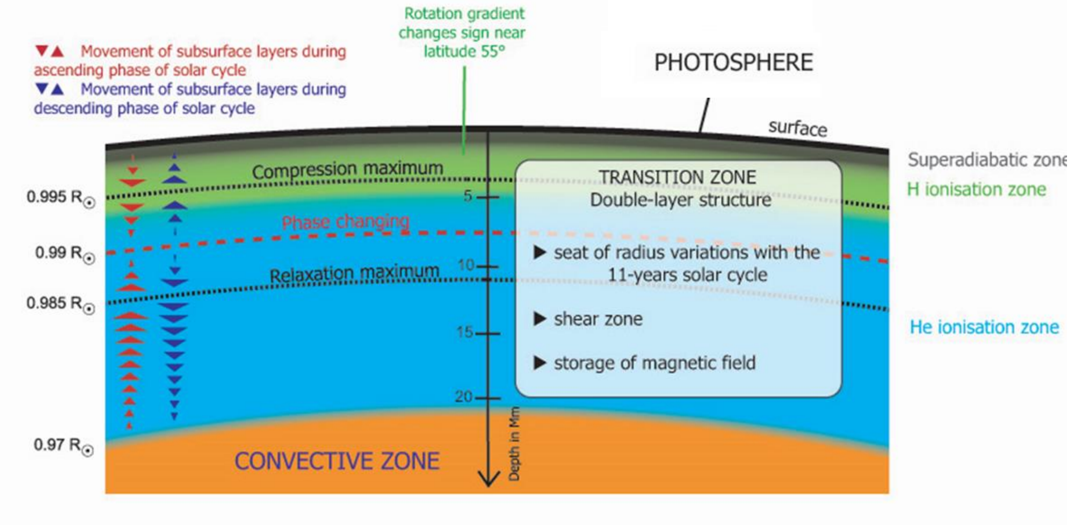

Schematic view of the subsurface layers, transition zone between the convective zone and the photosphere (non-scale scheme). This zone is called “Leptocline” (from the greek "leptos" = thin and “klinô” = slope).

The NSSL is not a homogeneous shear layer. It can be divided at least in two regions; the first part and thickest region, extends from its base (0.958 $R_\odot$, about 30 Mm deep) to around 0.986 $R_\odot$ (10 Mm), and the second part, up to the surface, the leptocline, where the gradient of rotation exhibits highly complex variations in both amplitude and latitude. Based solely on these considerations, Soares et al. (2024) suggests that the leptocline could be could be divided again into two sub-layers: the M layer (for middle one), centered at 0.9965 $R_\odot$ (~2.4 Mm) and the S layer, beginning at 0.9977 $R_\odot$ (~1.6 Mm) up to the surface, being understood that the inversion results are unreliable at layers shallower than ∼1 Mm. However, the leptocline cannot be reduced to highlight the only properties of the rotational gradient as other many physical phenomena take place there (H and He ionization zones for instance), and the superadiabatic region being far to be understood.

As a general conclusion, it is not impossible that the solar-dynamo could take place in the leptocline. Results presented here could be the starting point of systematic further investigations of structure and dynamics in this layer, will lead to a better understanding of the solar activity.

References

Antia, H.M.: 1998. Estimate of solar radius from f-mode frequencies. Astronomy and Astrophysics, vol. 330, pp. 336-340, DOI: 10.48550/arXiv.astro-ph/9707226.

Armstrong, J. and Kuhn, J. R. (1999). Interpreting the Solar Limb Shape Distortions, The Astrophysical Journal, Volume 525, Issue 1, pp. 533-538, DOI: 10.1086/307879.

Baird, Mackenzie A., Tripathy, S. C. and Jain, K. (2024). Connection between Subsurface Layers and Surface Magnetic Activity over Multiple Solar Cycles Using GONG Observations, The Astrophysical Journal, Volume 962, Issue 2, id.194, 19 pp., DOI: 10.3847/1538-4357/ad16db.

Brajša, R. and Hanslmeir, A. (2024). Springer Nature ed., 180 p.

Charbonneau P. (2020). Dynamo models of the solar cycle. Living Rev. Sol. Phys. 17(1), 4, DOI: 10.1007/s41116-020-00025-6.

Choudhuri, A. R., Jha, B.K. (2023). The Near-surface Shear Layer (NSSL) of the Sun: A Theoretical Model, Proceedings of IAUS 365; pp. 4, arXiv:2311.04197 [astro-ph.SR].

Gizon, L., Birch, A.C. and Spruit, H. C. (2010). Local Helioseismology: Three-Dimensional Imaging of the Solar Interior, Annual Review of Astronomy and Astrophysics Vol. 48, pp. 289-338, DOI:10.1146/annurev-astro-082708-101722.

Godier, S. and Rozelot, J. P. (2001). A new outlook on the `Differential Theory' of the solar Quadrupole Moment and Oblateness. Sol. Phys., 199, 217, DOI: 10.1023/A:1010354901960

Hernandez, G., Scherrer, P. and Hill, F. (2009). A new way to infer variations of the seismic solar radius, arXiv:0902.1002v1 [astro-ph.SR], 6 Feb 2009.

Hotta, H., Bekki, Y., Gizon, L., Noratz, Q. and Rast, M. (2023). Dynamics of Large-Scale Solar Flows, Space Science Reviews, 219:77, DOI: 10.1007/s11214-023-01021-6.

Howard, R. and Labonte, B.J. (1980). The sun is observed to be a torsional oscillator with a period of 11 years, Astrophysical Journal Letters, Vol. 239, pp. L33-L36, DOI : 10.1086/183286.

Howard, R.F. (1996). Solar active regions as diagnostics of subsurface conditions, Annual Review of Astronomy and Astrophysics, Vol 34, pp. 75-109, DOI: 10.1146/annurev.astro.34.1.75.

Howe R, Christensen-Dalsgaard J, Hill F et al (2005). Solar convection-zone dynamics 1995-2004. Astrophys J, 634(2), pp1405–1415. https://doi.org/10.1086/497107.

Howe, R. (2009). Solar Interior Rotation and its Variation *Living Rev. Sol. Phys.* **6**, 1, DOI: 10.12942/lrsp-2009-1.

Howe, R. (2020). Solar Rotation. In: Monteiro, M.J.P.F.G., García, R.A., Christensen-Dalsgaard, J., McIntosh, S.W. (eds) Dynamics of the Sun and Stars. Astrophysics and Space Science Proceedings, Vol 57. Springer, , DOI:10.1007/978-3-030-55336-4_8.

Inceoglu, F, Simoniello, R., Knudsen, M. F. and Karoff, C. (2017). Hemispheric progression of solar cycles in solar magnetic field data and its relation to the solar dynamo models, Astronomy & Astrophysics, Vol. 601, id. A51, 8 pp., DOI: 10.1051/0004-6361/201629871.

Javaraiah, J. (2003). "Long-Term Variations in the Solar Differential Rotation", *Solar Physics*, 212 (1): 23–49.

Javaraiah, J. and Gokhale, M.K. (2002). The Sun's rotation, J. Javaraiah and M. K. Gokhale, editors. New York: Nova Science.

Kitchatinov, L.L. (2023). Origin of the Near-Surface Shear Layer of Solar Rotation. *Astron. Lett.* **49**, 754–761 DOI : 10.1134/S106377372311004X.

Kholikov, S. and Hill, F. (2008). Sol. Phys., Vol. 251, Issue 1-2, pp. 157-161, DOI: 10.1007/s11207-008-9205-9.

Kiefer, R. and Roth, M. (2018). The Effect of Toroidal Magnetic Fields on Solar Oscillation Frequencies, The Astrophysical Journal, Volume 854, Issue 1, article id. 74, DOI: 10.3847/1538-4357/aaa3f7.

Kitiashvili, I. N., Kosovichev, A. G., Wray, A. A., Sadykov, V. M. and Guerrero, G. (2023). Leptocline as a shallow substructure of near-surface shear layer in 3D radiative hydrodynamic simulations, Monthly Notices of the Royal Astronomical Society, Vol. 518, Issue 1, pp. 504-512, DOI: 10.1093/mnras/stac2946.

Komm, R. (2022). Radial Gradient of the Solar Rotation Rate in the Near-Surface Shear Layer of the Sun, Frontiers in Astronomy and Space Sciences, Volume 9, id.428, DOI: 10.3389/fspas.2022.1017414.

Kosovichev, A. G., Schou, J., Scherrer, P. H., et al. (1997). Structure and Rotation of the Solar Interior: Initial Results from the MDI Medium-L Program, Solar Physics, 170, 43, DOI: 10.1023/A:1004949311268.

Kosovichev, A.G. and Rozelot, J.P. (2018). Cyclic Changes of the Sun's Seismic Radius, The Astrophysical Journal, Volume 861, Issue 2, article id. 90, 5 pp., DOI:10.3847/1538-4357/aac81d.

Kosovichev, A.G. et al. (2015). Structure and Dynamics of the_Sun's Interior Revealed by Helioseismic and Magnetic Imager, Soar physics, to be published.

Lamy, P., Prado, J.P., Floyd, O., Rocher, P., Faury, G. and Koutchmy, S. (2015). A Novel Technique for Measuring the Solar Radius from Eclipse Light Curves - Results for 2010, 2012, 2013, and 2015. Sol. Physics, Vol. 290, Issue 10, pp.2617-2648, DOI: 10.1007/s11207-015-0787-8.

Larson TP. and Schou J. (2018). Global-mode analysis of full-disk data from the Michelson Doppler Imager and the Helioseismic and Magnetic Imager. Sol Phys 293(2):29, DOI: 10.1007/s11207-017-1201-5.

Lefebvre, S. and Kosovichev, A. G. (2005). Changes in the Subsurface Stratification of the Sun with the 11-Year Activity Cycle, The Astrophysical Journal, Vol. 633, Issue 2, pp. L149-L152, DOI: 10.1086/498305 .

Lefebvre, S. and Kosovichev, A.K. (2007a). Helioseismic Test of Nonhomologous Solar Radius Changes with the 11 Year Activity Cycle, The Astrophysical Journal, Vol. 658, Issue 2, pp. L135-L138, DOI: 10.1086/515394.

Lefebvre, S., Kosovichev, A. G. and Rozelot, J. P. (2007b). Helioseismic Measurements of Solar Radius Changes from SOHO/MDI, SOHO-17. 10 Years of SOHO and Beyond, Proceedings of the conference held 7-12 May, 2006 at Giardini Naxos, Sicily, Italy. Edited by H. Lacoste and L. Ouwehand. ESA SP-617. European Space Agency, 2006. Published on CDROM, id.43

Lefebvre, S., Kosovichev, A. G., Nghiem, P., Turck-Chièze, S. and Rozelot, J. P. (2006). Cyclic variability of the seismic solar radius from SOHO/MDI and related physics. Proceedings of SOHO 18/GONG 2006/HELAS I, Beyond the spherical Sun. See also: Lefebvre, S., Nghiem, P. A. P. and Turck-Chièze, S. (2009). Impact of a radius and composition variation on stratification of the solar subsurface layers, ApJ, 690:1272–1279, DOI: 10.1088/0004-637X/690/2/1272.

M.A., Tripathy, S.C. and Jain, K. (2024). Connection between Subsurface Layers and Surface Magnetic Activity over Multiple Solar Cycles Using GONG Observations. The Astrophysical Journal, 962:194 (19pp), DOI: 10.3847/1538-4357/ad16db.

Mahajan, S.S., Upton, L.A., Antia, H.M. *et al.* (2024).The Sun's Large-Scale Flows I: Measurements of Differential Rotation & Torsional Oscillation. *Sol Phys* **299**, 38, DOI : 10.1007/s11207-024-02282-2.

Modolenvsky, M.S. (1988). Dependence of the gravitational field of the Earth on the changes of its velocity of rotation (in russian), Geodezika i Kartografiya, 5, 11-13.

Rozelot, J.P., Kosovichev, A.K. and Kilcik, A. (2016). Solar radius variations: new look on the wavelength dependence, In Solar and Stellar Flares and their Effects on Planets, Proceedings of the International Astronomical Union, IAU Symposium, Volume 320, pp. 342-350, DOI: 10.1017/S1743921316002118.

Scherrer, P. H., Bogart, R. S., Bush, R. I., et al. (1995). The Solar Oscillations Investigation - Michelson Doppler Imager, Solar Physics, Vol. 162, Issue 1-2, pp. 129-188, DOI :
10.1007/BF00733429.

Scherrer, P. H., Schou, J., Bush, R. I., et al. (2012) Design and Ground Calibration of the Helioseismic and Magnetic Imager (HMI) Instrument on the Solar Dynamics Observatory (SDO), Solar Physics, Solar Physics, Vol. 275, Issue 1-2, pp. 229-259, DOI: 10.1007/s11207-011-9842-2.

Schou, J., Kosovichev, A. G., Goode, P. R. and Dziembowski, W. A. (1997). Determination of the Sun's Seismic Radius from the SOHO Michelson Doppler Imager, Astrophysical Journal Letters, Vol. 489, p. L197, DOI: 10.1086/31678.

Soares, M.C., Basu, S. and Bogart, R.S. (2024). Exploring the Substructure of the Near-surface Shear Layer of the Sun, The Astrophysical Journal, 967:143 (11pp), 2024 June 1, DOI: 10.3847/1538-4357/ad3d59.

Spiegel, E.A. and Zahn, J.P. (1992). The solar tachocline, Astronomy and Astrophysics, 265, pp. 106-114.

Tassoul, J.L. (1979). Theory of rotating stars, Princeton University Press 524 p.

Tassoul, J.L. (2000). Stellar rotation, Cambridge University Press, 24 p.

Tripathy, S., Jain, K., Komm, R. and Kholikov, S. (2021). Subsurface Flow Measurements in the Near Surface Shear Layer over Two Solar Cycles, AGU Fall Meeting, held in New Orleans, LA, 13-17 December 2021, id. SH53C-02.

Vasil, G. M., Lecoanet, D., Augustson, K., Burns et al. (2024). The solar dynamo begins near the surface, Nature, Vol. 629, Issue 8013, pp. 769-772, DOI: 10.1038/s41586-024-07315-1.

Investigation of Potential Sources of Solar Energetic Particles (SEPs)

Tirnakci M.[1]*, Asenovski S.*[2]*, Kilcik A.*[1]

[1]Department of Space Science and Technologies, Akdeniz University Faculty of Science, 07058, Antalya, Turkey, e-mail: meliketirnakci@gmail.com
[2]Space Research and Technology Institute BAS, Sofia, Bulgaria

Abstract

Solar Energetic Particles (SEPs) are one of the key components of space weather, and if they can be predicted; it may be easier to find ways to protect against their negative effects such as single event, satellite drag, communication, etc. SEPs mainly originate from solar flares and coronal mass ejections and it is known that solar flares are strongly related to sunspots. Therefore, first we investigated the solar proton event (SPE) production potential of sunspot groups based on the McIntosh classification system; we examined the solar proton production potential of the Zurich class, type of penumbra and the compactness of groups. Finally, we applied period analysis to SEPs to detect their periodic behavior. Obtained periodicities were compared with well-known solar activity periodicities. Our findings are as follows: i- Sunspot classes; class F has the highest SPE production potential (1.7%), while class B has the lowest potential (0.08%). Penumbra types; class k has the highest SPE production potential (2.02%), while r and x have the lowest (0.04%). Interior spot distribution; class c has the highest SPE production potential (2.32%), while class x has the lowest (0.06%). ii- The 25–34-day periods seen in SEPs show that SEPs are dependent on solar rotation. iii-51-63 days and 221-241 days periodicities were observed. The period of 51-63 days is known as solar flare periodicity, while the period of 221-241 days is known as coronal mass ejection (CME) periodicity.

Keywords: Solar energetic particles; Solar activity; Solar convection.

Introduction

Space weather has gained increasing importance with the development of technology in recent years, enabling more detailed research and a deeper understanding of this field. The most critical source for comprehending space weather is undoubtedly the Sun. Solar phenomena such as sunspots, solar flares, and CME have become better understood thanks to advancements in science and technology. Besides these phenomena, SEPs originating from solar flares and CMEs are an important component of space weather.

SEPs are referred to as accelerated protons, electrons and heavy nuclei, such as He and Fe, in the interplanetary medium and are caused by solar flares and CMEs (Malandraki and Crosby, 2018). There are two particle accelerators thought to be of solar origin in SEPs. One produces impulsive SEPs generated by magnetic reconnection during solar flares or jets, while the other is triggered by shock waves generated by fast CMEs that cause larger gradual SEP events, which produce the highest SEP intensities near Earth (Reames, 2013). High-energy (around 1 GeV) SEP events can result in increased proton fluxes even at ground level (Temmer, 2021). Thus, we can say that SEPs are mostly composed of protons. The main subclass of SEPs that focus only on protons are Solar Proton Events (SPEs) and are characterized by protons >10 MeV. These charged particles can affect the Earth's magnetosphere, ionosphere and life on Earth. These are important phenomena to be taken into account in space weather studies.

Understanding the behavior and origins of SEPs requires a closer look at solar activity, especially sunspots and sunspot groups. Sunspots are transient phenomena that appear as darker spots on the Sun's photosphere compared to the surrounding areas. These regions have strong magnetic fields that reduce the convective flow of plasma, making them cooler than their surroundings (Sahin, 2023). Occasionally, they may also appear in groups on the solar disc. Sunspot groups are defined as the sum of sunspots belonging to the same magnetic flux group. Such regions of strong magnetic field are closely linked to solar activity and have a significant influence on the formation of solar flares and CMEs. Historically, many classification methods have been used to classify sunspot groups such as Cortie, Mount Wilson, Zurich and McIntosh. The McIntosh classification, known as Zpc and Z is the Zurich classification, focuses on sunspot evolution, the parameter p describes the penumbra, and the parameter c indicates the complexity of the sunspot distribution inside a group. Marroquin et al. (2023) carried out research on active regions (ARs) and SEP. They discovered a significant correlation between SEP and several factors: the complexity of the magnetic field of ARs, the longitudinal position of the largest sunspot, the area of ARs, and the type of penumbra.

In this study, we investigated the relationship between SEP, SPE and sunspot groups. The study is organized into four sections: 1. Introduction, 2. Data and Method, 3. Results, and 4. Conclusion and Discussion.

Data and Methods

In this study, SEP, SPE and sunspot groups data of Solar Cycle 23 (SC23) and SC24 were used (1996-2020). As SEP data, the >10 MeV proton flux was used and 128 SPE events for the years 1996-2020 are taken from Space Weather Prediction Center (SWPC, https://www.swpc.noaa.gov/). Sunspot groups were also taken from SWPC and checked on the Solar Monitor webpage (https://www.solarmonitor.org/). All datasets were converted into daily and monthly versions for further analyses.

To fill gaps in the SEP data, we initially applied cubic spline interpolation for periods of less than three days. Next, we examined the temporal variations to compare daily SEP and SPE data and eliminated discontinuities by considering non-SPE days at minimum SPE energy. Then, we calculated cross-correlation coefficient. To further our understanding of SEP sources, we used the Multi-Taper Method (MTM) analysis on the continuous SEP data. The error for significant periods identified through MTM was calculated using the following equation developed by Lou et al. (2003):

$$\Delta P = -P\frac{\Delta\omega}{\omega}$$

where P represents the period, $\Delta\omega$ is the full width at half maximum of the corresponding peak, and ω denotes the frequency. Finally, we classified the sunspot groups from which SPEs originate, including solar flare, CME and filament eruption.

Results

As the first result of our study, the histogram of SEP and SPE is presented in Figure 1. As can be seen from this figure, both SEP and SPE clearly show the sunspot cyclic variation and a very high correlation (r=0.8) with each other.

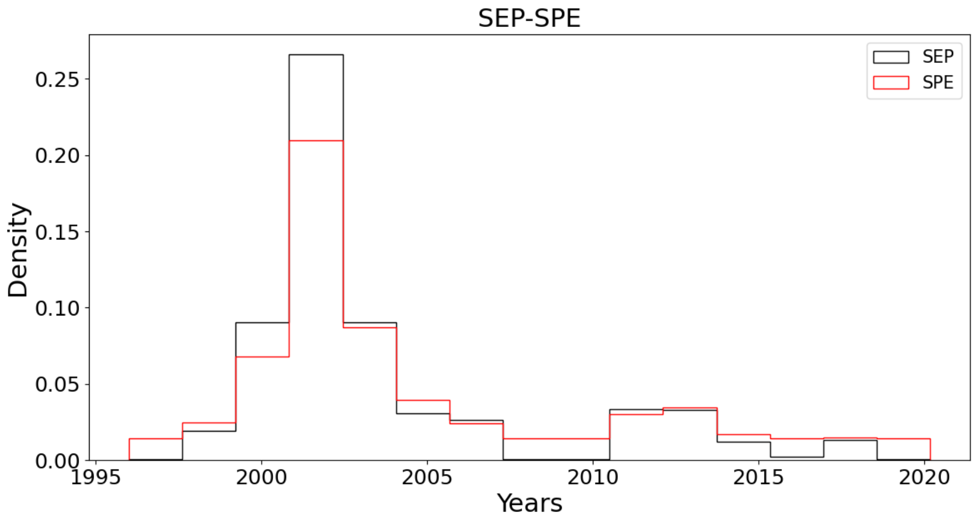

Figure 1. *Histogram plots of SEP and SPE*

However, SEP and SPE number density in SC23 is stronger than SC24. The study by Chandra et al. (2013) has a similar conclusion and suggests that higher density events in SC23 are associated with a higher level of solar activity in that cycle compared to SC24.

Figure 2 shows the MTM analysis result. As a result of the period analysis, significant periods and their significance levels are given in Table 1.

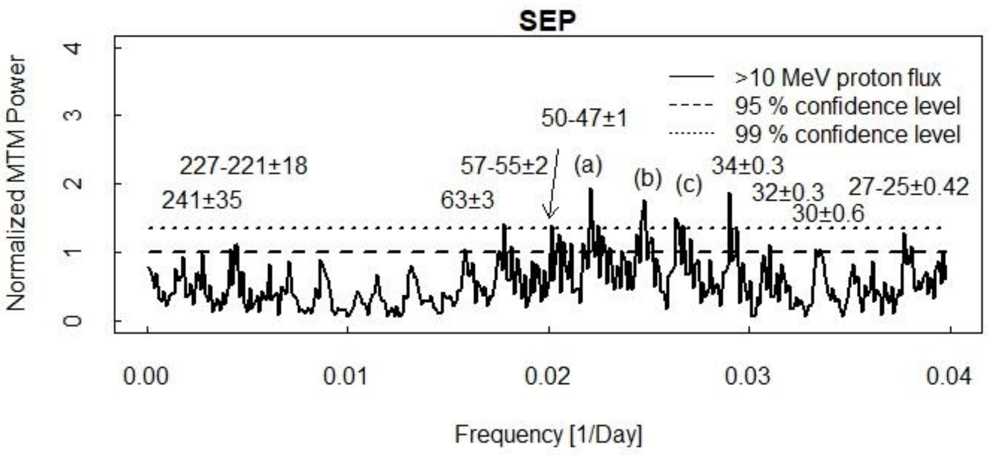

Figure 2. *MTM period analysis power spectrum of SEPs. In Figure;* ***a)*** *45±1;* ***b)*** *42±0.66;* ***c)*** *38-37±1*

Table1. Obtained significant periods and their significance levels.

Period (Days)	SEP
241 (1)	>95%
221-227 (1)	>95%
63 (2)	>95%
55-57 (2)	>99%
47-50 (2)	>99%
45	>99%

42	**>99%**
37-38	**>99%**
34 (3)	**>99%**
32 (3)	**>95%**
30 (3)	**>95%**
25-27 (3)	**>95%**

Specifically, periods 1 denote the CME periods, periods 2 represent the solar flare periods, and periods 3 correspond to the solar rotation periods. It is remarkable that the 356-day and 546-day periods in SEPs are significant at the 90% confidence level. These periods are also characterized by CME activities. However, for the purposes of this study, we have chosen to use a 95% confidence level.

In the final stage of the study, we categorized the SPEs according to the sunspot groups they originated from, as shown in Table 2. This table includes solar flares, CMEs and filament eruptions.

Table 2. Sunspot groups from which eruptive phenomena-induced SPEs originate

p and c parameter **Z parameter**	**x**						**o**						**i**						**c**					
	x	**r**	**s**	**a**	**h**	**k**	**x**	**r**	**s**	**a**	**h**	**k**	**x**	**r**	**s**	**a**	**h**	**k**	**x**	**r**	**s**	**a**	**h**	**k**
A	-	-	-	-	-	-	-	-	-	-	-	-	-	-	-	-	-	-	-	-	-	-	-	-
B	-	-	-	-	-	-	2	-	-	-	-	-	1	-	-	-	-	-	-	-	-	-	-	-
C	-	-	-	-	-	-	-	1	3	5	1	1	-	-	-	-	-	-	-	-	-	-	-	-
D	-	-	-	-	-	-	-	-	3	5	1	4	-	-	1	4	-	9	-	-	2	1	-	7
E	-	-	-	-	-	-	-	-	1	2	-	1	-	-	1	3	1	9	-	-	-	2	1	10
F	-	-	-	-	-	-	-	-	-	-	-	-	-	-	-	1	-	4	-	-	-	-	2	13
H	-	-	4	2	-	-	-	-	-	-	-	-	-	-	-	-	-	-	-	-	-	-	-	-

For instance, there are 13 SPEs originating from the Fkc sunspot group. However, it is important to note that not all proton events occur on the observable solar disk. Some events originate from regions behind the disk or from spotless active regions (see Table 3).

Table 3. SPEs from other sources

SPE Cause	Number
Events not associated with AR	**5**
Spotless AR	**1**
Behind	**7**
Unknown	**7**

In the SPE source shown in Table 2, especially the proton events seen behind the solar disc are numerous.

Discussion and Conclusion

In this study, we have investigated SEP, SPE and related sunspot groups. The findings of our study can be summarized as follows:

- Sunspot class F has the highest SPE production potential (1.7%), while classes B have the lowest potential (0.08%). According to penumbra type, class k has the highest SPE production potential (2.02%), while r and x have the lowest (0.04%). According to the compactness of the interior of the sunspot, class c has the highest SPE production potential (2.32%), while class x has the lowest (0.06%).
- The 25–34-day periods seen in SEPs show that SEPs are dependent on solar rotation.
- 51-63 days and 221-241 days periodicities were observed. The period of 51-63 days is known as solar flare periodicity, while the period of 221-241 days is known as coronal mass ejection (CME) periodicity.

SEPs will continue to be of interest in the coming years as they are an important component of space weather. As they are thought to originate from solar flares and CMEs, analyzing the sunspots from which SEPs originate will provide a better understanding of them. Although the 37-38, 42 and 45-day periods observed in SEPs are not fully explained in the literature, Kilcik et al. (2010) found 37-day periods in SC21 and 42-day periods in SC22 in the flare index data. Therefore, it would not be wrong to associate these periods with solar flare. Bronarska and Michalek's (2017) analyzed of 84 major SEP events revealed that these events typically originate from large bipolar structures (sunspot groups C, D, E, F in the McIntosh classification) and asymmetric sunspots, with the most energetic SEPs exclusively detected from active regions characterized by exceptionally large and complex penumbrae. Additionally, they found that active regions associated with eastern SEP events are larger than those linked to western SEP events, alongside a noted north-south asymmetry in SEPs.

Accurate predictions of such energetic particles will become more and more valuable. Therefore, it is important to extend the scope of the study and to include CMEs and solar flares.

References

Bronarska, K., & Michalek, G. (2017). Characteristics of active regions associated to large solar energetic proton events. Advances in Space Research, 59(1), 384-392.

Chandra, R., Gopalswamy, N., Mäkelä, P., Xie, H., Yashiro, S., Akiyama, S., ... & Nitta, N. V. (2013). Solar energetic particle events during the rise phases of solar cycles 23 and 24. Advances in Space Research, 52(12), 2102-2111.

Kilcik, A., Özgüç, A., Rozelot, J. P., & Ataç, T. (2010). Periodicities in solar flare index for cycles 21–23 revisited. Solar Physics, 264, 255-268.

Malandraki, O. E., & Crosby, N. B. (2018). Solar energetic particles and space weather: Science and applications. Solar particle radiation storms forecasting and analysis: the HESPERIA HORIZON 2020 project and beyond, 1-26.

Marroquin, R. D., Sadykov, V., Kosovichev, A., Kitiashvili, I. N., Oria, V., Nita, G. M., ... & Ali, A. (2023). Statistical study of the correlation between solar energetic particles and properties of active regions. The Astrophysical Journal, 952(2), 97.

Reames, D. V. (2013). The two sources of solar energetic particles. Space Science Reviews, 175, 53-92.

Sahin, S. (2023). An observational investigation of coronal rain in the quiescent and flaring solar corona (Doctoral dissertation, Northumbria University).

Temmer, M. (2021). Space weather: The solar perspective: An update to Schwenn (2006). Living Reviews in Solar Physics, 18(1), 4.

Total Solar Eclipse of 2024 April 8: A Research Expedition to Mexico

Tsvetkov Ts.[1], *Petrov N.*[1], *Minev M.*[1], *Zinkova Y.*[1]

[1]Institute of Astronomy and National Astronomical Observatory, Bulgarian Academy of Sciences, Sofia, Bulgaria; tstsvetkov@astro.bas.bg

Abstract.

Total solar eclipses provide an opportunity to observe the white-light corona out to several solar radii for a few minutes during totality. In addition to the impressive view, this moment is also ideal for conducting a number of experiments to reveal some still-preserved secrets of the Sun and its connection to our planet. Our team organized a research expedition to observe the latest total solar eclipse on 2024 April 8 in Mexico. In this paper we show our investigation methods and share our preliminary results from the latest research expedition.

Keywords: expedition; eclipse; corona;

Introduction

Total solar eclipses (TSEs) are among the most extraordinary astronomical phenomena observable from Earth, captivating both scientists and the general public alike. This celestial event provides a rare opportunity to study various aspects of solar and terrestrial physics. Historically, total solar eclipses have played a pivotal role in advancing our understanding of the solar corona, the outermost part of solar atmosphere. The fleeting moments of totality, when the bright disk of the Sun is completely covered, allow scientists to observe and analyze the coronal structure and behavior without the overwhelming glare of the solar disk.

On 2024 April 8, a TSE traversed North America, crossing Mexico, the United States, and Canada (Figure 1), granting millions of people the chance to witness one of nature's most spectacular displays. First, it allows for direct observations of the solar corona, providing data on its structure, dynamics, and the processes driving solar wind. Second, the eclipse offers a natural laboratory for studying the effects of sudden changes in solar radiation on the Earth's atmosphere, ionosphere, and even biosphere.

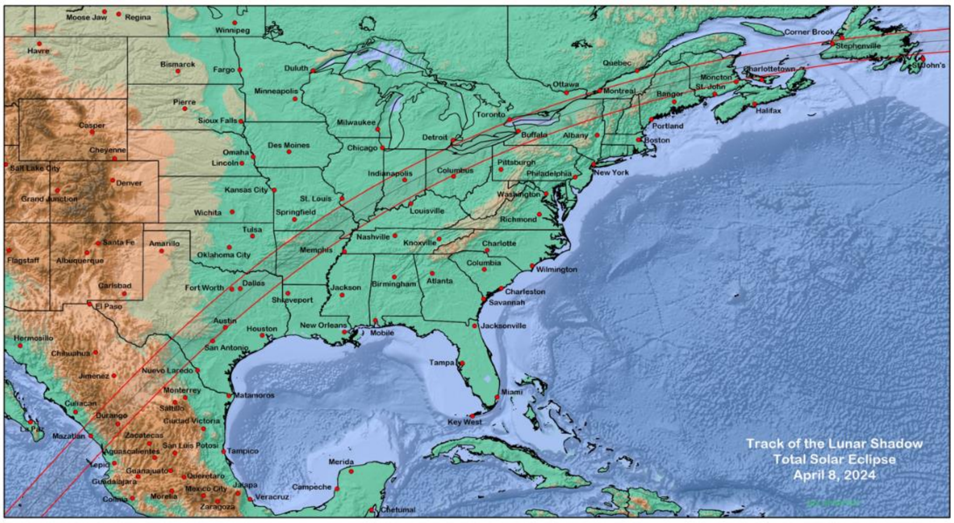

Figure 1. *Topographic map of the track of the eclipse. Source: https://eclipsophile.com/2024tse/*

The maximum duration of the totality was 4 min 28 s (near the Mexican town of Nazas, Durango). Anyway, all preliminary studies regarding the weather conditions confirmed that one of the best places for observations of this eclipse is a bit further from the coast, because of the impact of El Nino on the cloud cover. Using the provided information about the average cloud amount in April along the central axis of the eclipse, our team chose the best observational spot to be located in the surroundings of the town of Monclova (Figure 2).

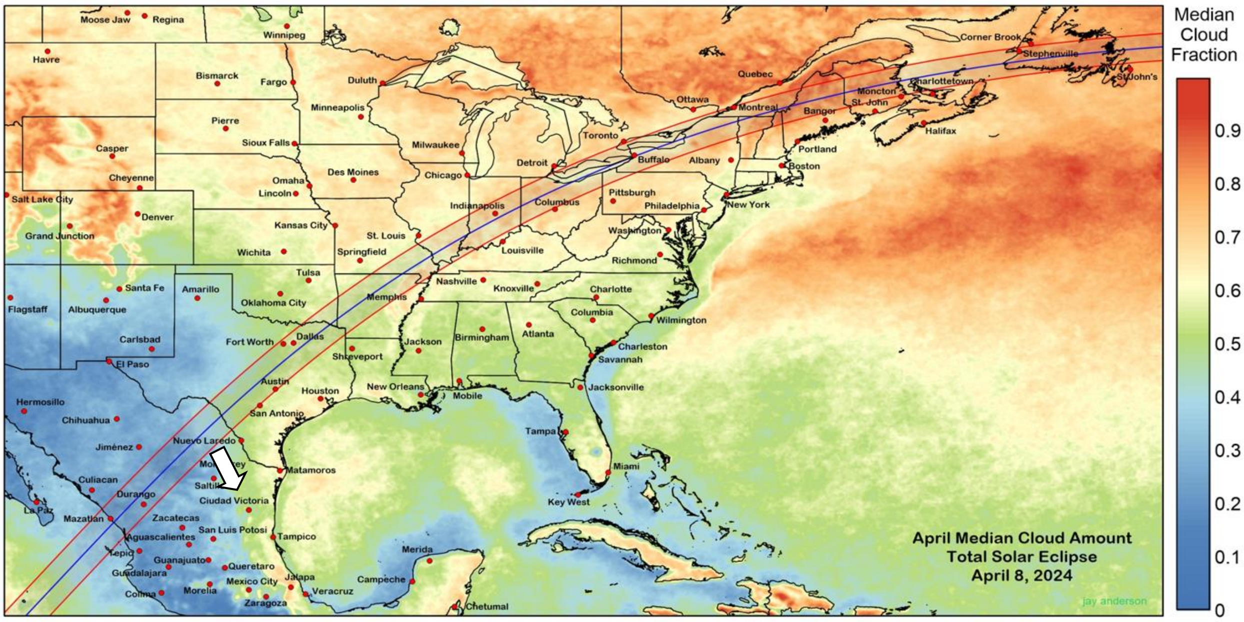

Figure 2. *Average April (2000-2020) cloud cover measured from the Aqua spacecraft (at approximately 13:30 LT). The arrow indicates the approximate position of our team. Data source: NASA. Eclipse track: Fred Espenak (https://eclipsophile.com/2024tse/).*

The chosen spot is outside populated areas, far from city lights and crowds of observers. Its altitude is 650 m. Eclipse details for our location are listed in Table 1.

Table 1. *Eclipse details for the chosen observational area by our team near Monclova (https://www.timeanddate.com/eclipse/solar/2024-april-8).*

Magnitude	**Duration [hh:mm:ss]**	**Duration of the totality [mm:ss]**	**Maximum [LT]**	**Sun's altitude at maximum**
1.0177	02:41:32	04:08	12:24:59	70°

Experiments

The main task of this research expedition was obtaining a new observational data during the TSE on 2024 April 8 from the territory of Mexico. Unfortunately, the weather conditions prevented the optimal realization of the planned experiments. However, the team's efforts during the TSE were directed to the successful implementation of several main tasks:

2.1. Structure and properties of the white-light solar corona

For this experiment, digital cameras with lenses of different focal lengths were used (Figure 3). Combining different frames taken with different exposures and lenses allows obtaining detailed images revealing the fine structure of the solar corona, both in its inner and outer parts [Espenak, 2000].

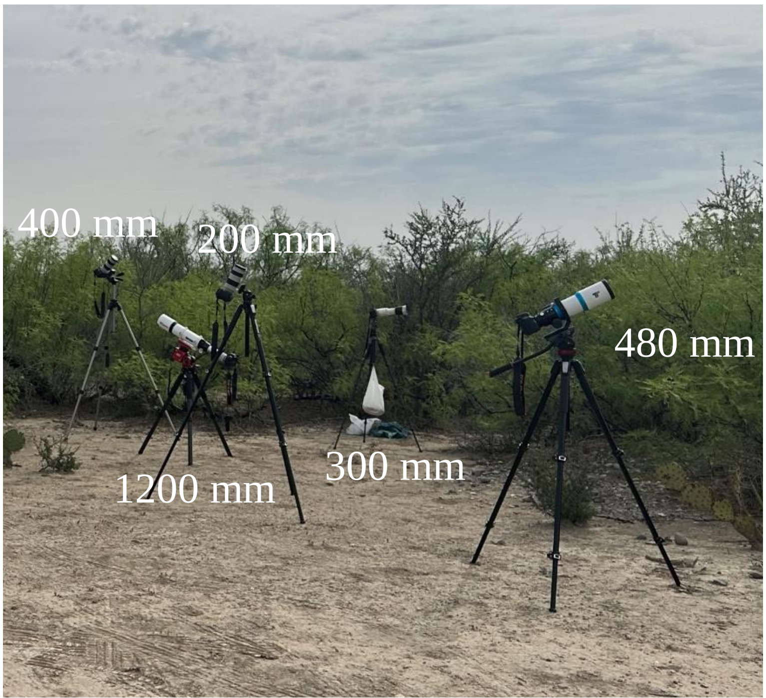

Figure 3. *Instruments, used to implement the planned experiments during the TSE on 2024 April 8 with the focal lengths of different lenses noted.*

Such observations can be used to determine the coronal flattening index (Figure 4) [Ludendorff, 1928] and therefore make a forecast about the maximum monthly sunspot number of the upcoming solar cycle [Pishkalo, 2011]. They can also help to observe the active phenomena in the corona and explore the relations between them. Fiber channels are the places where the quiescent prominences are being formed which we observe on the solar disk as filaments [Martin et al., 1993]. The accompanying coronal structures above them are complicated formations usually located in the base of the coronal streamers. They consist of relatively dark “empty spaces” inside the concentric loop-like structures. The coronal voids are positioned directly over the quiescent prominences and are unstructured and inhomogeneous. Fine, dark fibers are sometimes registered there which can be interpreted as proof of comparatively low-temperature plasma being present.

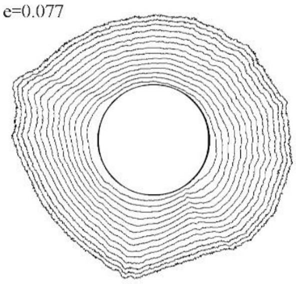

Figure 4. *The flattening of the solar corona and our estimation of the coronal flattening index.*

2.2. Parameters of the polarized solar corona

The intensity of the white-light corona is related to the density of free electrons in it. Polarized-light observations during TSEs hold out possibility for direct definition of the electron density in the corona in order to get a large-scale distribution of the electron concentration. This helps to separate the K and F components of the corona, since at distances less than 3 solar radii from the solar limb, the F-corona (also called dust) is practically unpolarized.

This experiment involved imaging the solar corona with different exposure times with three digital cameras equipped with a polarizing filter – 200, 480, 1200 mm (Figure 3), which allows determination of the degree of polarization in different parts of the corona. The observational data taken with 480 mm lens in 3 positions of the polarizing filter is shown on Figure 5.

Figure 5. *White-light solar corona (from 2024 April 8) captured in three positions of the polarizing*

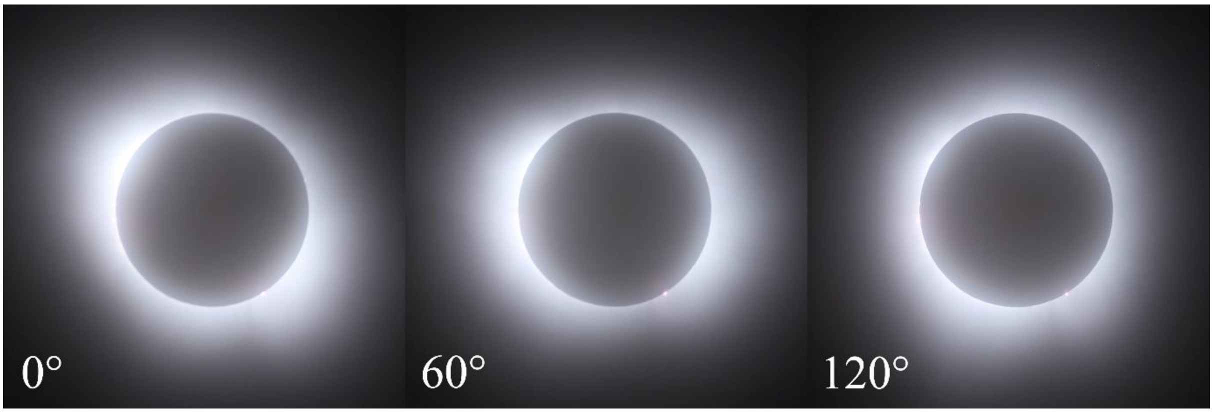

filter (0º, 60º, 120º) with exposure time 1/5 s and focal length of 480 mm.

2.3. Shadow bands and changes in weather conditions during the eclipse

Noticed for the first time as late as 1820 [Guillermier and Koutchmy, 1999], shadow bands are alternating dark and light streaks that "creep" across the Earth's surface in the seconds before and after the totality. A satisfactory explanation for the observed phenomenon was obtained only at the end of the twentieth century by Codona, who realized that the shadow bands are a consequence of the diffraction of the Sun's rays in the turbulent cells of the atmosphere [Codona, 1986]. However, the influence of the ground atmospheric layer and the meteorological conditions during the observation on the pattern of the shadow bands remains not fully understood to this day.

A Sony Alpha 7 digital video camera and a screen were used to capture and determine the speed and direction of the shadow bands before and after the totality. Along with the video recording, we tracked the change of some basic meteorological parameters such as air temperature and humidity, wind speed and direction with a meteorological sensor and an ultrasonic Gill WindSonic anemometer (with a measurement frequency of four times per second), respectively, which are provided in advance. The purpose of the coordinated measurements is to test our hypothesis about the influence of near-surface atmospheric conditions in the patter of the observed shadow bands.

Conclusions

The expedition to observe the total solar eclipse on 2024 April 8 aimed to capture detailed observations of the solar corona, shadow bands and collect data on atmospheric changes during the rare astronomical event. Unfortunately, despite meticulous planning and the selection of an optimal observation site, the expedition faced significant challenges due to unforeseen poor weather conditions, which ultimately hindered the observations of the eclipse.

We successfully obtained white-light observations of the solar corona despite the thin cloud cover during the totality and recorded the meteorological parameters during the eclipse, but the weather conditions made our task of registering the shadow bands impossible.

While the scientific goals of capturing high-resolution images and comprehensive data sets were only partially achieved, the expedition provided important lessons for future eclipse observations. The experience underscored the importance of flexibility and adaptability in scientific endeavors. The data collected still contributed valuable information that will be useful for ongoing research.

The expedition and the accompanying studies and presentations successfully engaged with different social groups and educational institutions, fostering a greater public interest in astronomy and science. Outreach activities, including educational talks and interactive sessions, were well-received and demonstrated the power of celestial events to inspire curiosity and learning.

In conclusion, while the primary scientific objectives of the total solar eclipse observation expedition were not fully realized due to poor weather conditions, the experience provided significant insights and highlighted the need for enhanced planning and adaptability in field research. The lessons learned from this expedition will inform and improve the strategies for future eclipse observations, ensuring that the scientific community can better navigate and mitigate the unpredictable challenges posed by natural events.

Acknowledgment

This work is supported by the National Science Fund of Bulgaria with contracts No. KP-06-M78/1 and KP-06-N64/3, and the national program "Young scientists and postdoctoral fellows-2" (Ministry of Education and Science).

References

Codona, J. L. (1986). The scintillation theory of eclipse shadow bands, A&A, Vol. 164(2), pp. 415–427.

Espenak, F. (2000). Digital Compositing Techniques for Coronal Imaging (Invited review), Last Total Solar Eclipse of the Millennium, ASP Conference Series, Vol. 205. Edited by W. Livingston and A. Özgüç. ISBN: 1-58381-032-3 (2000), p. 101.

Guillermier, P., Koutchmy, S. (1999). Total Eclipses: Science, Observations, Myths and Legends, Springer Publishing, p. 151.

Ludendorff, H. (1928). Sittungsberichte Preuss. Akad. Wiss., Phys.-Math. IClasse Vol. 16, p. 185.

Martin, S. F., Bilimora, R. and Tracadas, P. W. (1993). Magnetic Field Configurations Basic to Filament Channels and Filaments, Bulletin of the American Astronomical Society, Vol. 25, p. 1217.

Pishkalo, M. (2011)., Flattening Index of the Solar Corona and the Solar Cycle, Sol. Phys., Vol. 270, p. 347.

Moderate Magnetic Storm Expected as a Typical Space Weather Event in the Era of the Decreased Solar Activity

Gromova L.I.[1]*, Kleimenova N.G.*[2]*, Gromov S.V.*[1]*, Malysheva L.M.*[2]

[1]IZMIRAN, Moscow, Troitsk, Russia; gromova@izmiran.ru
[2]Schmidt Institute of Physics of the Earth RAS, Moscow, Russia

Abstract

The 25th cycle of solar activity (SA) is the second one in the epoch of decreased SA when the geomagnetic activity become lower year by year. Really, the number of intense magnetic storms in the 23rd, 24th, and approaching its maximum in the 25th SA cycle is decreased. Thus, moderate magnetic storms (50 < |*SymH*| <100 nT or G2-storms) become the most expected events of the space weather. Here we discuss the behavior of the magnetic storm on September 12, 2023 as an example of a typical moderate magnetic storm. Our study was based on the analysis of the global maps of ionospheric and field-aligned currents obtained from magnetic measurements on 66 low-orbit AMPERE project satellites and electrons and ions data from DMSP satellites as well as the ground-based magnetic data from the Scandinavian IMAGE profile and Intermagnet. It was shown that the initial phase of the magnetic storm was characterized by daytime polar-latitude geomagnetic disturbances and the storm main phase was associated with nighttime substorms in auroral latitudes accompanied by positive magnetic bays at the middle latitudes. It was supposed that such magnetic storms caused by both magnetic clouds or high-speed streams from coronal holes, could be the most expected phenomena in the near future.

Keywords: Solar activity; Magnetic storm; Substorm.

Introduction

The current 25th cycle of the solar activity is the second cycle in the era of decreased solar activity, which, according to forecasts, can last until the mid-70s of the 21st century [Ishkov, 2023]. During such an era, the level of geomagnetic activity decreases and the number of intense magnetic storms reduces. As it is shown in [Selvakumaran et al., 2016] the reduced geoeffectiveness in the solar cycle 24 comparing to the cycle 23 occurs mainly due to the decrease in the intense storms and to a smaller extent in the number of moderate storms. A decrease in the number of intense magnetic storms is also noted in 25th cycle that is demonstrated in Table 1 from [Gopalswamy et al., 2023].

Table 1. *Number of intense storms during the first 41 months of solar cycles 23-25.*

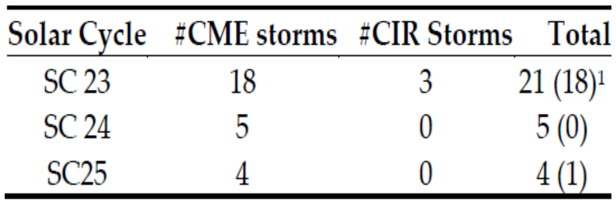

Solar Cycle	#CME storms	#CIR Storms	Total
SC 23	18	3	21 (18)[1]
SC 24	5	0	5 (0)
SC25	4	0	4 (1)

[1]The numbers in the parentheses of this column correspond to the rise phase.

The days with magnetic storms decreased from cycle to cycle and the proportion of days of moderate magnetic storms increased, for example, see as it is shown in Figure 1.

Thus, we could expect that *moderate* magnetic storms may be the most typical space weather events in an era of decreased solar activity.

The aim of our work is to study the spatiotemporal distribution of substorm geomagnetic disturbances during the typical *moderate* magnetic storm as a storm which may be the most expected event at an early date. For our study we chose the magnetic storm on September 12, 2023.

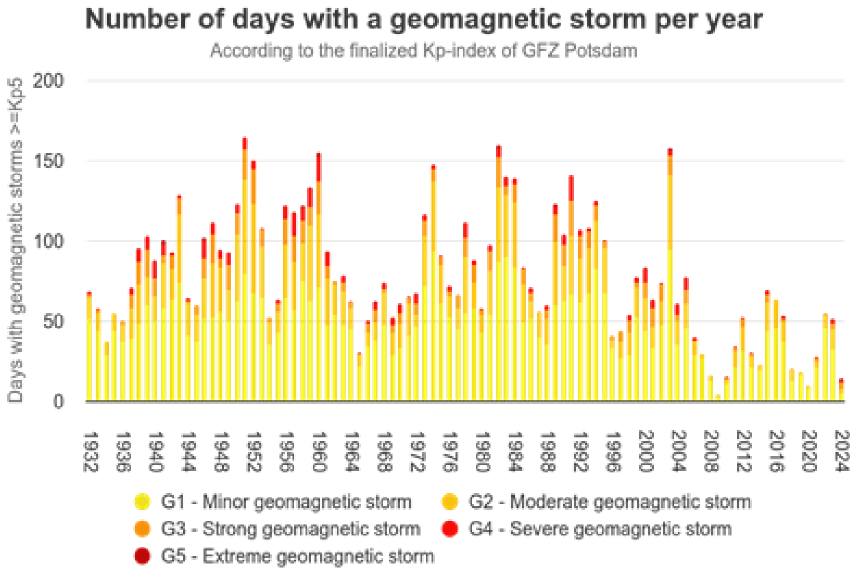

***Figure 1**. Number storm days in 20-25th solar activity cycles.*
From https://www.spaceweatherlive.com

Data

In our study we used the ground-based magnetic data from the Scandinavian IMAGE (https://space.fmi.fi/image/) and Intermagnet (https://imag-data.bgs.ac.uk/GIN_V1/) networks, as well as global maps of ionospheric and field-aligned currents obtained from AMPERE project (https://ampere.jhuapl.edu/) and electrons and ions data from DMSP (https://dmsp.bc.edu/).

AMPERE project is based on simultaneous magnetic measurements on 66 low-orbit satellites. The processing of the satellite data averaged over a 10-minute interval allows to analyze the global distribution of ionospheric and field-aligned currents. The maps are generated at 2-minute intervals. We assign each map to the middle of the averaging 10-min interval. Note, that AMPERE satellite data can represent the real planetary distribution of geomagnetic activity, which we cannot derive from ground-based data, since the stations are unevenly spaced due to large ocean expanses, and/or due to the lack of observation points (for example, in Siberia).

Variation of the Interplanetary Magnetic Field (IMF) and the solar wind parameters were proceeded from OMNI database http://omniweb.gsfc.nasa.gov, *PCN*-index values were obtained from http://pcindex.org.

We studied substorm activity in the magnetic storm basing on the analysis of the *AL*-index data from http://wdc.kugi.kyoto-u.ac.jp.

Magnetic storm on September 12, 2023

This *moderate* magnetic storm (G2, Kp_{max} = 5+) was noted as a response of the passage of three consecutive high-speed streams of the solar wind from coronal holes. [https://www.izmiran.ru/services/saf/archive/]. It was preceded by a long magnetically quiet period (Figure 2).

As it is shown in Figure 3 the magnetic storm began after the SC with a short (~3 hours) initial phase, when the solar wind dynamic pressure *Psw* (speed *V*, density *Np*) increased significantly, and the IMF components *Bz* and *By* varied slightly and remained negative. After

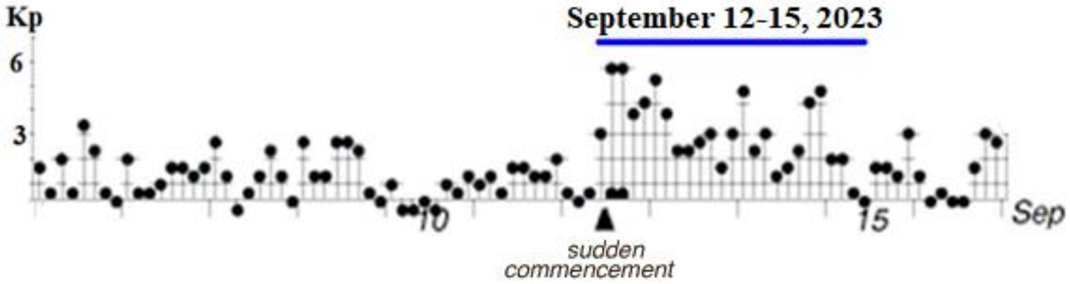

Figure 2. *Geomagnetic activity on September 6 – 16, 2023 by Kp-index. From https://kp.gfz-potsdam.de*

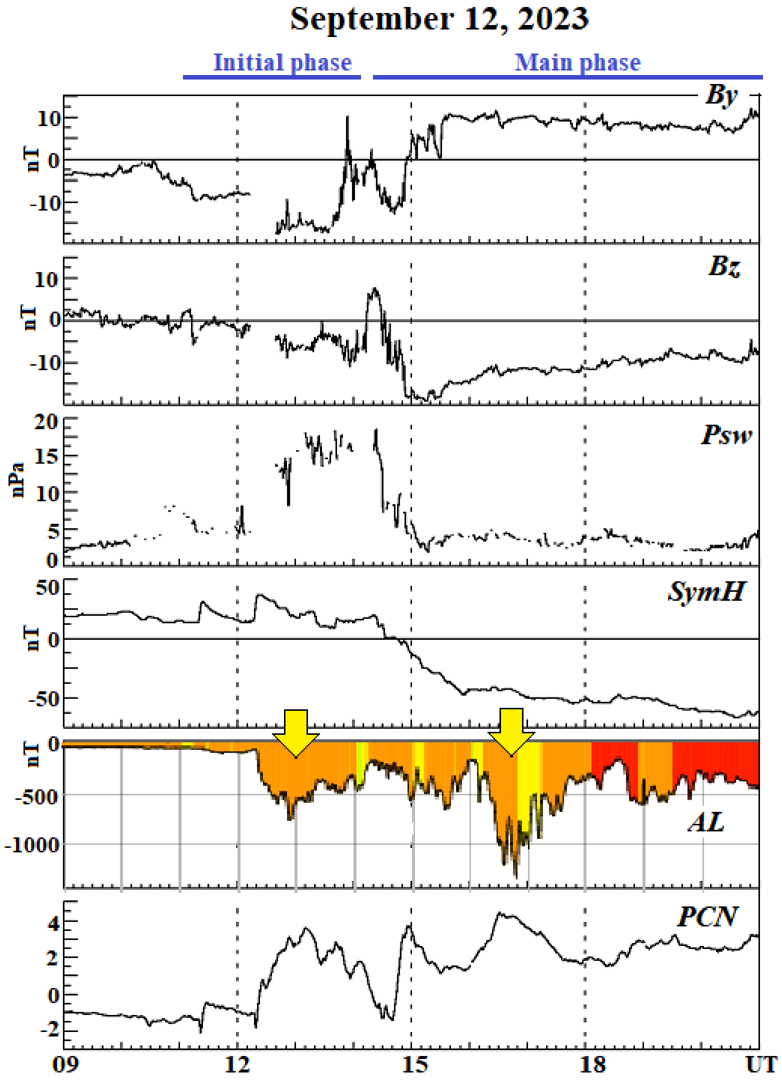

Figure 3. *The variation of the IMF and solar wind parameters, planetary indices SymH – index of the storm, Al - index of the auroral activity and PCN –index of geomagnetic activity in the Northern polar cap. Yellow arrows point the substorms under consideration.*

a sharp positive impulse and a rapid drop of the IMF *Bz* component and a simultaneous sharp decreasing of *Psw*, the main phase of the storm began and developed under the gradually decreasing negative IMF *Bz*, positive IMF *By* and a consistently small *Psw*.

Magnetic storms are typically accompanied by substorms [Akasofu and Chapman, 1963], and stronger storm are accompanied by more intense substorms [Feldstein et al., 1997], due to the southern component of the interplanetary magnetic field (the IMF $Bz < 0$) as both phenomena cause. As it is seen in Figure 3 the IMF *Bz* was negative both in the initial and main phase of the magnetic storm.

In the initial phase of the magnetic storm, one can observed the isolated substorm with *AL*–index-about -750 nT (~13:00 UT). During the main phase, which began with a sharp drop in the values of the southern IMF *Bz* component till -20 nT, an intense substorm was observed with *AL*-index -1400 nT (~16:50 UT). An increase in the *PCN*-index before each substorm indicates the increasing input of energy from the solar wind into the magnetosphere.

Thus, unexpectedly the considered *moderate* magnetic storm was accompanied by *high* substorm activity.

Substorm development in the initial and main phases of the magnetic storm

Figure 4 shows magnetograms of stations where we observed substorm development in the initial and main phase of the storm. Figure 4a shows the data from Scandinavian meridian profile of IMAGE network located the same longitudinal sector at MLAT 57-78°, approximately at the same longitude, MLT = UT+2.7. In Figure 4b one can see the magnetograms from some high-latitudes stations of the American sector: BRW (70°, MLT =

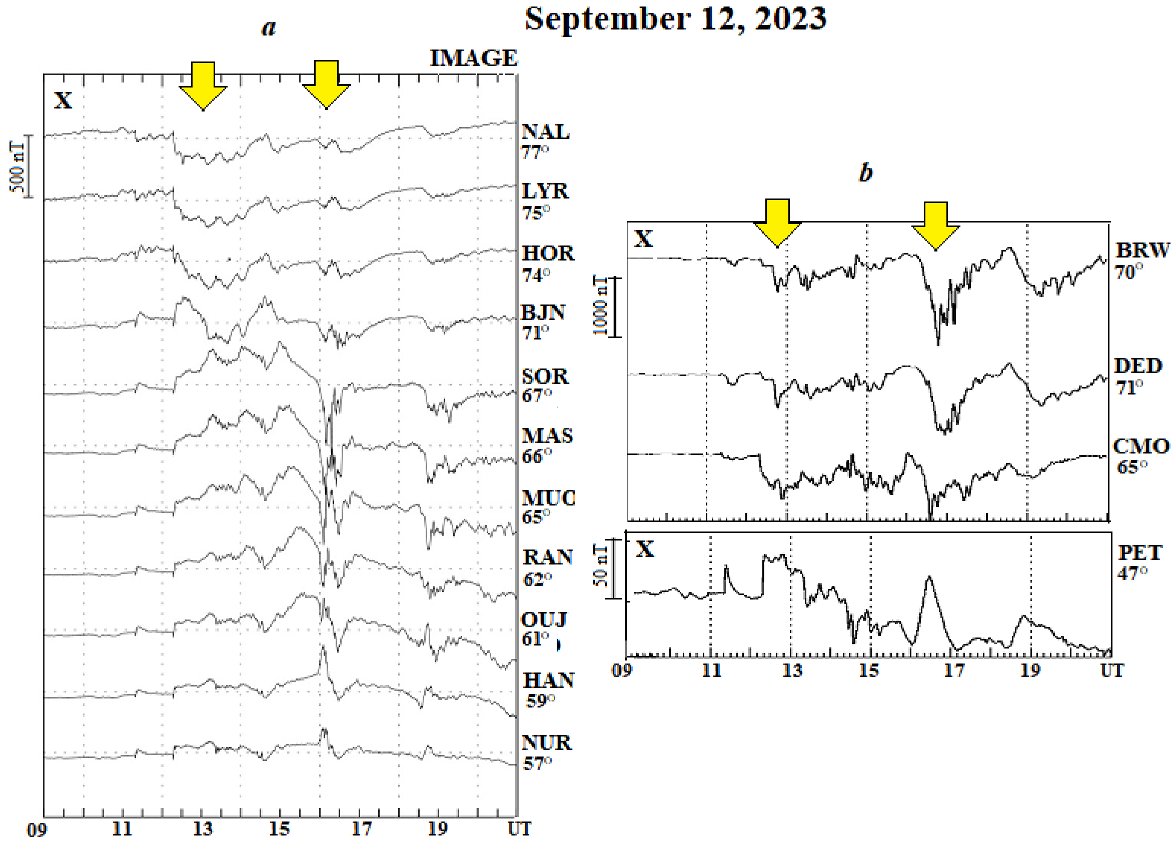

Figure 4. *Magnetograms of IMAGE profile stations (a) and high latitude stations of American sector and Russian mid latitude stastion PET (b). Yellow arrows point the substorms under consideration.*

UT-12), DED (71°, MLT = UT-11), CMO (65°, MLT = UT-10), and from Russian mid-latitude station PET (47°, MLT=UT-14) located approximately near this longitudinal sector.

Global distributions of the eastward and westward electrojets and field-aligned currents and spectrograms of DMSP in the maximum of the substorm in the initial (~13:00 UT) and main phase (~16:40 UT) of the magnetic storm are demonstrated in Figure 5 and Figure 6 correspondingly.

The dayside disturbances in the initial storm phase

In the initial phase of the storm, the daytime negative magnetic bays were observed in the *X*-component of the geomagnetic field, were recorded at some polar stations in Scandinavia (Figure 4a). These bays were accompanied by the precipitation of electrons and ions into the ionosphere (Figure 5c) and counterclockwise ionospheric vortex in the afternoon sector. One can see the development of an eastward electrojet i.e. increasing of the upward field-aligned currents (Figure 5b) in the same sector of the high latitudes.

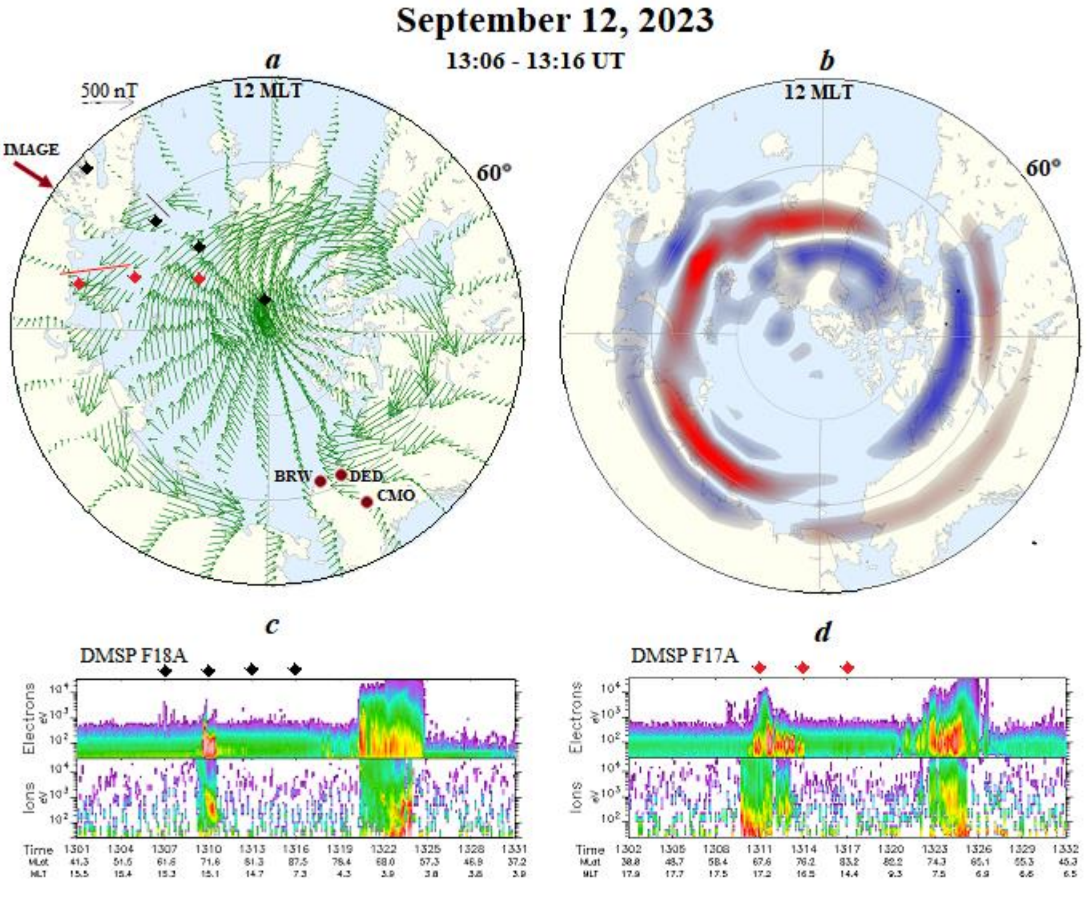

Figure 5. *AMPERE maps electrojets (a) and field-aligned currents (b) in the maximum of intensity of the substorm in the initial phase of the storm; spectrograms of DMSP F18A (c) and F17A (d) during the considered interval. Red arrow point the IMAGE meridian, red circles point the location of the station of American sector, rhombus (black one for F18A, red one for F17A) on the maps mark satellite passes, thin lines show approximate area of particle precipitation measured by DMSP.*

At the same time, in the early morning sector, a substorm developed at MLAT-latitudes ~65°, accompanied by positive bays at mid-latitudes (Figure 4b). This is evidence of the formation of substorm current wedge, which is one of the main features of substorm development [Kepko et al, 2015].

The substorms in the main storm phase

During the main phase of the magnetic storm, the intense magnetospheric substorm was observed in the post-midnight sector of the auroral latitudes (BRW, DED, CMO). One can see strong eastward electrojet and the development of positive mid-latitude magnetic bays as well as an intensification of the morning clockwise vortex, i.e. enhancement of field-aligned currents, that is typical for the development of very intense substorms and supersubstorms.

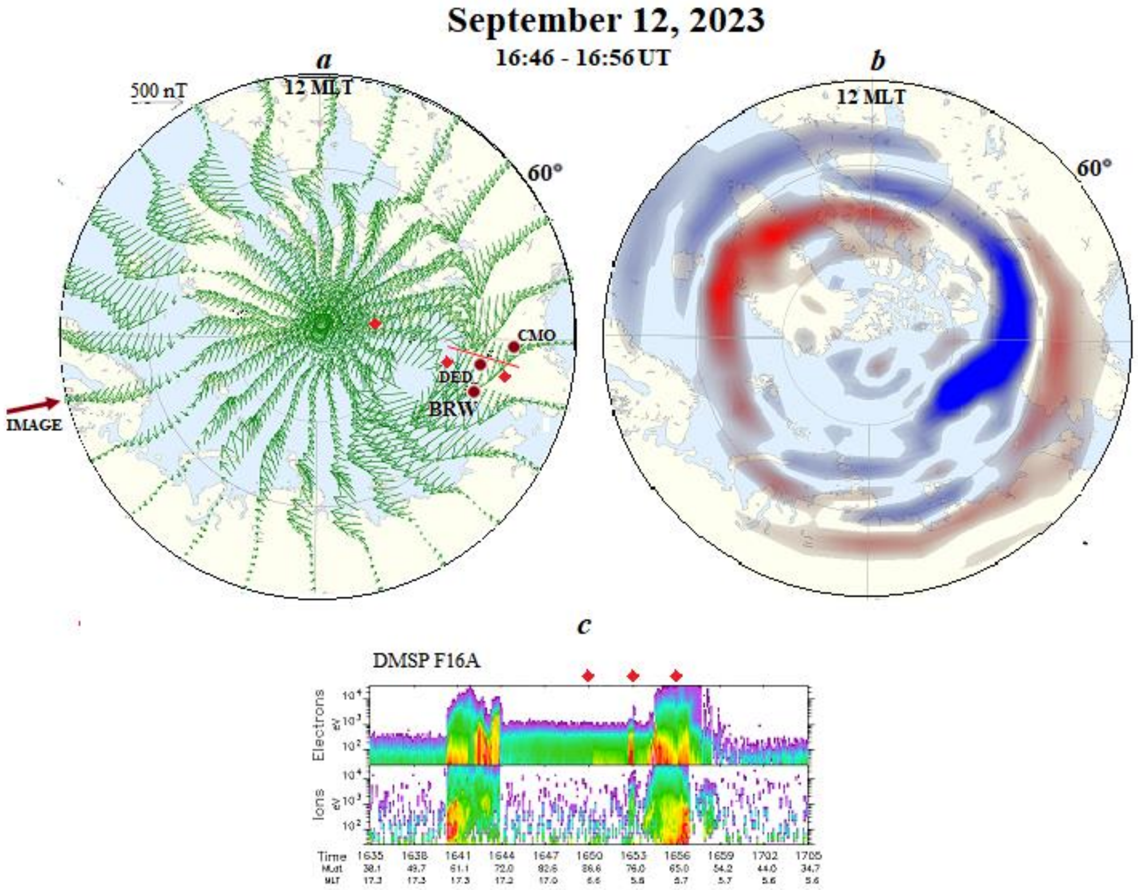

***Figure 6**. AMPERE maps electrojets (a) and field-aligned currents (b) in the maximum of intensity of the substorm in the main phase of the storm; spectrograms of DMSP satellite F16A during the considered interval. Red arrow point the IMAGE meridian, red circles point the location of the station of American sector, red rhombus on the maps mark satellite pass, thin lines show approximate area of particle precipitation measured by F16A.*

Discussion

The similar features were observed during some other *moderate* magnetic storms of the 25th SA cycle. They were characterized by high substorm activity: intense isolated substorms (up to -1000 nT) in the initial phase after a long interval of magnetically quiet conditions and very intense (up to -1500 nT) in the main phase of the storm as one can see in Figure 7. The occurrence of such strong substorms in the main phase of these *moderate* storm looks like similar to the development of supersubstorms - which are typical for much intense magnetic storms [e.g., Hajra et al., 2016; Despirak et al., 2019].

This contradicts the previously published in [Feldstein et al., 1997] a linear relationship between the intensity of the storm and substorms in the storm main phase This result was based on the assumption that the negative IMF *Bz* is the main driver of magnetic disturbances. But now the solar wind dynamic pressure is generally accepted as the second important driver particularly during the periods of the negative IMF *Bz* [Tsurutani and Zhou, 2003; Li and Peng, 2013 and references therein].

Really, our study demonstrated an emerging of substorm activity under the strong negative IMF *Bz* and gradual increase of the solar wind dynamic pressure.

However, the role of the solar wind pressure enhancement in the substorm generation is not sufficiently studied. For example, Sinha et al. [2023] believes that “scenario of substorm onset is simple when the southward component of IMF is present prior to the onset or when just a pressure pulse coincides with the onset. It may be a complex task to understand the behavior of substorm when both the triggering agents are present.”

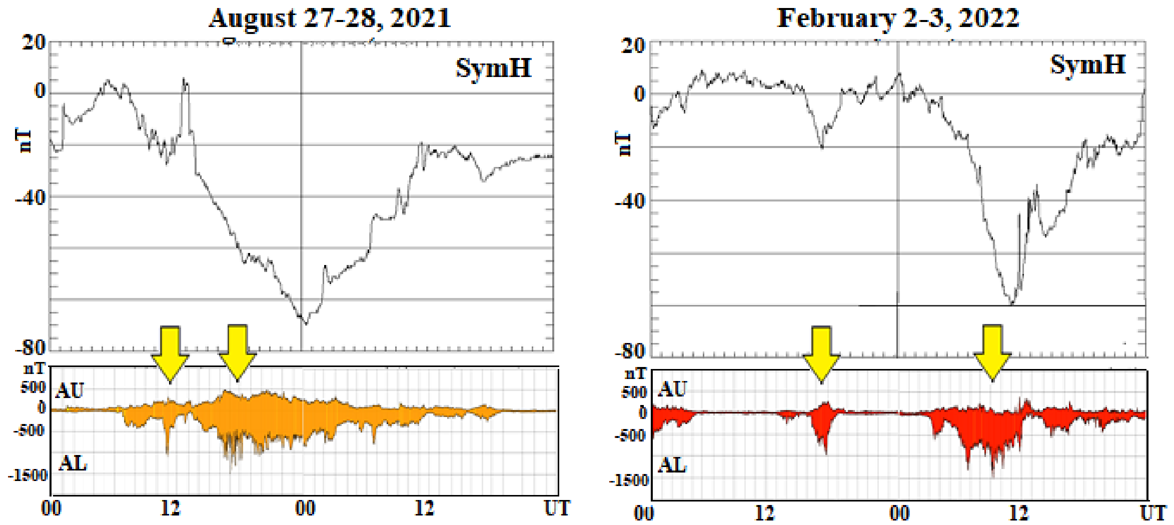

Figure 7*. Moderate storms of 25th cycle of the solar activity which are characterized by high substorm activity in the initial and main phases of the storm. Substorms are pointed by yellow arrows.*

Conclusion

The spatio-temporal distribution of substorm activity was studied during one of the typical *moderate* magnetic storms, as the most expected storm in the near future.

One of main feature of such storms is the appearance of fairly intense substorms, despite the relatively small values of the intensity of the ring current that is shown by *Dst*- (*SymH*-) index.

The scenario of substorms developed in the main phase of a considered *moderate* storm is similar to the scenario of very intense substorms and supersubstorms, which are typical for storms of much higher intensity.

We assume that the solar wind dynamic pressure plays an important role in the development of substorm under the southward *Bz* component of IMF.

References

Akasofu, S.-I, Chapman, S. (1963). The development of the main phase of magnetic storms, J. Geophys. Res., Vol. 68, pp. 125–129, https://doi.org/10.1029/jz068i001p00125

Despirak, I.V., Lyubchich, A.A., Kleimenova, N.G. (2019). Supersubstorms and conditions in the solar wind, Geomagn. Aeron., Vol. 59, pp**.** 170–176, https://doi.org/10.1134/S0016793219020075

Feldstein, Y. I., Grafe, A., Gromova, L. I., Popov, V. A. (1997). Auroral electrojets during geomagnetic storms, J. Geophys. Res., Vol. 102, pp. 14223–14235, https://doi.org/10.1029/97JA00577

Gopalswamy, N. et al. (2023). Intense Geomagnetic Storms during Solar Cycles 23-25, Proceedings of the Fifteenth Workshop “Solar Influences on the Magnetosphere, Ionosphere and Atmosphere”, pp. 47-55, https://doi.org/10.31401/WS.2023.proc

Hajra, R., Tsurutani, B.T., Echer, E., Gonzalez, W.D., Gjerloev, J.W. (2016). Supersubstorms (SML < -2500nT): Magnetic storm and solar cycle dependences, J. Geophys. Res, Vol. 121, No. 8, pp. 7805-7816, https:/doi.org/10.1002/2015JA021835

Ishkov, V.N. (2023). Medium-Sized Solar Cycles in Different Epochs of Solar Activity, Geomagn. Aeron., Vol. 63, pp. 1024–1030, https://doi.org/10.1134/S0016793223070101

Kepko, L., McPherron, R. L., Amm, O., Apatenkov, S., Baumjohann, W., Birn, J., Lester, M., Nakamura, R., Pulkkinen, T. I., Sergeev, V. (2015). Substorm current wedge revisited, Space Sci. Rev., Vol. 190, pp. 1–46, https://doi.org/10.1007/s11214-014-0124-9

Li, H., Wang, C., Peng, Z. (2013). Solar wind impact on growth phase duration and substorm intensity. J Geophys Res Vol. 118, pp. 4270–4278, https ://doi.org/10.1002/jgra.50399

Selvakumaran, R., Veenadhari, B., Akiyama, S., Pandya, M., Gopalswamy, N., Yashiro, S., Kumar, S., Mäkelä, P. and Xie, H. (2016). On the reduced geoeffectiveness of solar cycle 24: A moderate storm perspective, J. Geophys. Res. Space Physics, Vol. 121, pp. 8188–8202, https://doi.org/10.1002/2016JA022885

Sinha, S., Vichare, G., Sinha, A.K. (2023). Comparative analysis of the role of interplanetary magnetic field (IMF) and sudden impulse (SI) in triggering a substorm. Advances in Space Research, Vol. 71, No. 1, pp. 97-114, https://doi.org/10.1016/j.asr.2022.08.037

Tsurutani, B. T., & Zhou, X.-Y. (2003). Interplanetary shock triggering of substorms: WIND and POLAR. Advances in Space Research, Vol. 31, No. 4, pp. 1063–1067, https://doi.org/10.1016/S0273-1177(02)00796-2

Proceedings of
the Sixteenth Workshop “Solar Influences on the Magnetosphere, Ionosphere and Atmosphere”
June, 2024

Analysis of Substorms Related to Strong MPB at Panagjurishte Station in 2022

Guineva V.[1], Werner R.[1], Bojilova R.[2], Raykova L.[1], Atanassov A.[1], Valev D.[1]

[1]Space Research and Technology Institute (SRTI) – Bulgarian Academy of Sciences, Stara Zagora Department, Bulgaria; v_guineva@yahoo.com
[2]National Institute of Geophysics, Geodesy and Geography (NIGGG) - Bulgarian Academy of Sciences, Sofia, Bulgaria

Abstract

Substorms developed over Europe are often accompanied by midlatitude positive bays (MPB) which represent peaks in the X magnetic component at midlatitudes. The present study aims at revealing the interplanetary and geomagnetic conditions under which develop magnetospheric substorms responsible for strong MPB at the Bulgarian magnetic station Panagjurishte. In this purpose, the 153 MPB’s in 2022 determined as appreciable effect of auroral substorms, are examined. 14 MPB’s with maximal X values greater than 20 nT are taken into account. The beginning times of these MPB’s are close to the substorm onsets determined from the SML index by Newell and Gjerloev (2011), Forsyth et al. (2015) and Ohtani and Gjerloev (2020). The interplanetary and geomagnetic conditions during the studied substorms have been verified. It was found out that these substorms occurred against the background of different structures in the solar wind related to high speed streams from coronal holes or coronal mass ejections. Under such disturbed interplanetary conditions, in all studied cases magnetic storms developed, the majority of which are between the top 50 geomagnetic storms of 2022.

Keywords: Midlatitude positive bays; Interplanetary and geomagnetic conditions; Panagiurishte magnetic station

Introduction.

Magnetospheric substorms are a substantial element of the space weather. The principle disturbances of the Earth’s magnetosphere are due to the substorms development. After the present-day theory, during magnetospheric substorms, a current system forms, namely the so-called Substorm current wedge (SCW) [e.g. McPherron, 1972; McPherron et al., 1973a], by the deviation of the tail current along the magnetic field lines through the ionosphere and the formation of auroral electrojets, in the east and west direction. The auroral electrojets have been investigated since 1970s [e.g. McPherron et al., 1973b, Kisabeth and Rostoker, 1974]. The substorm current wedge is responsible for the main disturbances in the Earth magnetic field: negative bays of the X-component at auroral latitudes and positive bays of X at midlatitudes (midlatitude positive bays – MPB), which accompany the expansion of the magnetospheric substorms [e.g. McPherron, 1972; Kepko et al., 2014]. The magnetic disturbances at the Earth surface have been used in a number of studies of the magnetospheric substorms. The midlatitude magnetic variations are a powerfull tool for the magnetospheric substorms investigation. The MPB’s are a good indicator of the substorm onset [McPherron and Chu, 2017], and the sign of Y component was used to estimate the direction of the field aligned currents at a given longitude [Meng and Akasofu, 1969].

The magnetospheric substorms may be accompanied or not with magnetic disturbances at midlatitudes. The presence and strength of the midlatitude magnetic disturbances aroused by magnetospheric substorms, depend on the substorm strength, the measuring point location (distance from the substorm meridian and geomagnetic latitude), and also on the interplanetary and geomagnetic conditions.

The purpose of this work is to verify the interplanetary and geomagnetic conditions during substorms, which caused strong MPB at the Bulgarian magnetic station Panagjurishte. For this, the detected MPB's in 2022 based on the Catalog of the magnetic variations at the Panagjurishte station [Guineva et al., 2023a, Guineva et al., 2023b, Guineva et al., 2023c] have been used.

Data used.

For the study, data from the Catalog of the magnetic variations at the Panagjurishte station (PAG) (~37° GMLat, ~97° GMLon), created at the Space Research and Technology Institute of the Bulgarian Academy of Sciences, have been used. The catalog is available at: http://space.bas.bg/Catalog_MPB/. Data from 2022 were examined.

The interplanetary and geomagnetic conditions have been verified by data of OMNI database of the Coordinated data analysis Web (https://cdaweb.gsfc.nasa.gov/) and the Catalog of large scale solar wind phenomena (http://www.iki.rssi.ru/pub/omni/catalog/).

To compare the results for the substorms by the MPB's, registered at PAG, with other results of substorms over Europe at the same time, the substorm lists by Newell and Gjerloev (2011), Forsyth et al. (2015) and Ohtani and Gjerloev (2020) have been used, available in the SuperMAG database (https://supermag.jhuapl.edu/substorms/?tab=description), as well as IL index data from IMAGE database (https://space.fmi.fi/image/www/il_index_panel.php).

1.1.Data from the Catalog of the magnetic variations at PAG.

For the study, data from the section "Data about MPB", namely from the subsections "Yearly lists", "MPB parameters" and "MPB graphs" of the Catalog for 2022 have been used [Guineva et al., 2023b]. The time interval from 18 UT to 24 UT (approximately 21 MLT – 03 MLT for PAG) was examined. The MPB's, included in the yearly lists, have to fulfil the following conditions:

- The IL index computed by data from the PPN-NAL IMAGE chain has a minimum smaller than -200 nT;
- In the vicinity of this minimum at time distance no more than 30 min., a peak of the X magnetic field component at PAG was registered;
- The maximal value of the peak is greater or equal to 5 nT.

In 2022, 153 midlatitude positive bays were detected, meeting the above criteria. For the investigation, we used the strongest of them, with maximal value greater than 20 nT, which are 14 (about 10% of the whole number).

From subsection "MPB parameters", the MPB beginning time, the MPB maximal value and the MPB amplitude have been used for the chosen substorm cases [Guineva et al., 2023a].

Results.

Interplanetary and geomagnetic conditions in the time of MPB under examination.

Some characteristics of the examined MPB's and the peculiarities of the interplanetary and geomagnetic conditions at the same time are summarized in Table 1. The consecutive columns of the table are as follows: case number, date, the beginning time of MPB at PAG, MPB maximal value, MPB amplitude, observed structure in the solar wind, SYM/H index minimal value, the time of SYM/H minimum, SYM/H value at the MPB beginning time, the phase of the geomagnetic storm at the MPB beginning time (if a geomagnetic storm was developed at the same time).

Table 1. *Interplanetary and geomagnetic conditions in the time of strong MPB’s.*

№	date	MPB beginning time	MPB_{max} nT	Amplitude nT	Solar wind structure	SYM/H_{min} nT	Time of SYM/H_{min}	SYM/H nT	Storm phase
1	04.02.2022	17:44	27.63	40.13	EJECTA	-71	20:58	-51	Main phase
2	10.02.2022	20:14	21.57	30.19	MC	-68	19:00	-60	Max development
3	11.02.2022	19:39	28.94	42.87	CIR	-46	00:30 (12.02)	-5	Main phase
4	05.03.2022	20:26	27.30	33.80	HSS	-60	19:41	-57	Max development
5	02.04.2022	18:14	23.50	31.29	HSS	-59	07:07	-25	Late recovery
6	14.04.2022	18:29	27.11	43.66	MC	-86	22:40	-64	Main phase
7	27.05.2022	23:21	21.74	33.49	HSS	-59	07:16 (28.05)	-40	Main phase
8	19.07.2022	19:00	31.15	39.23	EJECTA	-65	12:20	-58	Max development
9	19.07.2022	21:27	30.06	38.63	EJECTA	-65	12:20	-63	Max development
10	08.08.2022	21:59	20.53	33.00	HSS	-69	07:42	-30	Recovery phase
11	11.08.2022	18:30	23.48	32.42	HSS	-69	07:42	-36	Late recovery
12	23.10.2022	20:21	23.32	32.71	CIR	-85	16:36 (22.10)	-16	Late recovery
13	07.11.2022	19:07	24.79	52.63	SLOW	-117	17:20	-110	Max development
14	22.12.2022	19:54	20.74	27.09	SLOW	-33	17:01	-14	

As it seen from Table 1, in almost all 14 cases, structures in the solar wind were registered (5 HSS’s, 2 CIR’s, 3 Ejectas, 2 MC’s, and only 2 Slows), and geomagnetic storms developed (except in the last case). Most of the storms are between the 50 top geomagnetic storms in 2022. 2022 is at about the middle of the ascending phase of SC25, which is expected to be a weak cycle, same as SC24, Sn number didn’t exceed 100 in 2022, so the maximal Ap index for the 13 storms is 40, the maximal kp is 6+, and the minimal SYM/H value is -117 nT.

Comparison of the obtained results with results about the same substorms by SML index.

To compare the substorm results by PAG magnetic data, we used the substorm lists by Newell and Gjerloev (2011), Forsyth et al. (2015) and Ohtani and Gjerloev (2020) from the SuperMAG database. At first, the AL index has been used to identify substorm events. Nowadays, several techniques are using the SuperMAG version of the AL index (SML index) to identify substorm events. The substorm events are identified and the substorm onsets are determined by several different techniques. It should be taken into account, that all existing substorm onset identification techniques have limitations. By reason of the applied technique and its assumptions, there may be some differences in the identified substorms and in the determined onsets. The substorm lists contain the time and the location of the substorm onset, comprising the following coloumns: the date, the substorm onset time (UT), magnetic local taime (MLT), magnetic latitude (Mlat), geographic longitude (Glon), and geographic latitude (Glat). For our comparison, we constructed 3 tables, Table 2, 3 and 4, including our data and corresponding data from the Newell and Gjerloev (2011), Forsyth et al. (2015) and Ohtani and Gjerloev (2020) lists, respectively.

Table 2. *Comparison of the obtained beginnings of the examined MPB's with the results of identified substorms over Europe at the same time by Newell and Gjerloev (2011).*

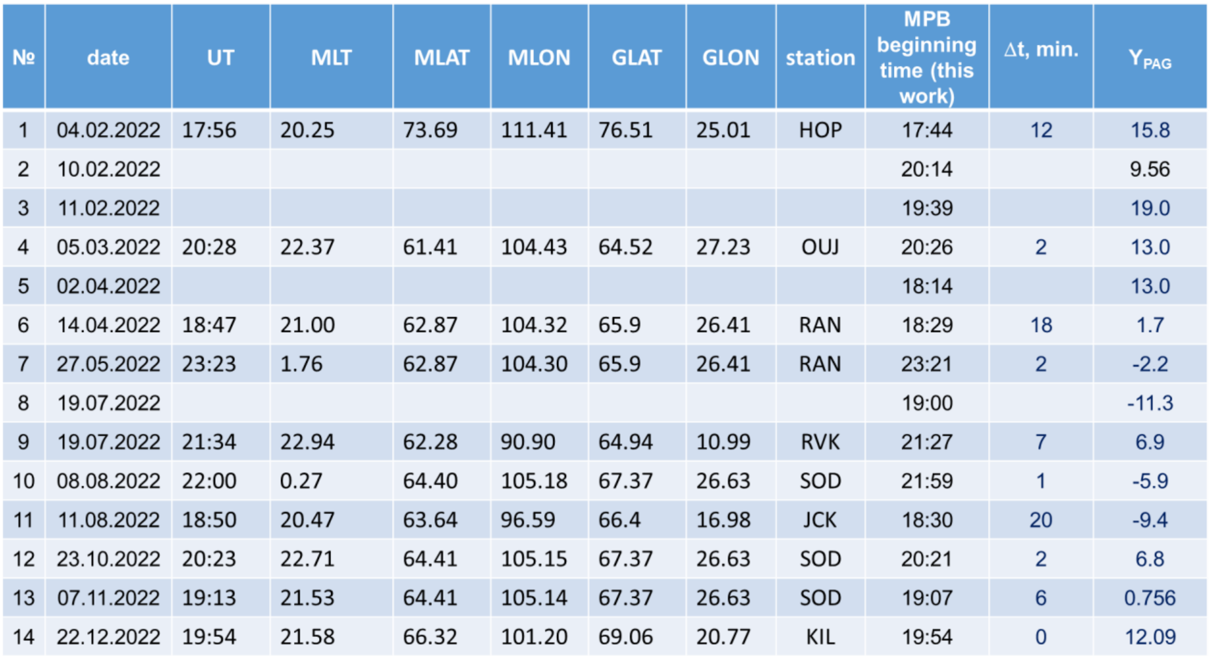

№	date	UT	MLT	MLAT	MLON	GLAT	GLON	station	MPB beginning time (this work)	Δt, min.	Y_{PAG}
1	04.02.2022	17:56	20.25	73.69	111.41	76.51	25.01	HOP	17:44	12	15.8
2	10.02.2022								20:14		9.56
3	11.02.2022								19:39		19.0
4	05.03.2022	20:28	22.37	61.41	104.43	64.52	27.23	OUJ	20:26	2	13.0
5	02.04.2022								18:14		13.0
6	14.04.2022	18:47	21.00	62.87	104.32	65.9	26.41	RAN	18:29	18	1.7
7	27.05.2022	23:23	1.76	62.87	104.30	65.9	26.41	RAN	23:21	2	-2.2
8	19.07.2022								19:00		-11.3
9	19.07.2022	21:34	22.94	62.28	90.90	64.94	10.99	RVK	21:27	7	6.9
10	08.08.2022	22:00	0.27	64.40	105.18	67.37	26.63	SOD	21:59	1	-5.9
11	11.08.2022	18:50	20.47	63.64	96.59	66.4	16.98	JCK	18:30	20	-9.4
12	23.10.2022	20:23	22.71	64.41	105.15	67.37	26.63	SOD	20:21	2	6.8
13	07.11.2022	19:13	21.53	64.41	105.14	67.37	26.63	SOD	19:07	6	0.756
14	22.12.2022	19:54	21.58	66.32	101.20	69.06	20.77	KIL	19:54	0	12.09

Table 3. *Comparison of the obtained beginnings of the examined MPB's with the results of identified substorms over Europe at the same time by Forsyth et al. (2015).*

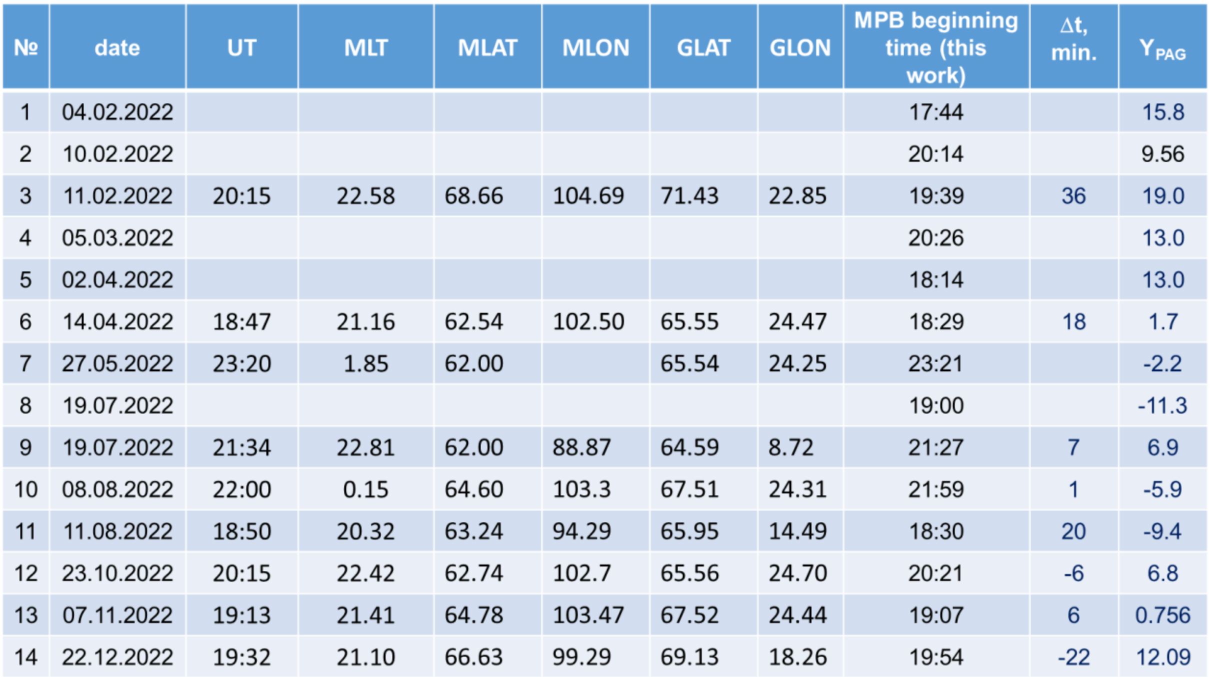

№	date	UT	MLT	MLAT	MLON	GLAT	GLON	MPB beginning time (this work)	Δt, min.	Y_{PAG}
1	04.02.2022							17:44		15.8
2	10.02.2022							20:14		9.56
3	11.02.2022	20:15	22.58	68.66	104.69	71.43	22.85	19:39	36	19.0
4	05.03.2022							20:26		13.0
5	02.04.2022							18:14		13.0
6	14.04.2022	18:47	21.16	62.54	102.50	65.55	24.47	18:29	18	1.7
7	27.05.2022	23:20	1.85	62.00		65.54	24.25	23:21		-2.2
8	19.07.2022							19:00		-11.3
9	19.07.2022	21:34	22.81	62.00	88.87	64.59	8.72	21:27	7	6.9
10	08.08.2022	22:00	0.15	64.60	103.3	67.51	24.31	21:59	1	-5.9
11	11.08.2022	18:50	20.32	63.24	94.29	65.95	14.49	18:30	20	-9.4
12	23.10.2022	20:15	22.42	62.74	102.7	65.56	24.70	20:21	-6	6.8
13	07.11.2022	19:13	21.41	64.78	103.47	67.52	24.44	19:07	6	0.756
14	22.12.2022	19:32	21.10	66.63	99.29	69.13	18.26	19:54	-22	12.09

Table 4. *Comparison of the obtained beginnings of the examined MPB's with the results of identified substorms over Europe at the same time by Ohtani and Gjerloev (2020).*

№	date	UT	MLT	MLAT	MLON	GLAT	GLON	station	MPB beginning time (this work)	Δt, min.	Y_{PAG}
12	23.10.2022	20:21	22.14	61.69	97.15	64.61	18.75	LYC	20:21	0	6.8
13	07.11.2022	19:11	21.41	66.64	103.89	69.46	23.7	MAS	19:07	4	0.756
14	22.12.2022	19:30	21.12	67.00	100.09	69.66	18.94	TRO	19:54	-24	12.09

The columns in Table 2, 3 and 4 are as follows: case number after Table 1, event date, substorm onset time by the respective list, magnetic and geographic coordinates of the onset (MLT, MLAT, MLON, GLAT, GLON), station name (in case, if the onset geographic coordinates correspond to a station location), the beginning time of the midlatitude positive bay (MPB) at PAG, the difference between the substorm onset time and the MPB beginning time (Δt), and the value of Y at PAG at the moment of the MPB maximum (Y_{PAG}).

From Tables 2, 3 and 4 it is seen, that almost all substorm events, identified by local (European) data, have been identified by techniques, using SML index. The time difference Δt in most cases is small, but there are also cases when Δt is much greater than expected. The MPB beginning at PAG doesn’t coincide with the substorm onset, unless the substorm meridian coincide with the PAG location. In all other cases it should be nearly after the substorm onset. That means, that Δt in the tables above is expected to be small and negative. In our previous studies [Guineva et al., 2023a] we have supposed, that the slightly earlier MPB beginning at PAG than the substorm onset time determined based on SML index may be due to the difficulty to estimate whether the smaller disturbances before the sharp decrease of X are the result of localized or global events in the magnetosphere, especially under disturbed conditions or when the substorms are not isolated. The obtained greater differences between the determined substorm onsets and the MPB beginning at PAG in some cases are maybe result of the assumptions made and the conditions set in the processing tools of the different techniques.

A case with great difference between the substorm onset determined by SML, and the MPB beginning at PAG.

To clarify the reasons for greater differences Δt in Tables 2, 3 and 4, we examined in detail these cases. In Figure 1 peculiarities of such a case are given, namely case number 6, the substorm on 14.04.2022 with onset at 18:47 UT by Newell and Gjerloev (2011) and Forsyth et al. (2015). This is an event in the presence of magnetic cloud, during the main phase of a geomagnetic storm. During this substorm a strong midlatitude positive bay was registered at Panagjurishte (PAG), with maximal value 27.11 nT and amplitude 43.66 nT. In Figure 1a the SML index from 17 to 21 UT on 14.04.2022 is shown. The red vertical line indicates the time of the substorm onset determined by SML, and the green one – the time of the MPB beginning at PAG, which is 18 minutes earlier than the onset. In Figure 1b the magnetic field components at the Ranua station (RAN) are presented, which coordinates coincide with the substorm onset location given in the substorm lists. The red and green vertical lines match the

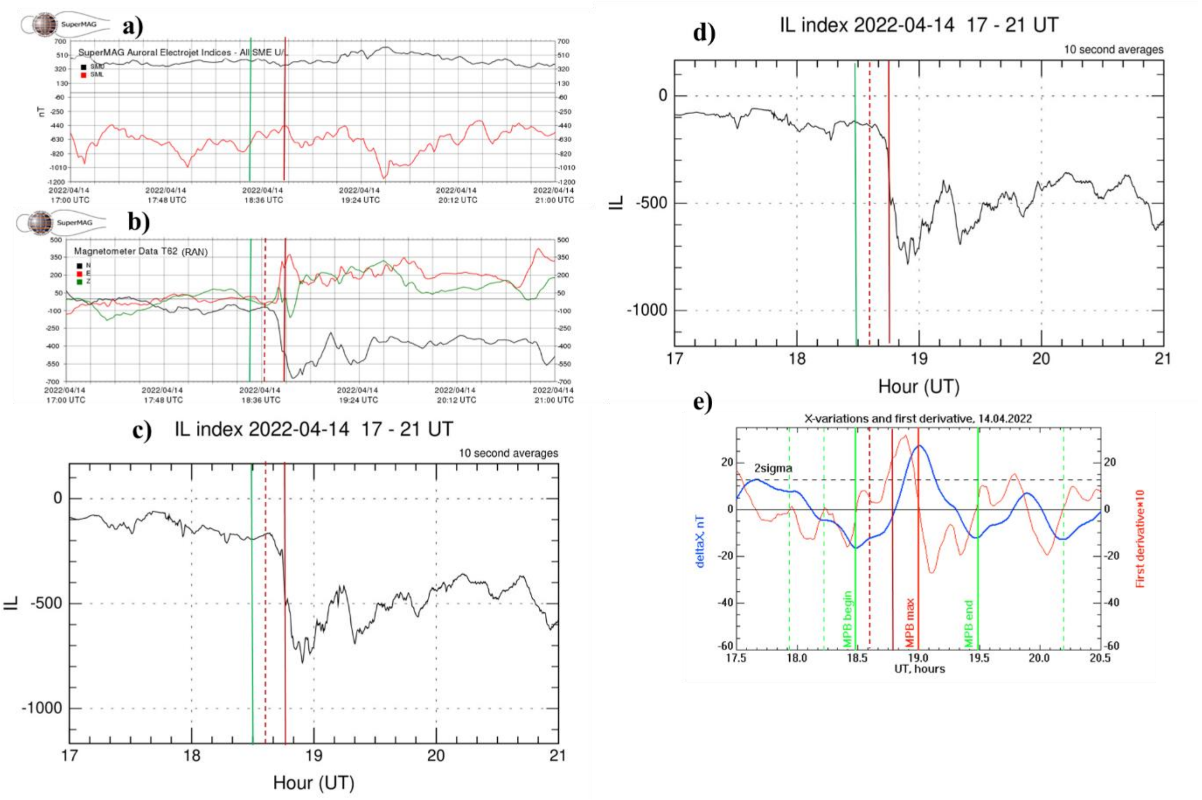

Figure 1. *An event for which greater difference between the determined by SML data substorm onset time and the estimated MPB beginning time at PAG (□t), the substorm on 14.04.2022: a) SML index from 17 to 21 UT; b) magnetic field data from the station Ranua (RAN) from the same time interval; c) IL index based on all IMAGE stations; d) IL index based on PPN-NAL chain stations; e) MPB registered at Panagjurishte (PAG).*

same moments as in Figure 1a, and the red dotted line – the onset time based on RAN X component, estimated by eye inspection (about 18:37 UT). It is seen that in this case, there is also difference between the onset times determined by SML index and the magnetic variations at the onset location. Figure 1c and 1d show the IL index by all IMAGE stations and by the PPN-NAL stations chain, respectively. The vertical lines indicate the same times as in Figure 1b. It can be seen some difference between Figure 1c and 1d only near the time of the substorm onset. There is a plateau of small disturbances from about 18:20 to 18:40 UT and maybe the disturbances after the green line, pointing the MPB beginning at PAG, belong to global events in the magnetosphere. As Ranua is part of the PPN-NAL chain, this meridian can be considered roughly as the substorm meridian. Panagjurishte is at about 5° distance by GMLON from Ranua, therefore the MPB beginning at PAG is very close to the onset time. It is known, that the MPB's are less sensitive to interference from small details in the electrojet and are a good indicator of the substorm onset [McPherron, 1972]. We assume that in this case, the substorm onset was between 18:20 and 18:29 UT. The exact onset time could be determined by examination of the MPB's of the European stations in the region.

Conclusions.

The strong midlatitude bays (MPB) (Xmax>20 nT) registered at Panagujrishte (PAG) in 2022 were related to substorms, developed during disturbed interplanetary and geomagnetic conditions. The obtained MPB beginning times are close to the substorm onsets determined from the SML index except a few cases.

The obtained small differences may be due to some distance of PAG station from the substorm meridian, as well as to the complicated conditions, when some smaller magnetic perturbations just before the sharp decrease of X are related to the beginning of the global magnetospheric disturbances. We presume, that the substorm onsets could be more easily and accurately determined by the midlatitude positive bays data from a global or regional set of midlatitude magnetic stations.

The obtained greater differences between the determined substorm onsets and the MPB beginning at PAG in some cases are maybe result of the assumptions made and the conditions set in the processing tools of the different techniques. The contributions of stations far from the substorm meridian, in such cases may lead to significant discrepancies between the substorm onset, determined by global (SML) and regional (IL, European MPB index) indices, so all results have to be verified for every concrete case.

Acknowledgements: We acknowledge the substorm timing list identified by the SOPHIE technique (Forsyth et al., 2015), the substorm timing list identified by the Newell and Gjerloev technique (Newell and Gjerloev, 2011), the substorm timing list identified by the Ohtani and Gjerloev technique (Ohtani and Gjerloev, 2020), the SMU and SML indices (Newell and Gjerloev, 2011); and the SuperMAG collaboration (Gjerloev et al. 2012). The authors are grateful to the creators of the databases IMAGE (http://space.fmi.fi/image/), OMNI (https://cdaweb.gsfc.nasa.gov/) and the solar wind large-scale phenomena catalog (http://www.iki.rssi.ru/omni/) for the opportunity to use them in this work.

References

Forsyth, C., Rae, I. J., Coxon, J. C., Freeman, M. P., Jackman, C. M., Gjerloev, J., Fazakerley A. N. (2015). A New Technique for Determining Substorm Onsets and Phases from Indices of the Electrojet (SOPHIE), J. Geophys. Res. Space Physics, Vol. 120, DOI:10.1002/2015JA021343.

Gjerloev, J. W. (2012), The SuperMAG data processing technique, J. Geophys. Res., Vol. 117, A09213, DOI:10.1029/2012JA017683.

Guineva V.H., R. Werner, A.M. Atanassov, R.Ts. Bojilova, L.N. Raykova, D.T. Valev, (2023a). Determination of the parameters of midlatitude positive bays caused by magnetospheric substorms, Proceedings of the Fifteenth Workshop "Solar Influences on the Magnetosphere, Ionosphere and Atmosphere", Primorsko, Bulgaria, 05 - 09 June 2023, pp.56-63, DOI: 10.31401/ws.2023.proc, https://www.spaceclimate.bas.bg/ws-sozopol/pdf/Proceedings2023.pdf

Guineva V., R. Werner, I. Despirak, N. Klejmenova, A. Lubchich, P. Setsko, A. Atanassov, R. Bojilova, L. Raykova, D. Valev, (2023b). Results from the bulgarian-russian project on investigation of the geomagnetic disturbances propagation to mid-latitudes and their interplanetary drivers identification for the development of mid-latitude space weather forecast, Proceedings of the Nineteenth International Scientific conference SES2023, 24-26.10.2023, Sofia, Bulgaria, pp.47-56, http://space.bas.bg/SES/archive/SES%202023_DOKLADI/1_Space%20Physics/2_Guineva.pdf

Guineva V., R. Werner, I. Despirak, N. Klejmenova, A. Lubchich, P. Setsko, A. Atanassov, R. Bojilova, L. Raykova, D. Valev, (2023c). Basic results from the project "Investigation of the geomagnetic disturbances propagation to mid-latitudes and their interplanetary drivers identification for the development of mid-latitude space weather forecast", Proc. 46th Annual seminar "Physics of Auroral Phenomena", 13-17 march 2023, Apatity, Russia, pp.23-29, http://pgia.ru/seminar/archive/

Kepko L., R.L. McPherron, O. Amm, S. Apatenkov, W. Baumjohann, J. Birn, M. Lester, R. Nakamura, T.I. Pulkkinen, V. Sergeev, (2014). Substorm current wedge revisited, Space Sci. Rev., Vol.190, pp. 1–46, DOI: 10.1007/s11214-014-0124-9.

Kisabeth, J.L., G. Rostoker, (1974). The expansive phase of magnetospheric substorms: 1. Development of the auroral electrojets and auroral arcs configuration during substorm, J. Geophys. Res., Vol.79, No7, pp.972–984, DOI: 10.1029/JA079i007p00972.

McPherron, R.L., (1972). Substor related changes in the geomagnetic tail: The growth phase, Planet. Space Sci., Vol. 20, No. 9, pp. 1521-1539, DOI: 10.1016/0032-0633(72)90054-2.

McPherron, R. L., Russell, C. T., Aubry, M. (1973a). Satellite studies of magnetospheric substorms on August 15, 1968, 9: phenomenological model for substorms, J. Geophys. Res., Vol. 78, No. 16, pp. 3131–3149, DOI: 10.1029/JA078i016p03131.

McPherron R.L., C.T. Russell, M.G. Kivelson, P.J. Coleman, Jr., (1973b). Substorms in space: The correlation between ground and satellite observations of the magnetic field, Radio Sci., Vol.8. No.11, pp. 1059-1076, DOI: 10.1029/RS008i011p01059.

McPherron, R.L., Chu, X., (2017). The midlatitude positive bay and the MPB index of substorm activity, Space Sci. Rev., Vol. 206, pp. 91-122, DOI: 10.1007/s11214-016-0316-6.

Meng, C.-I., Akasofu, S.-I., (1969). A study of polar magnetic substorms. 2. 3-dimensional current system, J. Geophys. Res., Vol. 74, pp. 4035–4053, DOI: 10.1029/JA074i016p04035.

Newell, P. T., Gjerloev, J. W., (2011). Substorm and magnetosphere characteristic scales inferred from the SuperMAG auroral electrojet indices, J. Geophys. Res., Vol. 116, A12232, DOI:10.1029/2011JA016936.

Ohtani, S., Gjerloev, J.W., (2020). Is the substorm current wedge an ensemble of wedgelets?: Revisit to midlatitude positive bays, Journal of Geophysical Research: Space Physics, Vol. 125, No. 9, p. e2020JA027902, DOI:10.1029/2020JA027902.

Angular Dependencies of the Ionospheric Scintillation Parameters Based on Observations of the Cosmic Radio Sources in the Decameter Radio Wave Range

Lytvynenko O.A., Panishko S.K.

Institute of Radio Astronomy of NASU, spanishko@ukr.net

Abstract

Passing through the Earth's ionosphere the radio wave from cosmic source crosses the layer with electron concentration irregularities which cause random phase fluctuations of the radio wave that leads to intensity fluctuations. Due to movement of the irregularities along the line of sight the intensity fluctuations at the receiving point, are observed as the temporary fluctuations of radio signal known as ionospheric scintillations. This effect is most pronounced in decameter radio wave range. Its intensity is determined by the heterogeneous structure of ionosphere, and, among other things, depends on the geometry of the radio signal propagation which is associated with the manifestations of the angular dependencies of the ionospheric scintillation parameters. Such dependencies reflect the heterogeneous structure of ionosphere and can serve as a research tool. According to long-term observations of the power cosmic radio sources in the decameter radio wave range the estimations of the ionospheric scintillation parameters – index, period and spectral index, were obtained. The dependencies of these values on the zenith angle and on the angle between source direction and geomagnetic field line were analyzed. It is shown, that the scintillation index and period are related to each other in inverse proportion and show the dependencies on angle between source direction and geomagnetic field line. At the same time, the spectral index demonstrates the well expressed dependence on the radio source zenith angle.

Key words: Cosmic radio sources; Ionospheric scintillations; Angular dependencies.

Introduction

Passing through the Earth`s ionosphere, the radio wave from cosmic source intersects a layer with irregularities of electron concentration which cause random phase fluctuations, resulting in intensity fluctuations. Due to the movement of irregularities along the line of sight, intensity fluctuations at the receiving point are observed as temporary fluctuations of the radio signal known as *ionospheric scintillation* [Aarons, 1982]. This effect depends on the wavelength and is most pronounced in the decameter radio wave range.

The intensity of the ionospheric scintillation is determined by the inhomogeneous structure of the ionosphere and, among other things, depends on the geometry of radio signal propagation, which is associated with the manifestations of the angular dependences of the ionospheric scintillation parameters [Vasylyev et al., 2022]. Such dependencies reflect the inhomogeneous structure of the ionosphere and can serve as a tool for its study.

The main geometric factors influencing the scintillation intensity are the dependence on the zenith angle θ due to the changes in thickness of the scattering layer and dependence on the angle β between direction to the source (the line of sight) and the geomagnetic field line due to elongation of irregularities along field lines. Figure 1 shows the geometry of signal propagation from a radio source to the observer with taking into account the passage through ionospheric layer with irregularities of electron concentration; direction of the geomagnetic vector is also shown. Symbols used in the Figure 1: D – magnetic declination; I – magnetic inclination; **H** – geomagnetic vector; $\delta_m = I - (90^o - \Phi)$ – angle between the vector **H** and the equatorial plane; Φ – latitude; S – line of sight of the source; θ – zenith angle of the source; δ – angle between the line of sight and the equatorial plane; β – angle between the vector **H** and the line of sight.

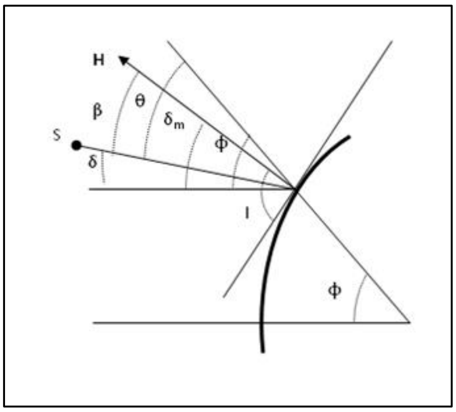

Figure 1. *Geometry of the radio wave propagation from a source to the observer crossing of ionospheric layer*

The purpose of the work is to study the angular dependencies of the ionospheric scintillation parameters based on long-term observations of the cosmic radio sources in the decameter radio wave range.

Observations and processing method

Observations, the analysis of which is presented in this studying, were obtained on the radio telescope (RT) URAN-4 on the frequencies 20 and 25 MHz. From 1987 to present the observations of the power cosmic radio sources 3C 144, 3C 274, 3C 405, 3C 461 were carried out on the RT URAN-4 in monitoring regime. All observed radio sources scintillate on irregularities of the electron concentration of ionosphere. The measurements consist in the fact that during the day the several passages of each radio source through RT direction pattern are recorded for discrete values of the hour angle near culmination moment [Derevyagin et al., 2005]. Separate record of the radio source is used for processing data. To decrease the influence of the RT direction pattern the fluctuating row was separated in the central part of record. This row was used to determine the scintillation parameters [Panishko and Lytvynenko, 2023].

The scintillation index SI was estimated on the fluctuating row as

$$\mathrm{SI} = \sqrt{\langle (\mathrm{I}(\mathrm{t}) - \langle \mathrm{I} \rangle)^2 \rangle / \langle \mathrm{I} \rangle^2}\ . \qquad (1)$$

Scintillation period ST (in seconds) was calculated as a value of the time shift when the auto correlation function of the fluctuating row first reaches zero. Spectral index SP was defined as the slope of the spectrum which was obtained by the Fourier transformation of the fluctuating row. The scheme for obtaining scintillation data is shown in the Figure 2.

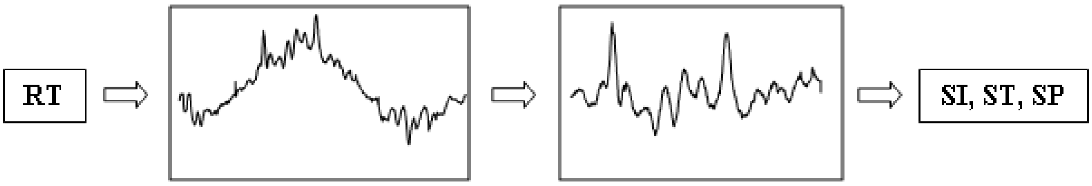

Figure 2. *The scheme for obtaining the scintillation data*

Given that for RT URAN-4 is D = 2°, I = 63.73°, δ_m = 20.127°, the angles β_0 were calculated by coordinate transformation for culmination moment of each radio source on the ionospheric latitudes at the observation point. Data is presented in the Table 1. The quantities of the zenith angles for culmination moment and type of observed radio sources are also placed here (SNR – supernova remnant; RG – radio galaxy).

Table 1. *Angular characteristics of the radio sources*

Source	Source type	θ_0°	β_0°
3C 144	SNR	24.4	1.84
3C 274	RG	34.0	-7.36
3C 405	RG	05.7	20.54
3C 461	SNR	-12.4	38.52

The Figure 3 shows how the zenith angle of the radio sources changes during observations at different hour angles. It is clear from the Figure 3 that radio sources 3C 405 and 3C 461 are observed near zenith, while 3C 144 and 3C 274 are lower altitudes.

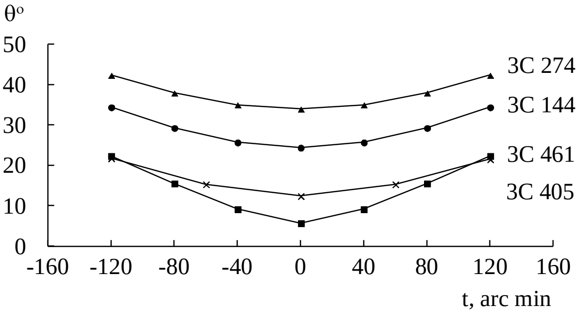

Figure 3. *Change of zenith angle on the dependence of the hour angle of radio source during observations*

Results and their analysis

During 1987–1990 analog observations were carried out on RT URAN-4. These measurements were used for estimations of the scintillation index and periods. Insufficient data was received on the 20 MHz due to the radio interference. Average values were calculated for all estimations of each radio sources on the frequency 25 MHz, that showed there was the inversely proportional relationship between the index and period (Figure 4, on the left) [Lytvynenko and Panishko, 2000]. Further digital measurements which carried out during 1998–2000 confirmed this relationship at two frequencies (Figure 4, on the right).

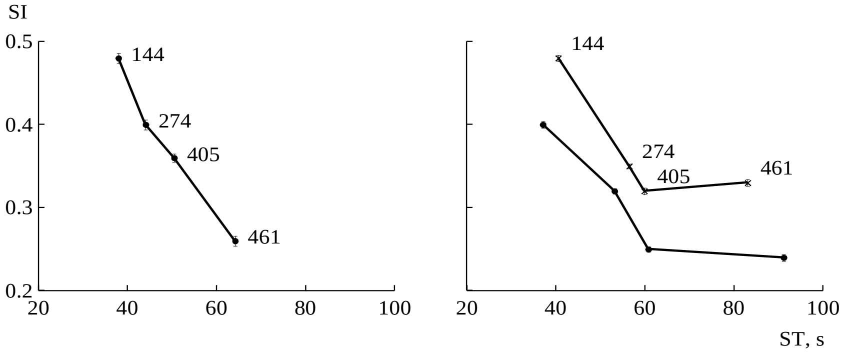

Figure 4. *The dependence index–period for average values of each radio source. On the left – data from 1987-1990, 25 MHz; on the right – data from 1998-2007, 20 (crests) and 25 (dots) MHz*

As can be seen from Table 2, the values of ionospheric scintillation parameters on the two frequencies are significantly correlated with each other, so the data on the 25 MHz is used in further analysis.

Table 2. *Correlation coefficients of the scintillation parameters on the 20 and 25 MHz*

NS	R(SI)	R(ST)	R(SP)
3C 144	0.94	0.93	0.90
3C 274	0.90	0.84	0.52
3C 405	0.87	0.46	0.54
3C 461	0.90	0.64	0.73

The dependence considered above allows us to assume the presence of geometric factor due to influence of the geomagnetic field. The dependence of the average periods for each radio source on the angle β_0 is shown in the Figure 5. From graph we can approximately estimate the coefficient of elongation of irregularities along the geomagnetic field lines in relation to the transverse size as 1:2.6.

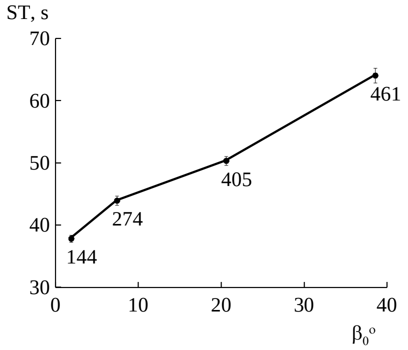

Figure 5. *The dependence of the scintillation period on the angle between the radio source line of sight and the geomagnetic vector on the ionospheric altitudes*

Since 1998, digital registration of the observation data has been used and estimations of spectral index have been added to the index and period already measured. The dependence of the scintillation parameters on the radio source zenith angle which was calculated for culmination moment is shown in the Figure 6.

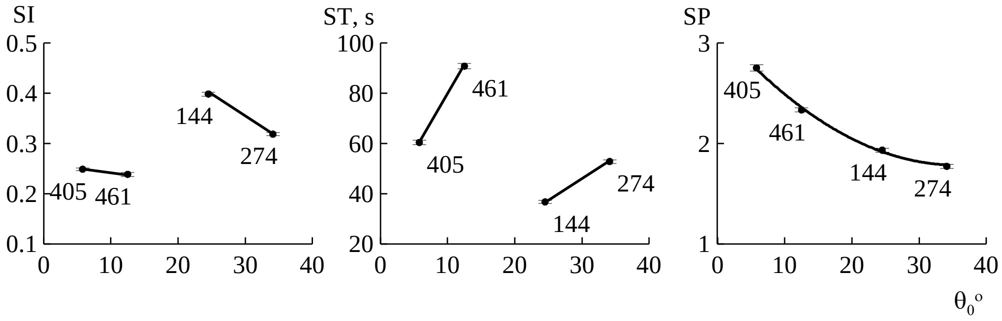

Figure 6. *The dependence of the average index, period and spectral index on the zenith angle*

The dependence of scintillation parameters on the angle between line of sight and geomagnetic field line is shown in the Figure 7.

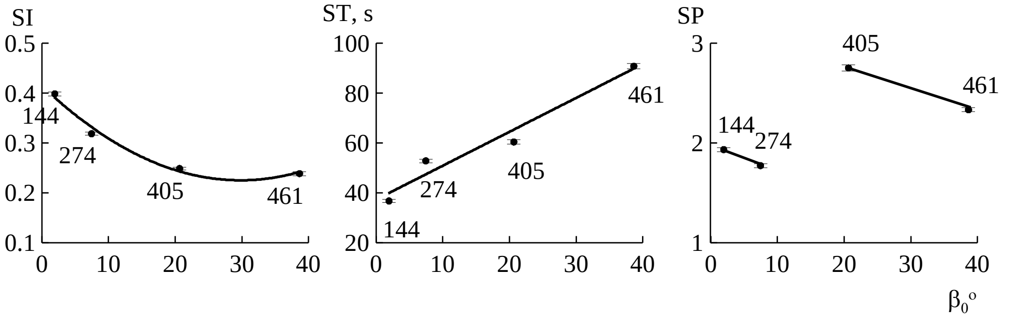

Figure 7. *The dependence of the index, period and spectral index on the angle between line of sight and geomagnetic field line*

As mentioned above (Figure 3), the graphs show that the observed radio sources can be divided into two groups: «high» and «low» with similar characteristics within groups. Further dependencies for each scintillation parameters on the angles θ and β are considered in more detail.

There is a dependence on the angle β for the scintillation index, which is emphasized by the second-degree polynomial. Dependence on the angle θ is observed within groups of the radio sources. In general, the index decreases with both an increasing in angle β and an increasing in angle θ. Due to the inversely proportional relationship between the index and the period, the period increases with angle β almost linearly and increases with increasing angle θ within groups. The spectral index has a clearly expressed dependence on the angle θ, which is emphasized by the second-degree polynomial, and decreases with its growth, within groups – decreases with the growth of the angle β.

Thus, the obtained results allow us to state that the nature of the angular dependencies of the ionospheric scintillation parameters is influenced by both the change in the thickness of the scattering layer and the elongation along the lines of force of the geomagnetic field of the irregularities responsible for the occurrence of scintillations.

Conclusions

Based on the long-term observations of the cosmic radio sources 3C 144, 3C 274, 3C 405 and 3C 461 in decameter range wave, estimations of the scintillation parameters (index SI, period ST and spectral index SP) were obtained. Dependences of SI, ST and SP on the zenith angle θ and on the angle β between line of sight and geomagnetic field line were analyzed. It was found:

1. By the nature of angular dependencies of the ionospheric scintillation parameters the radio sources can be divided into two groups: with smaller zenith angles (3C 405, 3C 461) and larger zenith angles (3C 144, 3C 274).
2. The index and period of the ionospheric scintillations are inversely related and show dependence on the angle β, with the index decreasing and the period increasing with increasing angle β. The obtained data made it possible to estimate the coefficient of elongation along the lines of force of geomagnetic field of the irregularities causing scintillations in relation to the transverse size as 1:2.6. The dependence on the angle θ is manifested within groups: the index decreases and the period increases with increasing angle θ.
3. The spectral index has a clear dependence on the angle θ, decreasing with its growth. Within groups spectral index decreases with increasing angle β.
4. Analysis of these results allows us to conclude that the angular dependencies of the ionospheric scintillation parameters contain a contribution from both angle θ and angle β, which must be taken into account when interpreting the observation data.

References

Aarons, J. (1982). Global Morphology of Ionospheric Scintillations, Proc. IEEE, Vol. 70, No 4, pp. 360-378.

Derevyagin, V.G., Isaeva, E.A., Kravetz, R.O., Litvinenko O.A., Panishko, S.K. (2005). Observations of power cosmic radio sources on the radio telescope URAN-4 during 1998-2004, Astronom. and Astrophys. Trans., Vol. 24, No 5, pp. 421-424, http://dx.doi.org/10.1080/10556790600631652.

Lytvynenko, O.A., Panishko, S.K. (2000). Studying of the scintillations of the cosmic sources on the ionospheric irregularities in the decameter radio wave range, Geomagnetizm i aeronomia, Vol. 40, No 4, pp. 116-117. (in Russia).

Panishko, S. K., Lytvynenko, O. A. (2023). Short period variations of the parameters of ionospheric scintillations on the long-time observations of the cosmic radio sources at the decameter radio waves, Proc. of Fifteenth Workshop, Primorsko, Bulgaria, June 5-9, 82-88, DOI: 10.31401/WS.2023.proc.

Vasylyev, D., Béniguel, Y., Volker, W., Kriegel, M., Berdermann J. (2022). Modeling of ionospheric scintillation, J. Space Weather Space Clim., Vol. 12, 22, pp. 1-19. https://doi.org/10.1051/swsc/2022016.

St. Patrick's Day 2015 Geomagnetic Storm: Sources of Perturbations

Stefan C., Dobrica V.

"Sabba S. Stefanescu" Institute of Geodynamics of the Romanian Academy,
19-21 Jean-Louis Calderon St., 020032 Bucharest, Romania; cristiana_stefan@geodin.ro

Abstract

The St. Patrick's Day 2015 geomagnetic storm, the strongest one of the solar cycle 24, was analyzed in order to highlight the possible sources accountable for the perturbations observed in recorded data during the storm. SuperMAG database was used to obtain ground data recordings in an equally distributed grid at the northern hemisphere scale that then were analyzed by means of the empirical orthogonal function method (EOF). The connection between the time series of the EOF modes and various geomagnetic indices (Dst, AE) that describe current systems in the magnetosphere and ionosphere, sources of perturbations, was achieved using the wavelet coherence analysis (WTC).

Keywords: Sun-Earth interaction; St. Patrick's Day 2015 geomagnetic storm; sources of perturbations

Introduction

The strongest geomagnetic storm of solar cycle 24 that occurred on 17 March 2015 is associated to a partial halo coronal mass ejection (CME) related to a C9.1 flare. It was first seen in LASCO/C2 images at 02:00 UT on March 15 and wasn't expected to reach Earth. The unexpected arrival was, as proposed by Kataoka et al. (2015), due a combination of (1) a fast CME followed by a high-speed stream from a nearby coronal hole and (2) a preceding slow and high-density CIR that was piled up ahead of the CME just before the arrival at the Earth enhancing its magnetic field and density. This "pileup accident" as named by Kataoka et al. (2015) generated a major magnetic storm (Kp=8) with a peak in the Dst index of -234 nT reached at 23:00 UT. Carter et al. (2016) investigated the impact of this storm in terms of geomagnetically induced currents (GICs), produced by induced geoelectric fields that are caused by magnetic field fluctuations, using magnetometer data from around the world. Dobrica et al. (2016) and Demetrescu et al. (2018) calculated the induced geoelectric field using data recorded at European geomagnetic observatories.

In order to identify the sources responsible for the perturbations observed in ground data during the development of the St. Patrick's Day 2015 geomagnetic storm we applied two widely used methods in meteorology and oceanography, namely the EOF/PCA (von Storch and Navarra, 1995; Hannachi, 2004) and the wavelet coherence (Grinsted et al., 2004). According to Bjornsson and Venegas (1997) the EOF method facilitates the determination of the spatial distribution of the variability modes (EOF) of a given field, their associated temporal variations (PC) and their importance in terms of variance. The wavelet coherence analysis (Grinsted et al., 2004) investigates relationships in time-frequency space between two time series and shows locally phase locked behavior. In geomagnetism the EOF/PCA was used by Pais et al. (2015), Domingos et al. (2019) and Stefan et al. (2019-2020) on geomagnetic field models data to show various characteristics of the geomagnetic field. Recently, Morozova and Rebbah (2023) used the PCA method to remove the Sq variation from the geomagnetic field data. The wavelet coherence (WTC) analysis was used by Giri et al. (2024) to show the phase relation between the plasma beta, Alfven Mach number, and magnetosonic Mach number with SYM-H index in case of four geomagnetic storms from solar cycles 23, 24 and 25.

Data and method

The SuperMAG database was used to acquire 1 minute data in an even spatial grid at the northern hemisphere scale. The data is available at https://supermag.jhuapl.edu/. We choose a six days interval such so the storm to be in the middle of the analyzed interval and also have information about the geomagnetic conditions prior of the storm as well on the end of the recovery phase. The EOF/PCA method was used to decompose the geomagnetic field data recorded during the 17 March 2015 geomagnetic storm into variation modes in order to highlight the possible sources of the perturbations observed in ground data. The geomagnetic indices Dst (SYM-H, ASY-H) and AE (AO, AU, AL), that describe current systems from the magnetosphere and ionosphere, sources of perturbations, were used. The data for both indices is available at http://wdc.kugi.kyoto-u.ac.jp/aeasy/index.html.

In order to show the relationship between various geomagnetic indices, which are proxies for different current systems from the magnetosphere and ionosphere, and the temporal variations associated to the EOF modes we used the wavelet coherence analysis (WTC) (Grinsted et al., 2004).

Results and discussion

The distribution, at the northern hemisphere scale, of the north geomagnetic field component (X) at the minimum of the Dst (Figure 1) shows a depression of the field of about 600 nT in the most affected area, namely the southern part of the Scandinavian Peninsula. Also, an about 400 nT decrease in the field took place in the north-west of Russia.

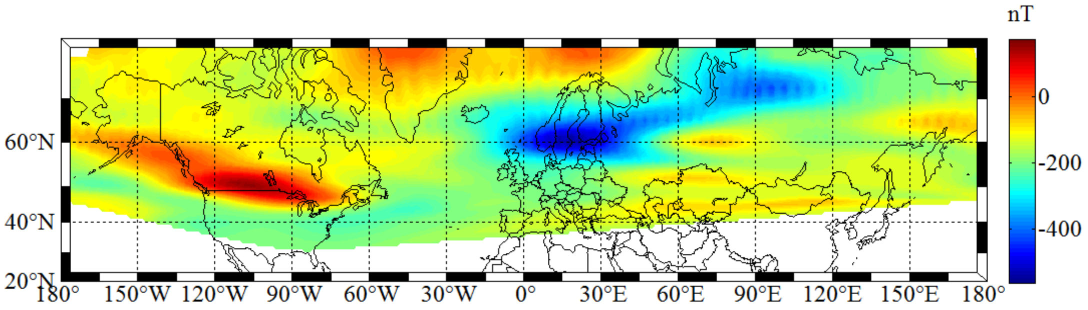

Figure 1. *Geographical distribution of the north geomagnetic field component (X) at the minimum of the Dst*

The geographical distribution of the first EOF mode (~68% variance) (Figure 2, left) reveals that the most affected areas were the Scandinavian Peninsula, the northern part of the North Atlantic, Greenland, the north-east and central Canada, North Dakota and Montana from the US. Lower intensity perturbations affected Alaska, north-west and west of the Canadian territory and Russia. The graphical representation of the time series of the first mode (PC1) along with the SYM-H index (Figure 2, upper right) reveals that there is a very good correlation (correlation coefficient -0.97) between the two of them. Also, the wavelet coherence analysis (Figure 2, bottom right) shows that the two times series are phase locked even before the beginning of the storm, marked on the figure with the purple rectangle. Based on this information we can state that almost 68% of the observed perturbations in ground data is due to the ring current intensification that takes place during the storm.

The second EOF mode (Figure 3, left) is responsible for 13% of the disturbed signal in recorded data and can be associated with the intensification of the auroral electrojet represented by the AU index. The wavelet coherence analysis (Figure 3, bottom right) reveals that before the commencement of the storm, in the time interval 30 minutes – 2 hours, there is a link between AU index and the time series of the second EOF mode (PC2). In the time interval of the duration of the storm (purple rectangle on the figure) there is a clear coherence between the analyzed time series.

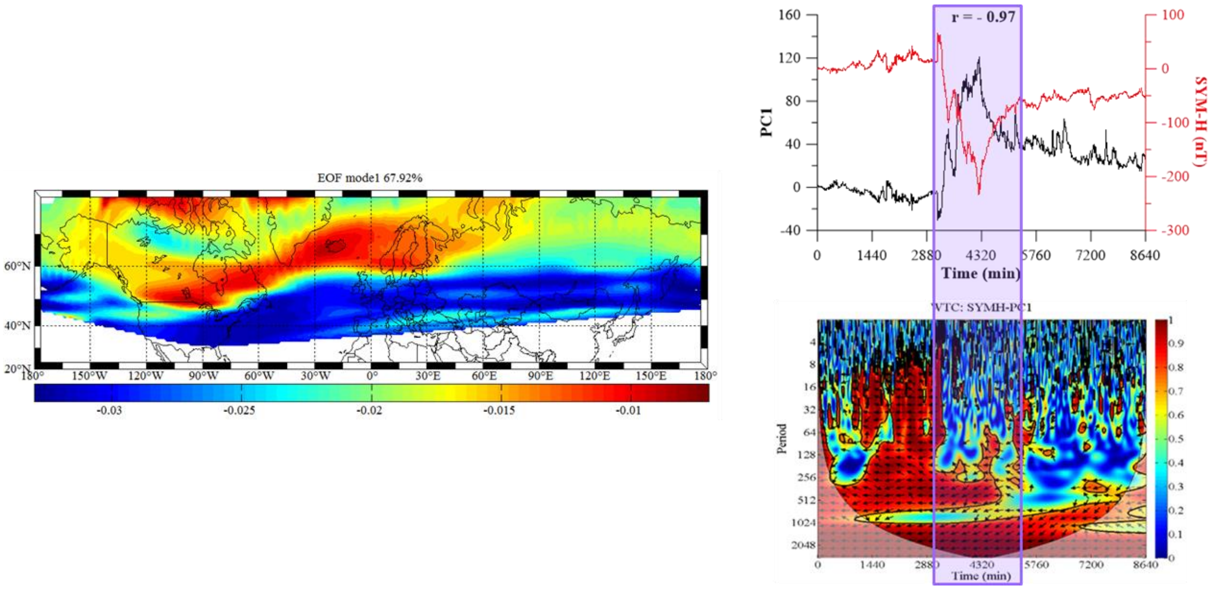

Figure 2*. Geographical distribution of the first EOF mode (left) and the associated PC1 series (black line) along with the geomagnetic index SYM-H (red line), respectively the coherence between PC1-SYM-H (bottom). The period of the storm is marked by the purple rectangle*

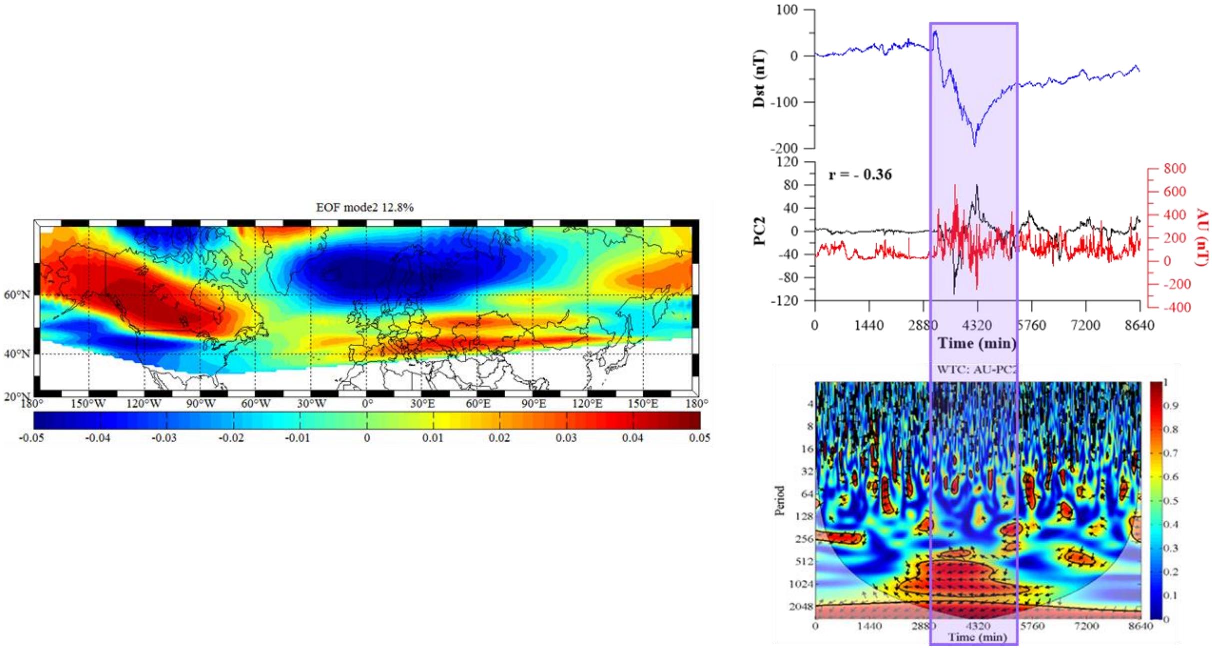

Figure 3. *Geographical distribution of the second EOF mode (left) and the associated PC2 series (black line) along with the geomagnetic indices Dst (blue line) and AU (red line), respectively the coherence between PC2-AU (bottom). The period of the storm is marked by the purple rectangle*

In Figure 4 (left) is represented the third mode that accounts for about 9% of the overall perturbation; it can be associated with the AO. The WTC shows that there is mostly an in-phase relationship (arrows pointing right) between the time series of mode 3 (PC3) and the AO index (Figure 4, bottom right).

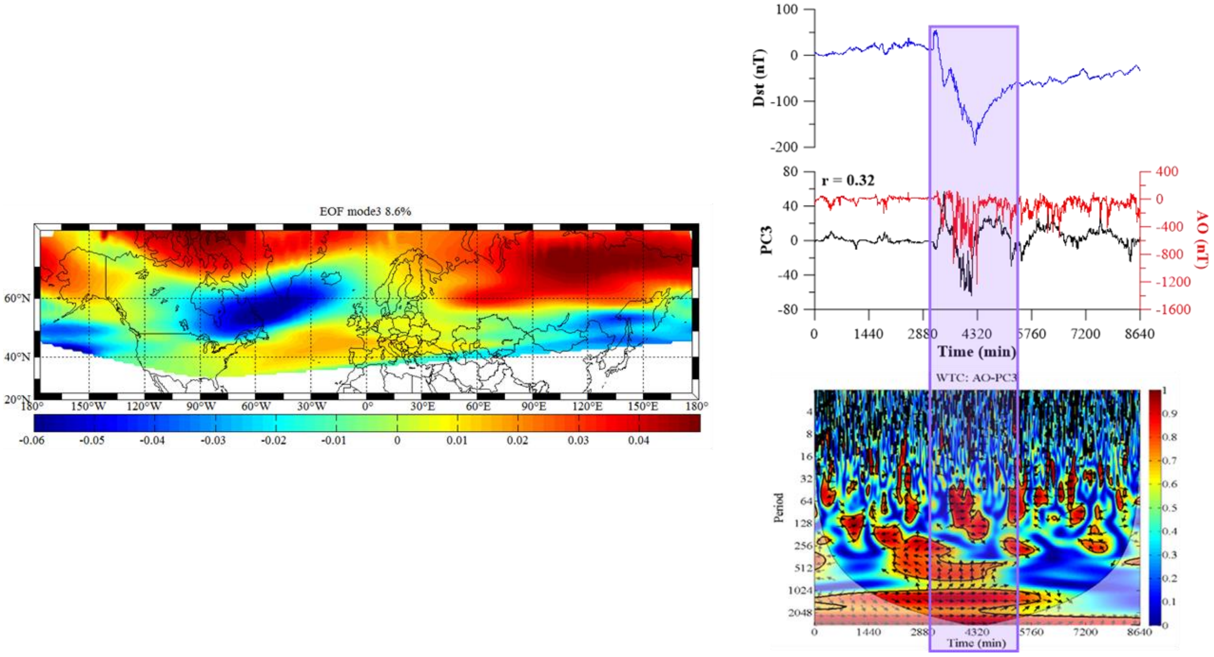

Figure 4. *Geographical distribution of the third EOF mode (left) and the associated PC3 series (black line) along with the geomagnetic indices Dst (blue line) and AO (red line), respectively the coherence between PC3-AO (bottom). The period of the storm is marked by the purple rectangle*

Conclusions

Applying two widely used methods in meteorology and oceanography and relatively new introduced in geomagnetism, namely EOF/PCA and wavelet coherence we were able to identify the sources accountable for the perturbations observed in geomagnetic data during the St. Patrick's Day 2015 storm. We obtained that the main source for this perturbations is given by the intensification of the ring current that takes place during the storm.

Acknowledgements

The paper is a contribution to the Project 3/2023 of the Institute of Geodynamics of the Romanian Academy.

Crosswavelet and wavelet coherence software were provided by A. Grinsted.

References

Bjornsson, H., Venegas, S.A. (1997), A manual for EOF and SVD analyses of climate data, Tech. Rep. No. 97-1, Department of Atmospheric and Oceanic Sciences and Centre for Climate and Global Change Research, McGill University.

Carter, B. A., Yizengaw, E., Pradipta, R., Weygand, J. M., Piersanti, Pulkkinen, M., A., Moldwin, M. B., Norman, R., Zhang, K. (2016), Geomagnetically induced currents around the world during the 17 March 2015 storm, J. Geophys. Res. Space Physics, 121, 10,496–10,507, doi:10.1002/2016JA023344.

Demetrescu, C., Dobrica V., Greculeasa, R., Stefan, C. (2018). The induced surface electric response in Europe to 2015 St. Patrick's Day geomagnetic storm, J. Atmos. and Sol. Terr. Phys., 180,106-115.

Dobrica, V., Demetrescu, C., Stefan, C., Greculeasa, R. (2016). Geomagnetically Induced Currents, a space weather hazard. Case study – Europe under intense geomagnetic storms of the solar cycle 23. Sun Geosph. 11, 111–117.

Domingos, J., Pais, M.A., Jault, D., Mandea, M. (2019). Temporal resolution of internal magnetic field modes from satellite data, Earth Planets Space 71, 2. https://doi.org/10.1186/s40623-018-0983-5.

Giri, A., Adhikari, B., Baral, R., Idosa Uga, C., Calabia, A. (2024). Wavelet Coherence Analysis of Plasma Beta, Alfven Mach Number, and Magnetosonic Mach Number during Different Geomagnetic Storms, The Scientific World Journal, 2024, 1335844, 11 pages. https://doi.org/10.1155/2024/1335844.

Grinsted, A., Moore, J.C., Jevrejeva, S. (2004). Application of the cross wavelet transform and wavelet coherence to geophysical time series, Nonlin. Processes Geophys. 11, 561–566, doi:10.5194/npg-11-561-2004.

Hannachi, A. (2004). A Primer for EOF Analysis of Climate Data, Department of Meteorology, University of Reading, 33pp.

Kataoka, R., Shiita, D., Kilpua, E., Keika, K. (2015). Pileup accident hypothesis of magnetic storm on 17 March 2015, Geophys. Res. Lett. 42(13): 5155–5161. https://doi.org/10.1002/2015GL064816.

Morozova, A., Rebbah, R. (2023). Principal component analysis as a tool to extract Sq variation from the geomagnetic field observations: Conditions of applicability, MethodsX, 10, 101999. https://doi.org/10.1016/j.mex.2023.101999

Pais, M.A., Morozova, A.L., Schaeffer, N. (2015). Variability modes in core flows inverted from geomagnetic field models. Geophys J Int 200:402–420. doi:10.1093/gji/ggu403.

Stefan, C., Dobrica, V., Demetrescu, C. (2019-2020). Geomagnetic field characteristics revealed by empirical orthogonal functions, Rev. Roum. GÉOPHYSIQUE, 63–64, p. 63– 67.

Von Storch, H., Navarra, A. (1995). Analysis of Climate Variability: Applications of Statistical Techniques, Springer, 334pp, doi:10.1007/978-3-662-03167-4.

Dose Rate and Flux Measurements During a Travel from Bulgarian Antarctic Base on Livingston Island to Sofia, Bulgaria

Dachev T.P.[1], Sapundjiev P.V.[2], Tomov B.T.[1], Matviichuk Y.N.[1], Mitev M.M.[1], Georgieva[1], K.Ya., Kirov[1], B.B. Jordanova M.M.[1], Krezhov K.A.[1]

[1]Space Research and Technology Institute, Bulgarian Academy of Sciences, Sofia, Bulgaria
[2]National Institute of Geophysics, Geodesy and Geography, Bulgarian Academy of Sciences, Sofia, Bulgaria
[3]Institute of Electronics, Bulgarian Academy of Sciences, Sofia, Bulgaria
tdachev59@gmail.com

Abstract

The radiation risk spectrometer-dosimeter Liulin-AA performed observations in the Bulgarian Antarctic Base on Livingston Island. The battery-operated device also did continues measurements at the back trip from Livingston Island to Sofia, Bulgaria between 24 of February and March 9, 2024. Different radiation and environment conditions were detected during this journey. The latter starts with few days measurements in the Bulgarian Antarctic Base and includes: four trips by car, one travel by ship, four aircraft flights, one of which is crossing the magnetic equator, one travel by bus and two stays in hotels in Punta Arenas, Chile and Buenos Aires, Argentina. The lowest dose rates were measured during the trips by car. The dose rates during the ship travel were smaller than the dose rates on the ground. The dose rates registered in a bricks building in Sofia were higher than the ground dose rates. As expected, the highest dose rates were registered during the aircraft flights. The different dose rates and spectra are described and analyzed in this paper.

Keywords: Antarctic Base absorbed dose rate; Equivalent dose rate; Flux

Introduction

The Bulgarian Antarctic Base "St. Clement Ohridski" (BAB, Fig. 1) is located in the eastern part of Livingston Island, South Shetland Islands. The base was established on April 26-29, 1988. It was named after St. Clement of Ohrid, a prominent Bulgarian scholar and bishop, by a Presidential decree in 1994. The base is used by scientists from Bulgaria and other countries for research in various fields, including geology, biology, glaciology, topography, and geographic information.

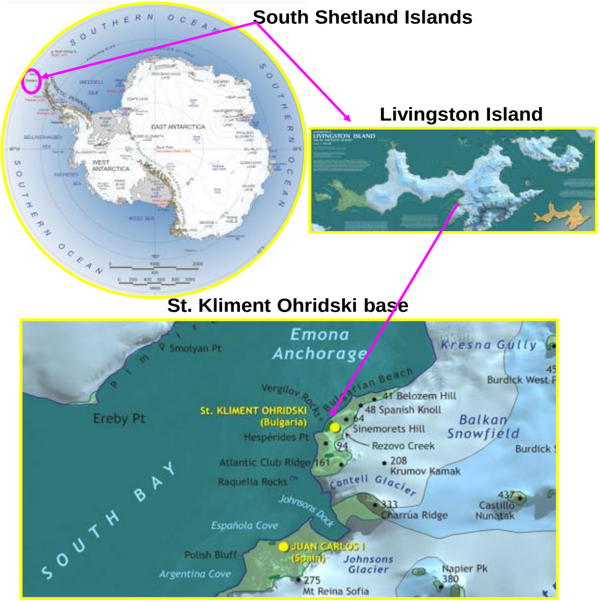

Fig. 1.Geographical position of the The Bulgarian Antarctic Base "St. Kliment Ohridski".

Liulin-AA description

The design of the portable dosimeter-spectrometer Liulin-AA is not a new one. Since 1989, Space Research and Technology Institute (SRTI-BAS), in an international cooperation with scientists from Russia, Germany, Japan, Czech Republic, Italy, Norway, Switzerland, Belgium, USA and India, etc., worked at mountain peaks, flew in space and on stratospheric balloons, rockets and aircraft with more than 35 similar devices [Dachev 2009; Dachev et al, 2015, 2017, Dachev, 2021, http://www.space.bas.bg/SollarTerrestialPhysics/files/Poster-IKIT-BAN-2019%20SZF.pdf].

The last use of Liulin device is the flight of first commercial mission into suborbital space with the SpaceShipTwo spacecraft of Virgin Galactic Company. (Virgin Galactic launches first commercial spaceflight (spacedaily.com)). The flight took place on 29th of June 2023 at 08:00 a.m. MT or 03:00 p.m. GMT from Spaceport America in New Mexico, USA. The preliminary results for the altitudinal profile obtained during the flight were published by Dachev et al, [2023].

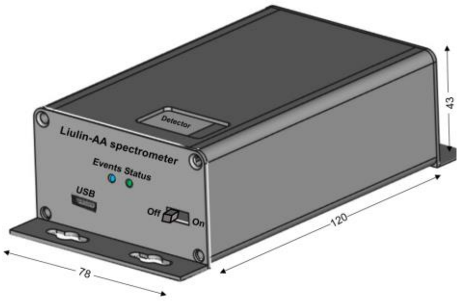

Fig. 2. Draft of Liulin-AA spectrometer.

Liulin-AA spectrometer (Fig. 2) contains one silicon-PIN diode of Hamamatsu S2744-08 type (2 cm^2 area and 0.3 mm thickness, Fig. 4), one ultra-low noise charge-sensitive preamplifier of AMPTEK A225F type (Fig. 2), and 2 microcontrollers.

The doses (deposited energies in the detector) are determined by a pulse height analysis technique and then passed to a discriminator. According to AMPTEK A225 specifications, the pulse amplitudes A [V] are proportional by a factor of 240 mV/MeV to the energy loss in the detector and respectively to the dose. This is the key feature of the AMPTEK A225 preamplifier, which directly transfers the pulse amplitude, measured in volts by the spectrometer to dose and dose rate.

The amplitudes of all signals from the incoming particles and quanta are transformed into digital signals by an ADC converter and are sorted into 256 channels by a multichannel analyzer. For every exposure interval, a single 256 energy deposited spectrum (EDS) is collected.

Two microcontrollers, through specially developed firmware, manage the unit. The Liulin-AA communicates with a personal computer (PC) by a universal serial bus (USB) signal.

The following method for calculations of the dose is used [Dachev et al., 2002]: The dose D [Gy] by definition is one Joule deposited in 1kg of a mater or:

$$D = K.Sum(EL_I * i)_{ET} / MD, \qquad (1)$$

where MD is the mass of the detector in [kg] and EL_i is the energy loss in Joules in channel i. Energy loss in channel i is proportional to the number of events A_i in it multiplied by i. K is a coefficient.

During the construction of the Liulin-AA instrument measures have been taken to reduce the microphone effect at the detector. As a result, it can be seen that when transporting by water, land and air under general conditions, shock and jolt disturbances are not registered anywhere. A new power supply circuit for the detector [Tomchev et al., 2023] has been constructed and used. As a result, the electromagnetic interference and noises were reduced. The device has been calibrated by applying a new methodology [Mitev et al., 2023], which leads to an increase in the accuracy and convergence of the registered data.

Experimental Results

A Preliminary Experiment to Determine the Sensitivity of Liulin-Type Instruments to Various Environmental Conditions

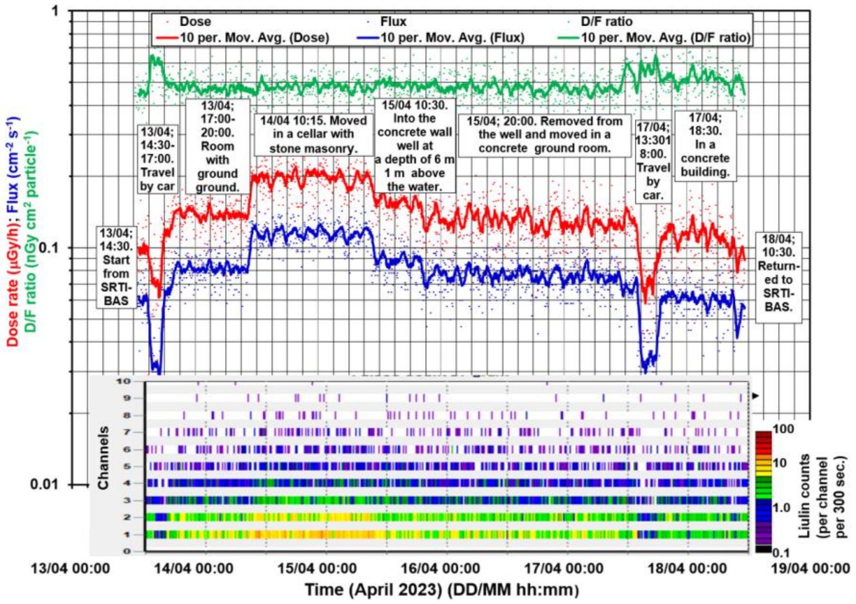

Fig. 3. Five-day battery non-stop experimental use of the Liulin-AA in different places and at different surroundings.

Fig. 3 shows five-day battery non-stop experimental measurements of the dose rate, flux and calculated dose to flux ratio by the Liulin-AA in different places and at different surroundings. The experiment began on 13th of April 2023 at 12:00 in a hut building of our institute. The instrument was initiated at 300 s exposition. The average dose rate in this position is about 0.095-μGy h^{-1}.

From 17:00 to 20:00 hours, the instrument was transported by a car from Sofia to Dimitrovgrad town in central south Bulgaria at a distance of 224 km. Due to the lack of walls and building constructions surrounding the instruments, the dose rate is the smallest observed and is about 0.07-μGy h^{-1}. Remarkable is the mean value enhancement of the dose to flux (D/F) ratio from 0.47 nGy cm^2 particle^{-1} to about 6.3-nGy cm^2 particle^{-1}. This enhancement shows an increase of the number of counts in the higher energy deposition channels where the space radiation component is registries.

After the arrival at the destination, the instrument is placed in a house, on a floor of trampled earth for the period from 20:00 on 13th of April until 10:15 on 14th of April. The dose rate raises up to 0.135-μGy h^{-1}.

Between 10:15 on 14th of April and 10:20 on the 15th of April, the instrument is situated in a cellar with stone masonry. Here the maximal averaged dose rate is about 0.2-μGy h^{-1}. The next position of the instrument is in a well at 6 meter depth from the ground and 1 meter above the water. The walls of the well are covered by concrete cylinders. The dose rate falls down to 0.158-μGy h^{-1}. Next, the instrument is moved to a concrete ground room where the averaged dose rate is 0.13-μGy h^{-1}.

During the journey back from Dimitrovgrad to Sofia on 17 of April between 13:30 and18:10 hour the same small dose rate (0.07-μGy h^{-1}) as during the first travel is observed. Between 18:10 on 17th of April and 09:00 on 18th of April, the instrument is situated in a concrete building room where the dose rate is in average 0.115-μGy h^{-1}. After the return of the instrument in the SRTI-BAS laboratory at 09:50 on 18th of April, the same small dose rates of 0.095-mGy h^{-1} is measured as at the beginning of the experiments on 13th of April.

The conclusions from the five-day non-stop experimental use of the Liulin-AA in different circumstances and different surroundings are:

-The instrument measures stable low dose rates between 0.07 and 0.2-mGy h^{-1}. The smallest dose rate, measured during the car drive of 0.07 μGy h^{-1} is very close to the average ground base dose rate (0.073-mGy h^{-1}), measured in aircraft on the runway before the take-off [Dachev et al. 2013];

- Good repeatability of the data are seen in the two recurrent points - during the car route from and towards the SRTI-BAS of 0.095-mGy h^{-1};

The Liulin type instruments do have a good sensitivity to monitor the dose rates in different environment.

4.2. Environmental Radiation and Commercial Aviation Flights Dosimetry during a Travel from Bulgarian Antarctic Base on Livingston Island to Sofia, Bulgaria

Fig. 4 illustrates the first trip from Livingston Island to King George Island with one blue arrow. The trip by bus from Punta Arenas to Rio Gallegos is a small magenta line. All other trips, by plane, are marked with yellow arrows. The route is shown over a fragment of a map of the estimated ambient dose equivalent rate (μSv h^{-1}) at 11.887 km (FL390) [Makrantoni, et al., 2022].

The white labels next to the flight from Buenos Aires to Rome are the measured in this points equivalent dose rates by Liulin-AA spectrometer. Good coincidence is observed.

Fig 5 contains two panels. In the upper panel depending from the left y-axes are plotted: a) with red line and markers the dose rate and the

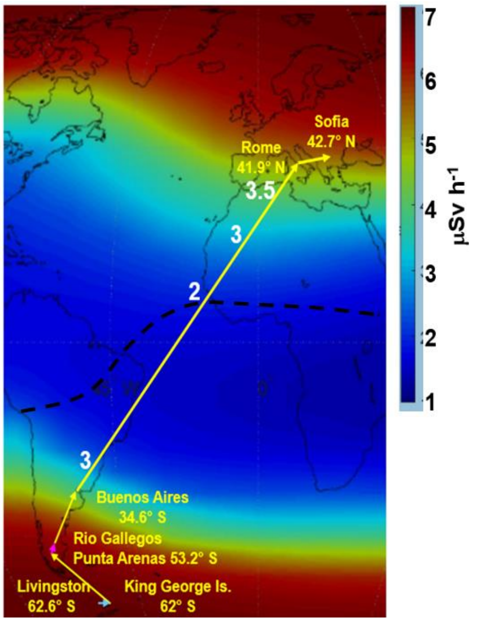

Fig. 4. The return path from Livingstone Island to Sofia, Bulgaria. It is presented over a fragment of a 3D map of the estimated ambient dose equivalent rate at 11.887 km., according to the right side color bar.

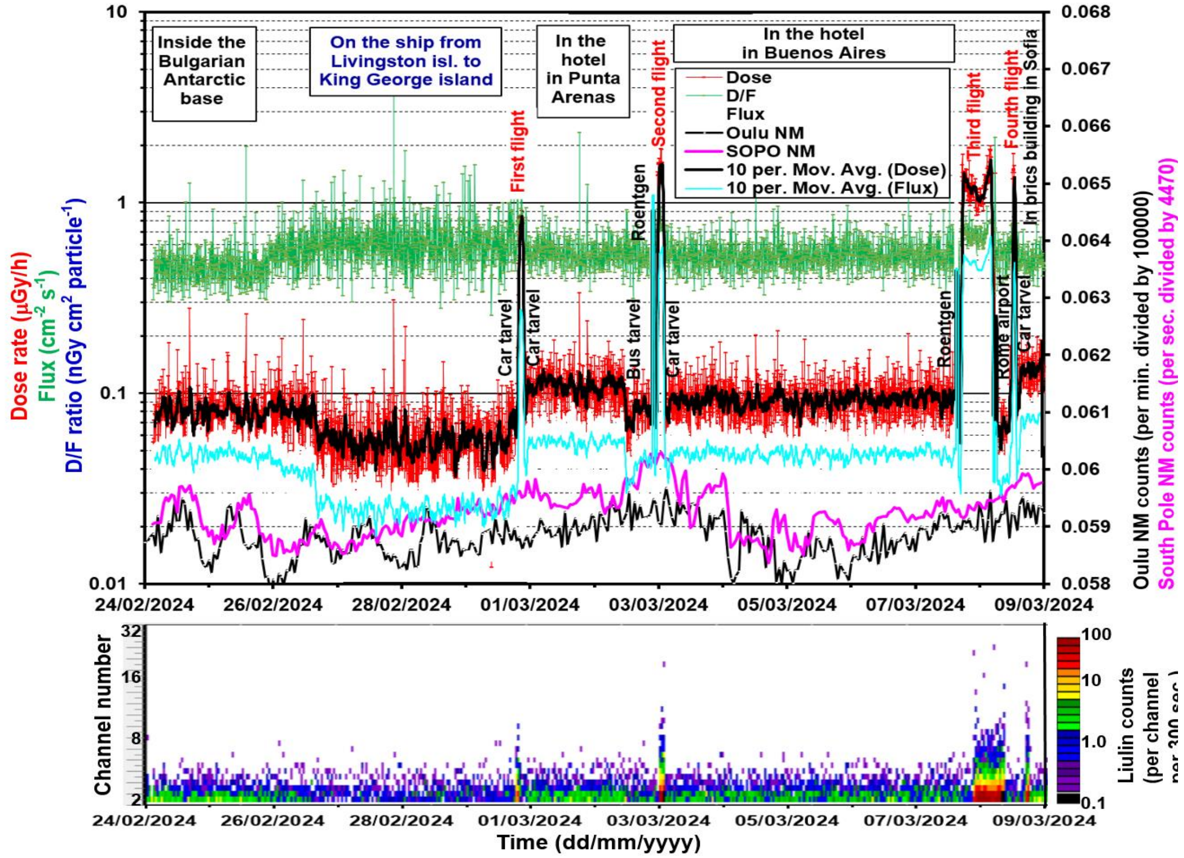

Figure 5. *Environmental radiation and commercial aviation flights dosimetry during a travel from Bulgarian Antarctic Base on Livingston Island to Sofia, Bulgaria.*

10 per mowing average of dose rate with black line; b) with blue line the 10 per moving average of flux; c) the dose to flux ratio with green line and markers.

On the right y-axes of the upper panel are plotted two Neutron Monitor (NM) data: the Oulu NM https://cosmicrays.oulu.fi/ counts (per min. divided by 100000) with a black line and the South Pole NM (SOPO) https://neutronm.bartol.udel.edu/realtime/southpole.html counts divided by 4470 with a magenta line.

In the lower panel of Fig. 5 is situated a 3D color-coded graphic showing the first 32 channels' counts in the spectra population, according to the right side color bar. No significant dependence of the dose rate from the neutron monitors values is observed.

Table 1 contains the averaged values of the absorbed dose rate, equivalent dose rate, flux, dose to flux ratio for the some points of interest of the trip back to Bulgaria.

Table 1. Comparison of the R-PM parameters, measured during experiments with Liulin type spectrometers on balloons and on SpaceShipTwo.

Location and Time	Average measured abs./ amb. eq. dose rate (μGy/h)/(μSv/h)	Average measured Flux (cm^{-2} s^{-1})	Calculated Dose to flux ratio (nGy cm^{2} part.$^{-1}$)	Elevation above the see level (m)
Inside the Bulgarian Antarctic base at Livingston Island, 62.5999° S 60.4999° W, Rc=2.79 GV. **From** 24/02/2024 03:09:00 **Until** 25/02/2024 21:09:00	0.087/1.391	0,047	0.472	12-15
On the ship from Livingston island to King George island, 61.9882° S, 58.0196° W, Rc=2.84 GV. **From** 26/02/2024 16:49:00 **Until** 29/02/2024 15:49:00	0.056/0.0963	0.025	0.622	0.00
First Car travel to King George airport **From** 29/02/2024 18:04:00 **Until** 29/02/2024 18:34:00	0.0532/0.0915	0.26	0.568	
First aircraft flight from King George island to Punta Arenas, Chile, 53.1634° S, 70.9078° W, Rc= 4.54 GV. **From** 29/02/2024 19:19:00 **Until** 29/02/2024 21:14:00	0.808/1.779	0.268	0.862	9,000?
Second Car travel to Punta Arenas hotel **From** 29/02/2024 21:34:00 **Until** 29/02/2024 22:04:00	0.0757/0.130	0.041	0.519	0.516
Inside the Hotel in Punta Arenas, 53.1634° S, 70.9078° W **From** 29/02/2024 22:34:00 **Until** 01/03/2024 20:44:00	0.110/0.189	0.055	0.556	
Bus travel from the Hotel in Punta Arenas to the Airport in Rio Gallegos **From** 02/03/2024 11:09:00 **Until** 02/03/2024 18:14:00	0.078/0.134	0.0393	0.554	
First roentgen security check at Airport in Rio Gallegos **From** 02/03/2024 21:39:00 **Until** 02/03/2024 21:39:00	8.319	10.551	0.219	
Second aircraft flight from Rio Gallegos to Buenos Aires, Argentina, 34.6037° S, 58.3816° W, Rc= 8.44 GV. From 29/02/2024 19:19:00 Until 29/02/2024 21:14:00	1.543/3.696	0.561	0.766	12,000?
Third Car travel from Buenos Aires Airport to the hotel **From** 03/03/2024 05:34:00, **Until** 03/03/2024 06:14:00	0.060/0.1032	0.034	0.599	
Inside the hotel in Buenos Aires 34.6037° S, 58.3816° W **From** 03/03/2024 03:04:00 **Until** 07/03/2024 13:54:00	0.092/1.582	0.0478	0.535	25
Second roentgen security check at Buenos Aires Airport **From** 07/03/2024 15:09:00 **Until** 07/03/2024 15:09:00	3.542	4.102	0.239	
Third aircraft flight Buenos Aires to Rome, Italy, 41.8967° N, 12.4822° E, Rc= 6.2 GV. **From** 07/03/2024 17:24:00 **Until** 08/03/2024 04:09:00	1.16/3.076	0.432	0.670	12,000?
Fourth aircraft flight from Rome to Sofia, Bulgaria, 42.6977° N, 23.3219° E, Rc= 5.9 GV. **From** 08/03/2024 12:19:00 **Until** 08/03/2024 12:54:00	1.496/3.935	0.533	0.780	12,000?
Fourth Car travel from the airport in Sofia **From** 08/03/2024 13:14:00, **Until** 08/03/2024 13:34:00	0.0423/0.0727	0.0213	0.563	
Inside the bricks building in Sofia **From** 08/03/2024 14:24:00 **Until** 09/03/2024 11:09:00	0.133/0.228	0.729	0.509	

The ambient equivalent dose rates in Table 1, were calculated using the developed by [Spurny and Dachev, 2002] and later improved by [Ploc et al., 2011] method.

As seen in the first row of the Table 1, the measurements began "Inside Bulgarian Antarctic Base" on 24 February 2024 and ended on 25 February at 21:29 (Sofia time (UT+ 3 hours)) "Inside bricks building in Sofia (last row).

The measured dose rate inside the Bulgarian Antarctic Base of 0.087 μGy h^{-1} are very similar to the published by [Zanini et al., 2019] doses, obtained at the Argentine Antarctica base in Marambio (Antarctica, 64.24° S, 56.63° W, 196 m a.s.l., vertical cutoff rigidity Rc=2.35 GV). In Table 1, (therein) the measured dose rate is 75.7 ± 3.3 μGy h^{-1} in January-May 2013 and 74.6 ± 2.8 in March-October 2015.

The lowest dose rates of 0.056 μGy h^{-1} and 0.0963 μSv h^{-1} in Fig. 5 were observed during the travel on the ship between Livingston Island and King George Island. The value in μSv h^{-1} is very close to the average dose rate of 0.091 ± 0.010 μSv h^{-1} recorded by the use of a Geiger-Müller Gamma-Scoutevery during the non-stop sailing on the yacht Katharsis II from Cape Town, South Africa to Hobart, Australia around the Antarctic continent between 23 December 2017 and 5th April 2018 [Długosz-Lisiecka, 2021]. The car travel and the bus travel doses, similarly to the measured during Preliminary experiment (Fig. 3), are at low levels between 0.0423 μGy h^{-1} during the car trip between Sofia airport and Sofia town and 0.078 μGy h^{-1} during the bus trip between the hotel in Punta Arenas to the Airport in Rio Gallegos town.

The doses in different buildings during the trip varies between 0.133 μGy h^{-1} inside the brick building in Sofia and 0.092 μGy h^{-1} inside the hotel in Punta Arenas. These high doses are understandable because according to [Shahbazi-Gahrouei et al., 2013, Table 1 therein] the radioactivity concentration in (Bq/kg) in brick is the highest with 37±1.5 from ^{226}Ra, 12.2±0.7 from ^{232}Th and 851.4±15 from ^{40}K. The cement, which is the major contributor in the concrete, is on the second place.

The highest dose rates were observed during the four commercial aircraft flights, depicted on Fig. 6. The maps with the ground projection of the aircraft paths (red lines) are visible in the background of the four figures. In addition, the variations of the ambient equivalent dose rate in μSv h^{-1} (blue lines), the absorbed dose rate in μGy h^{-1} (black lines) and the dose to flux ratio in nGy cm^2 particle^{-1} (magenta lines) are also shown.

The variations of the mentioned above two dose rate parameters during first flight from King George Island (61.9882° S, 58.0196° W, Vertical cut-off rigidity (Rc) is 2.84 GV) to Punta Arenas town in Chile, (1,241 km distance) are seen in Fig. 6a. The measured absorbed and equivalent dose rate during this flight are the smallest in comparison with the other three flights. The reason is that this flight was performed with aircraft type BAe146, which cruise altitude is at about 9 km. The highest average dose to flux value of 0.862 nGy cm^2 particle^{-1} in comparison with other three flights gives information that in the spectra exist particles depositing energy in higher energy channels. This is expected due to the relative high latitudes of the flight.

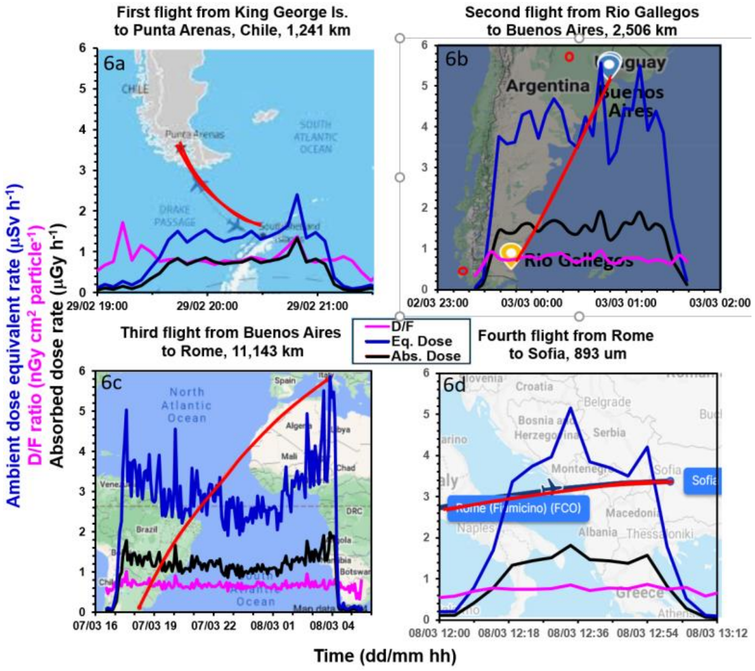

Figure 6. *Environmental radiation and commercial aviation flights dosimetry during a travel from Bulgarian Antarctic Base on Livingston Island to Sofia, Bulgaria.*

The high dose rates seen in the second and fourth flights are very similar because of the similar latitudinal (please look Fig. 4) and altitudinal conditions. This is also expected because the cruise altitude of flights 2-4 is around 12 km.

The most interesting, is the third flight being the longest and crossings the geomagnetic equator (please look at the dashed black line, Fig. 4) somewhere on the west coast of Africa. Both sides of the path in both hemispheres are from -35° to 42° geographic latitudes and Rc=6.2 GV and Rc=5.9 GV. Close after the take-off from the Buenos Aires airport and before the landing in Rome, the predicted ambient dose equivalent [Makrantoni, et al., 2022] is about 4-6 μSv h^{-1}. The latter is in a good coincidence with the values in the blue line (Fig. 6). With the decrease of the latitude toward the magnetic equator (black dashed line, Fig. 4), the doses also decrease down to values of 2-2.5 μSv h^{-1}.

Conclusions

The most important achievement of the paper is the discovery and the proof of the existence of stable measurements of Liulin type instruments in different ground and aircraft circumstances and different natural radiation surroundings.

Acknowledgements

The authors thank to all Bulgarian and foreign specialists and organizations that participated in the development of the Liulin instruments. BAS, NSFI, PECS and our international partners for the financing of projects related to the creation of Liulin equipment.
Peter Sapundjiev is very thankful to Project/Contract No 70-25-94 from 28.04.2023, Supported by National Program for Polar Studies "From Pole to Pole" 2022 – 2025.
This study was supported by grant KP-06-N44/2 with the Bulgarian Science Fund, 27.11.2020.

References

Dachev, T., Tomov, B., Matviichuk, Y., Dimitrov, P., Lemaire, J., Gregoire, G., Spurny, F., 2002. Calibration results obtained with Liulin-4 type dosimeters. Adv. Space Res. 30, 917–925. https://doi.org/10.1016/S0273-1177(02)00411-8.

Dachev, T.P., 2009. Characterization of near Earth radiation environment by Liulin type instruments. Adv. Space Res. 44, 1441–1449. https://doi.org/10.1016/j.asr.2009.08.007.

Dachev, T.P., Semkova, J.V., Tomov, B.T., Matviichuk, Y.N., Dimitrov, P.G., Koleva, R.T., Kubancak, I.N., 2015a. Overview of the Liulin type instruments for space radiation measurement and their scientific results. Life Sci. Space Res. 4, 92–114. https://doi.org/10.1016/j.lssr.2015.01.005.

Dachev, T.P., Bankov, N.G., Tomov, B.T., Matviichuk, Y.N., Dimitrov, P.G., Häder, D.-P, Horneck, G., 2017. Overview of the ISS radiation environment observed during the ESA EXPOSE-R2 mission in 2014–2016. Space Weather, Vol. 15, 1475–1489, https://doi.org/10.1002/2016SW001580.

Dachev T., Dimitrov P., Tomov B., Matviichuk Y., Semkova J., Koleva R., Jordanova M., Bankov N., Mitev M., Carlucci P., Cairo F., Kostadinov I., Paciucci L., Prediction and Measurement of the Space Radiation Altitudinal Profile during the Flight of the Virgin Galactic SpaceShipTwo, Proceediings of the Thirteenth Workshop "Sollar Inflluences on the Magnetosphere Ionosphere and Atmosphere", ISSN 2367-7570, 177-182, September, 2021.

Długosz-Lisiecka, M., Krystek, M., Koper, M., Grala, T., Leniec-Koper, H., Barasiński, M., Talar, M., Kamiński, I., Kibart, R., Małecki, W. and Kukliński, P., 2021. ACTA UNIVERSITA TISLODZIENSIS Folia Geographica Physica 20, 2021: 7–12, Natural gamma radiation at the sea level around the Antarctic continent recorded south of the 62° parallel. https://doi.org/10.18778/1427-9711.20.01.

Makrantoni, P., Tezari, A., Stassinakis, A.N., Paschalis, P., Gerontidou, M., Karaiskos, P., Georgakilas, A.G., Mavromichalaki, H., Usoskin, I.G., Crosby, N. and Dierckxsens, M., 2022. Estimation of Cosmic-Ray-Induced Atmospheric Ionization and Radiation at Commercial Aviation Flight Altitudes. Applied Sciences, 12(11), p.5297.

Mitev, M., L. Tsankov, T. Dachev, B. Tomov, Y. Matviichuk and N. Tomchev, "Radiationless energy calibration of radiation survey meters," *2023 XXXII International Scientific Conference Electronics (ET)*, Sozopol, Bulgaria, 2023, pp. 1-4. https://doi.org/10.1109/ET59121.2023.10279419.

Ploc, O., Pachnerova Brabcova, K., Spurný, F., Malušek, A. and Dachev, T., 2011. Use of energy deposition spectrometer Liulin for individual monitoring of aircrew. Radiation Protection Dosimetry, *144*(1-4), pp.611-614. 10. https://doi.org/1093/rpd/nc0000.

Shahbazi-Gahrouei, D., Gholami, M. and Setayandeh, S., 2013. A review on natural background radiation. Advanced biomedical research, *2*(1), p.65. https://doi.org/10.4103/2277-9175.115821.

Spurný, F. and Dachev, T., 2002. On board aircrew dosimetry with a semiconductor spectrometer. Radiation protection dosimetry, *100*(1-4), pp.525-528. https://doi.org/10.1093/oxfordjournals.rpd.a005928

Tomchev, N., Mitev, M., Tsankov, L. Novel Linear Step-up Power Supply Module for Detector Systems. Proceedings 32nd International Scientific Conference Electronics, ET 2023, Institute of Electrical and Electronics Engineers Inc., 2023, ISBN:979-835030200-4, https://doi.org/10.1109/ET59121.2023.10279817,1-4.

Zanini, A., Vernetto, S., Ciancio, V., Di Giovan, G., Morfino, P., Liberatore, A., Giannini, G. and Hubert, G., 2019. Environmental radiation dosimetry at high southern latitudes with Liulin type instruments. Journal of environmental radioactivity, *208*, p.105993. https://doi.org/10.1016/j.jenvrad.2019.105993.

An Assessment of the Radiation Risk in Orbit Around Mars, Based on Measurements by the Lyulin Instrument and Numerical Simulations

Krastev K.[1]*, Semkova J.*[1]*, Koleva R.*[1]*, Benghin V.*[2]*, Drobyshev S.*[2]

[1]Space Research and Technology Institute, Bulgarian Academy of Sciences
[2] Institute of Biomedical Problems of Russian Academy of Sciences

Abstract

In this paper, we present the results of the numerical modeling of the Liulin device. Some effects that occur when ionizing radiation is detected by a system of detectors (telescope) are described.

Introduction

The issues and methodology discussed in this article follow those presented in [Krastev et all., 2023a]. Here we will focus on the influence of the geometry of the detectors and the design of the Liulin - MO device on the measured fluxes and doses. The Lyulin-MO dosimetry module of the FREND instrument provides information on the radiation environment during the cruise stage and in orbit around Mars [Semkova et al, 2018]. A schematic diagram of the construction and geometry of the instrument's detectors is shown in Figure 1.

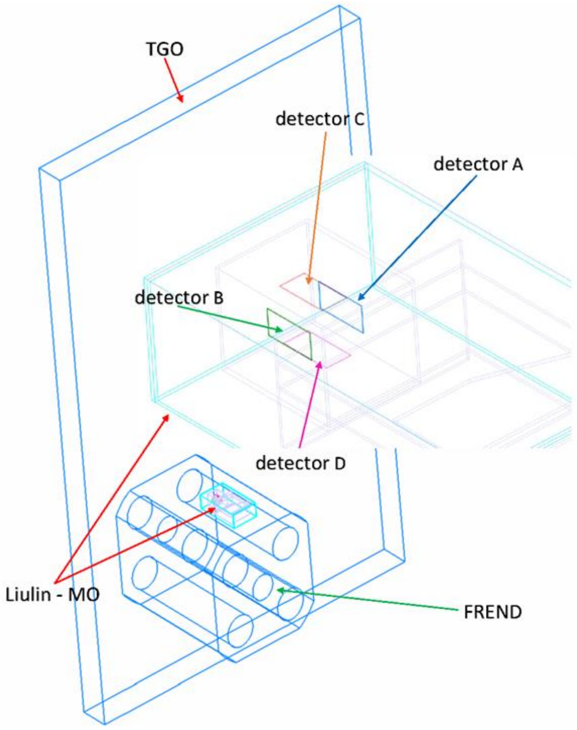

Figure 1. *The detector circuit of the Lyulin-MO equipment on board TGO.*

One of the significant effects affecting the accuracy of measurements is shown in Figure 2.

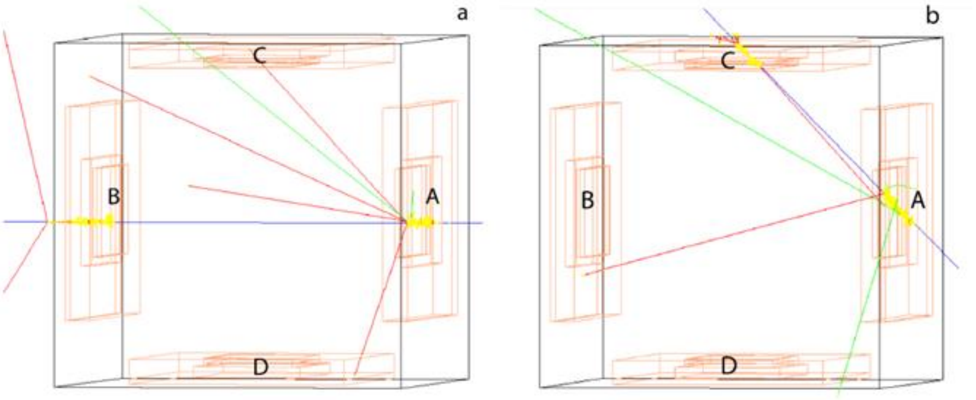

Figure 2. *Examples of true and false signals: a) A heavy particle (shown in blue) passes through each of the detectors A and B included in the telescope AB. This is an example of a real coincidence. Here, a parasitic signal is generated by a DC telescope. Detectors D and C register secondary electrons in the matching mode and give a false match; b) A heavy particle (blue color) passes through only one of the detectors (detector A), a coincidence is recorded caused by the ingress of secondary particles (red color) into detector B. In this case, we have a false match.*

Methods

The methodology for research and evaluation of the specified effects follows that described in [Krastev et all., 2023]. The corresponding distribution for the GCR flux is taken from the NASA OLTARIS database (https://oltaris.larc.nasa.gov/), Figure 3. The GCR model of Badhwar O'Neil (BON 2020) [Slaba & Withman, 2020] is used. Data used for the period from April 15, 2016 to September 15, 2016.

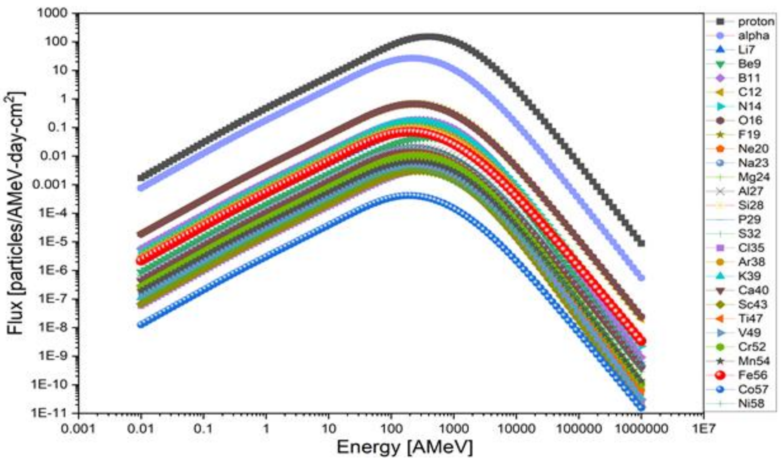

Figure 3. *Spectrum of galactic cosmic rays GCR from NASA's OLTARIS database*

Results

Figure 4 shows for each component of the GCR spectrum in which energy range it is registered. It can be seen from the figure that heavy elements, due to the effects shown in Figure 2, are registered in a lower energy range than they should be. This effect has a minor role in the formation of the flux since it is overshadowed by the recorded protons and alpha particles whose count rate is orders of magnitude higher. In the considered case of protection, the highest energy part of the spectrum is formed by registration of iron ions, but Mg24 and Si28 ions have a significant contribution.

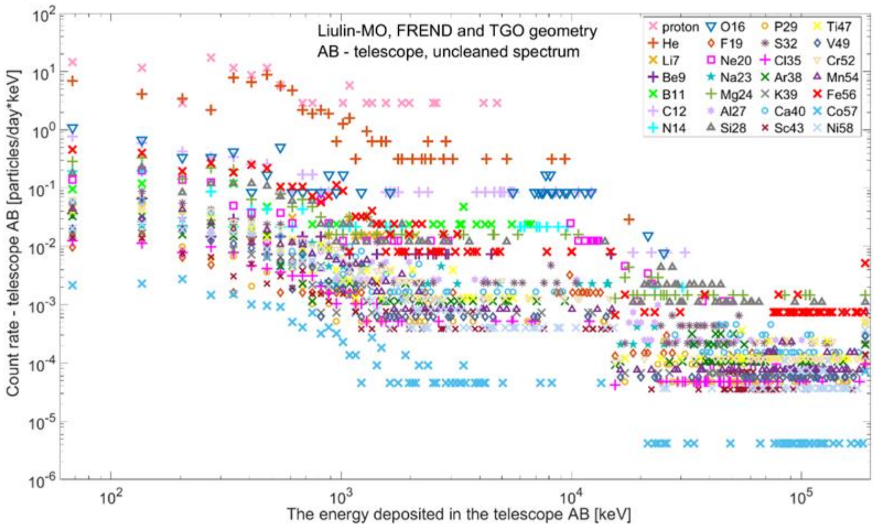

Figure 4. *Count rate (uncleared) of the AB telescope, for each component of the GCR, calculated from the simulation. The protection includes Lyulin-MO, FREND and TG*

Figure 5 shows how the readings of the detector system depend on the surrounding structures and materials. For a more precise analysis, the geometric factors are calculated separately for detectors A and B, denoted by GA and GB, respectively. From Figure 5 it can be seen that the geometric factor GB for the high-energy range obtained in the case of shielding is 35 cm^2 sr, and this same GB factor in the case of zero shielding is 1.4 cm^2 sr. It can be said that the role of electrons in event registration increases sharply in the case of protection of the detector system. On the contrary, in the high-energy range, the geometric factor in the case of shielding is smaller than that for zero shielding. This can be explained by the shielding of part of the GCR flux by the construction of Lyulin-MO, FREND and TGO.

Figure 6 shows the cleaned spectra for the AB telescope. It can be seen from the figure that only protons and alpha particles are present in the lowest energy range. It can also be noted that the cleaned spectra lack the "tails" of most of the components, i.e. the events in which the recorded energy goes beyond the scope of the telescope (192 MeV). Here, by a cleaned spectrum, we will understand a simulated spectrum from which parasitic signals are removed.

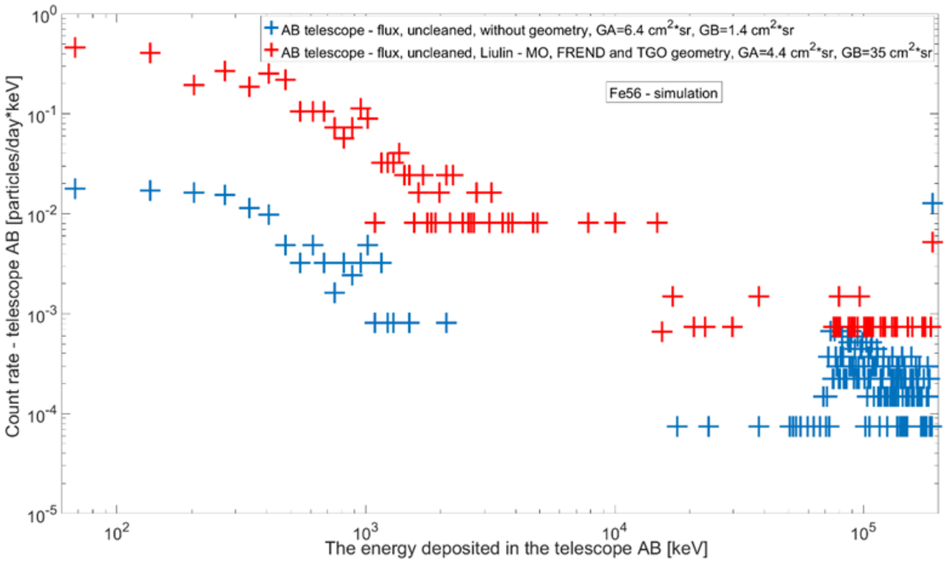

Figure 5. *Count rate (uncleared) of the AB telescope, for Fe56 from the GCL spectrum, calculated from the simulation for the cases without shielding and with shielding by the construction. Protectione includes Liulin-MO, FREND and TGO.*

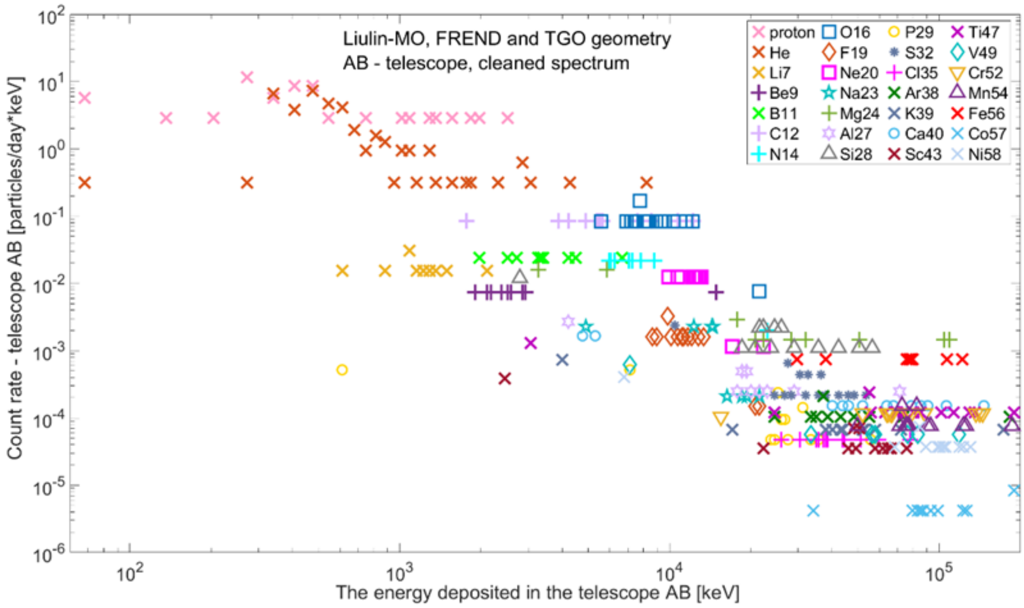

Figure 6. *Count rate (cleared) of the AB telescope, for each component of the GCR, calculated from the simulation. protection includes Lyulin-MO, FREND and TGO.*

Conclusion

The obtained numerical simulation results show that the registration of ionizing radiation by detector systems (telescopes) is accompanied by the appearance of undesirable effects that distort the detector response. Failure to take these effects into account in some cases leads to overestimation of measurements by several times. The use of false signal cleaning methods [Krastev et all., 2023b], which are not considered here, leads to results close to those obtained experimentally [Semkova, J., et al, 2018; Zeitlin, C., et al. 2013].

References

Krastev K., et al 2023a. Numerical Simulation of the LIULIN-MO Device, pp.88-94, Proceedings of the 15th Workshop "Solar Influences on the Magnetosphere, Ionosphere and Atmosphere" June, 2023, ISSN 2367-7570, pp.88-94, https://spaceclimate.bas.bg/ws-sozopol/pdf/Proceedings2023.pdf

Krastev, K. et al, 2023b, Numerical simulation of Liulin-MO instrument for measuring cosmic radiation onboard Exomars Trace Gas Orbiter, Comptes rendus de l'Académie bulgare des Sciences, Tome 76, No , 2023

Semkova, J., et al, 2018. Charged particles radiation measurements with Liulin-MO dosimeter of FREND instrument aboard ExoMars Trace Gas Orbiter during the transit and in high elliptic Mars orbit, Icarus, Vol. 303, Pp 53-66, https://doi.org/10.1016/j.icarus.2017.12.034

Slaba T. & K. Withman, „The Badhwar-O'Neill 2020 GCR Model", AGU, Volume18, Issue 6, 2020

Zeitlin, C., et al. 2013. Measurements of Energetic Particle Radiation in Transit to Mars on the Mars Science Laboratory, Science 340, 1080 (2013)

Solar Influence on Chandler Period

Chapanov Ya.[1], *Ron C.*[2], *Vondrak J.*[2]

[1]Climate, Atmosphere and Water Research Institute, Bulgarian Academy of Sciences (CAWRI-BAS),
yavor.chapanov@gmail.com
[2]Astronomical Institute, Czech Academy of Sciences (AI-CAS)

Abstract

The Chandler wobble (CW) is a free rotational mode of the Earth associated with its dynamical ellipticity. In the absence of external force, the CW would have a period of about 433 days. The Chandler wobble is excited by a combination of atmospheric and oceanic processes, with the dominant excitation mechanism being ocean-bottom pressure fluctuations, caused by ocean circulation and variations in temperature, salinity, and winds. The most important energy sources of all atmospheric and oceanic processes are the solar activity cycles, so the solar cycles affect climatic system and angular momentum of atmosphere and ocean, followed by polar motion and Chandler period variations. The Chandler period variations are determined from the coordinates of polar motion for 1860-now from the solution C01 of the IERS. The centennial, decadal and interannual harmonics of solar activity are determined by the Method of Partial Fourier Approximation of time series of the Total Solar Irradiance (TSI), Sunspot Numbers (SSN) and North-South Solar Asymmetry (N-S SA). The long-term variations of CW period are compared with corresponding cycles of N-S SA. The decadal and interannual oscillations with periods above 6yr of CW have good agreement with the TSI cycles in several frequency bands. The short-term CW oscillations have good agreement with SSN cycles in two bands of periodicity between 3 and 4 years. It is remarkable that the CW grand minimum around 1930 is strongly connected with all solar harmonics with dominating influence of long term N-S SA variations (periodicity 78-156yr, CW period decrease - 6d) and TSI variations (periodicity 39-52yr, CW period decrease - 10d). The TSI influence on CW period variations is non-linear and frequency dependent. The value of CW period increase during the warming cycles of solar activity and decrease during some solar minima.

Keywords: Chandler period, TSI, SSN, North-South solar asymmetry.

Introduction

The solar activity affects terrestrial systems by means of direct radiation over Earth surface, influences charged particles of the solar wind, and the solar magnetic field. The solar wind directly affects Earth magnetic field, ionosphere and atmosphere. The sunspot numbers represent both TSI and solar wind variations. The SSN and TSI variations are highly correlated in decadal period bands, and they have some differences in annual period bands. The variations of solar magnetic field modulate solar wind and cosmic rays in the frame of the solar system. The North-South solar asymmetry represents significant part of solar magnetic field variations. The cosmic rays near Earth are modulated by Earth magnetic field variations, too. The TSI and cosmic ray variations affect climate system and motion of ocean and atmosphere, whose small variations stay in the source of Chandler wobble excitation. So, we may expect significant solar influence on Chandler wobble variations, expressed by strong correlation in selected frequency bands between Chandler period value and any of solar activity indices – TSI, SSN or N-S solar asymmetry. The Chandler period variations have two anomalies: in 1926, when the period significantly decrease; and in 2011, when the Chandler oscillation almost disappear from the polar motion.

Data and Methods

a) Solar and terrestrial data

The solar activity variations are presented by several numerical indices (Fig. 1). The most popular of them are indices of sunspot numbers, sunspot area and TSI. The sunspots have been observed during the last 4 centuries, while the real observations of TSI are available only for the last decades.

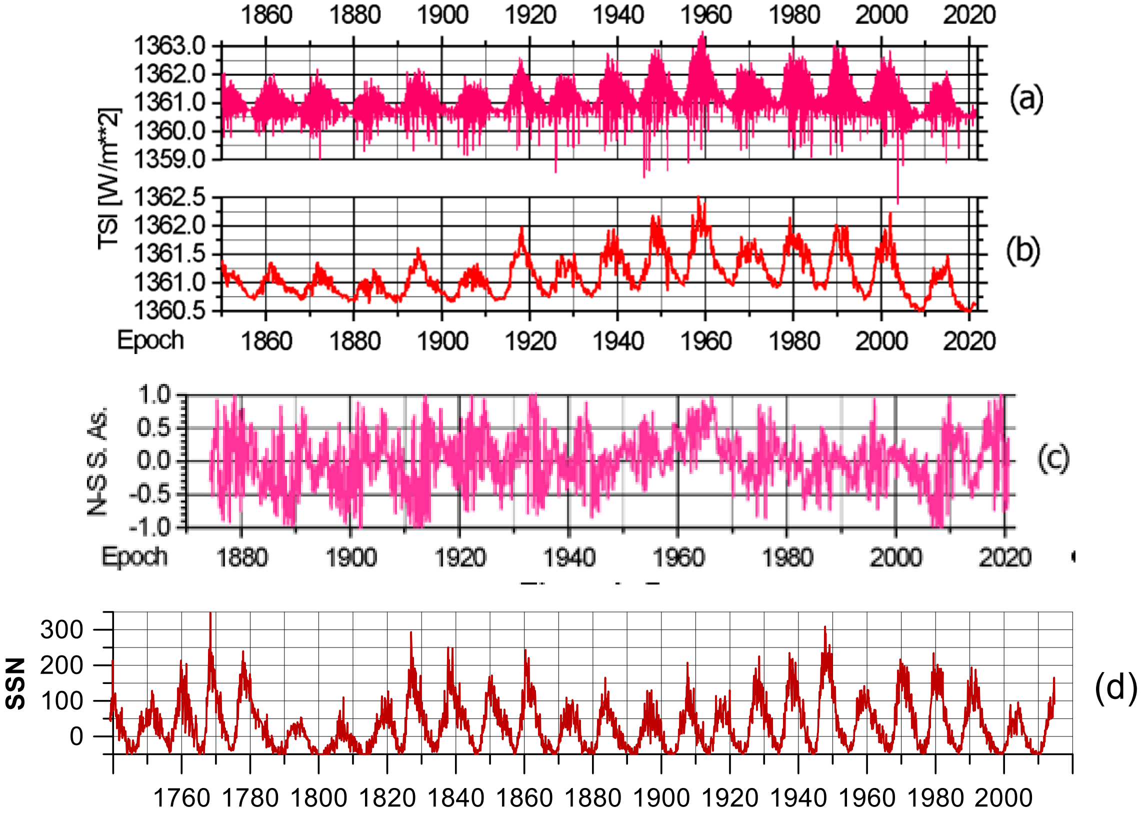

Figure 1. *Time series of solar indices: reconstructed daily values of TSI – (a); 0.1-year normal points of TSI – (b); North-South solar asymmetry – (c); and sunspot numbers – (d).*

The TSI data are presented in Fig.1, a, b. The last version of estimated solar irradiances for the last 400 years is based on the NRLTSI2 historical TSI reconstruction model by J. Lean (Kopp et al., 2016; Lean, 2000, 2010; Coddington et al., 2015). The North-South solar asymmetry (Fig.1, c) is determined from the relation $(S_n\text{-}S_s)/(S_n+S_s)$, where the S_n and S_s are monthly sunspot area on the Northern and Southern solar hemispheres, respectively (in units of millionths of a hemisphere). The data since 1874 are observed by the Royal Greenwich Observatory and merged after 1976 with the US Air Force (USAF) and the US National Oceanic and Atmospheric Administration (NOAA) data by D. Hathaway (https://solarscience.msfc.nasa.gov/greenwch.shtml). The daily and monthly values of SSN are provided by the Royal Observatory of Belgium (Fig.1, d).

The variations of the value of Chandler period (Fig.2) are calculated by the method, described in (Vondrak et al., 2005). The polar motion coordinates (Fig. 3) are from the solution C01 of the IERS. They have two anomalies – in 1926 and 2011, when the Chandler amplitude stands almost zero. In 1926 the Chandler period significantly decrease to 380 days, instead of its mean value of 431 d. In 2011 and next years the estimated Chandler period stays closed to its mean value with the exception in 2018, when it decreases to 390 d (Fig. 2).

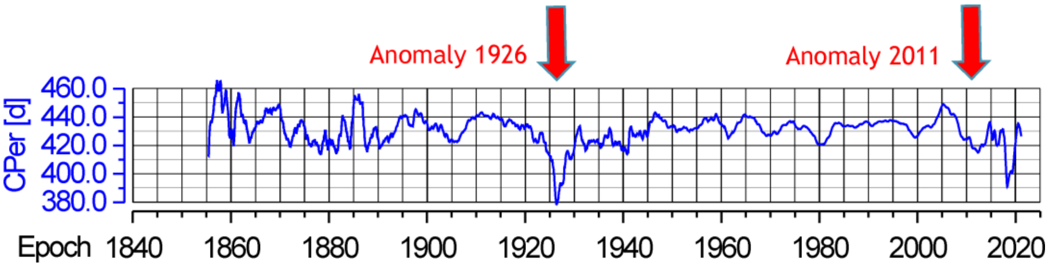

***Figure** 2. Variations of Chandler period value since 1850.*

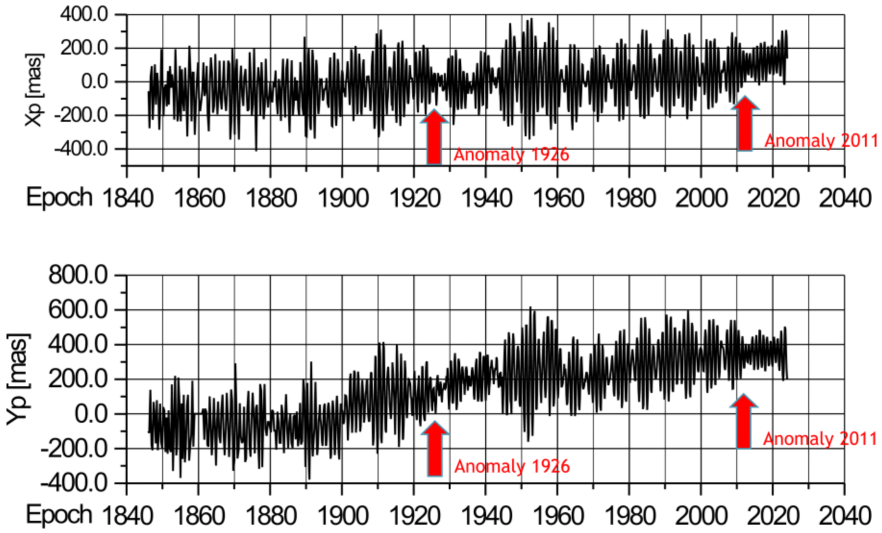

***Figure 3.** Coordinates of polar motion Xp and Yp for the period 1860-now from the solution C01 of the IERS.*

b) Method of Partial Fourier Approximation

The periodical variations are derived from the data by means of partial Fourier approximation based on the Least-Squares (LS) estimation of Fourier coefficients. The Partial Fourier approximation $F(t)$ of discrete data is given by

$$F(t) = f_0 + f_1(t-t_0) + \sum_{k=1}^{n} a_k \sin k\frac{2\pi}{P_0}(t-t_0) + b_k \cos k\frac{2\pi}{P_0}(t-t_0), \tag{1}$$

where P_0 is the period of the first harmonic, t_0 - the mean epoch of observations, f_0, f_1, a_k and b_k are unknown coefficients and n is the number of harmonics of the partial sum, which covers all oscillations with periods between P_0/n and P_0. The application of the LS estimation of Fourier coefficients needs at least $2n$+2 observations, so the number of harmonics n is chosen significantly smaller than the number N of sampled data f_i. The small number of harmonics n yields to LS estimation of the coefficient errors. This estimation is the first essential difference with the classical Fourier approximation. The second difference is the arbitrary choice of the period of first harmonic P_0, instead of the observational time span, so the estimated frequencies may cover the desired set of real oscillations. This method allows a flexible and easy separation of harmonic oscillations into different frequency bands by the formula

$$B(t)=\sum_{k=m_1}^{m_2} a_k \sin k\frac{2\pi}{P_0}(t-t_0)+b_k \cos k\frac{2\pi}{P_0}(t-t_0), \tag{2}$$

where the desired frequencies ω_k are limited by the bandwidth

$$\frac{2\pi m_1}{P_0} \le \omega_k \le \frac{2\pi m_2}{P_0} \tag{3}$$

After estimating the Fourier coefficients, it is possible to identify a narrow frequency zone presenting significant amplitude, and defining a given cycle. Then this cycle can be reconstructed in time domain as the partial sum limited to the corresponding frequency bandwidth. Doing this for terrestrial and solar time series, we shall identify their respective cycles, isolate and compare the common ones.

Results

Common cycles of Chandler period variations and solar indices are determined in several narrow frequency bands (Figs. 4-6). The SSN affects short-term oscillations with periods below 4 years (Fig. 4). The N-S solar asymmetry correlates with long-term Chandler oscillations with time lag equal to the 22-year Hale magnetic solar cycle (Fig. 5). The Anomaly 1926 starts when the decadal cycles of TSI have local minima (Fig. 6).

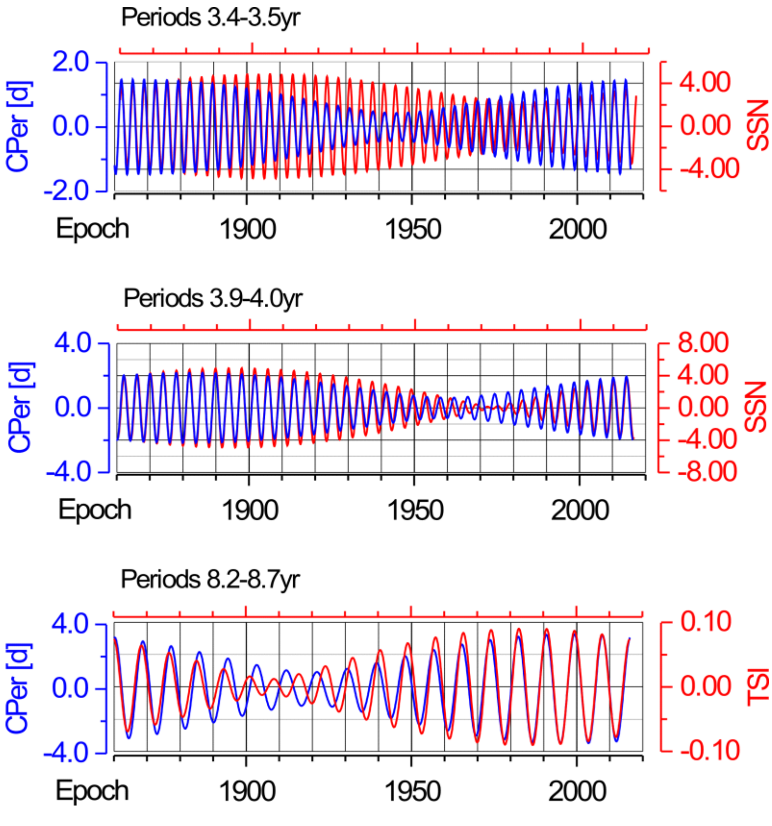

Figure 4. *Subdecadal variations of Chandler oscillation with periodicity 3.4 – 8.7 year.*

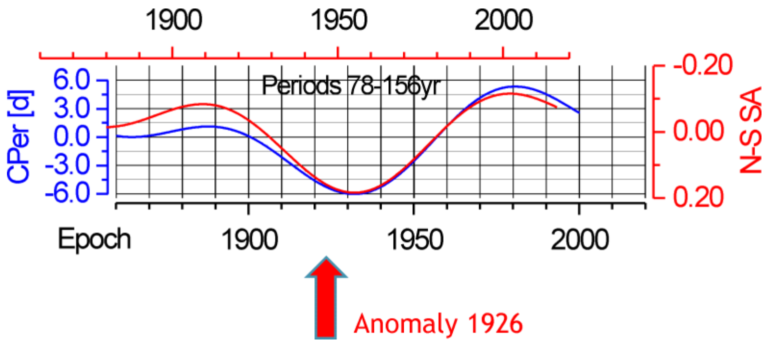

***Figure** 5. Long-term variations of Chandler period with minimum after the anomaly 1926.*

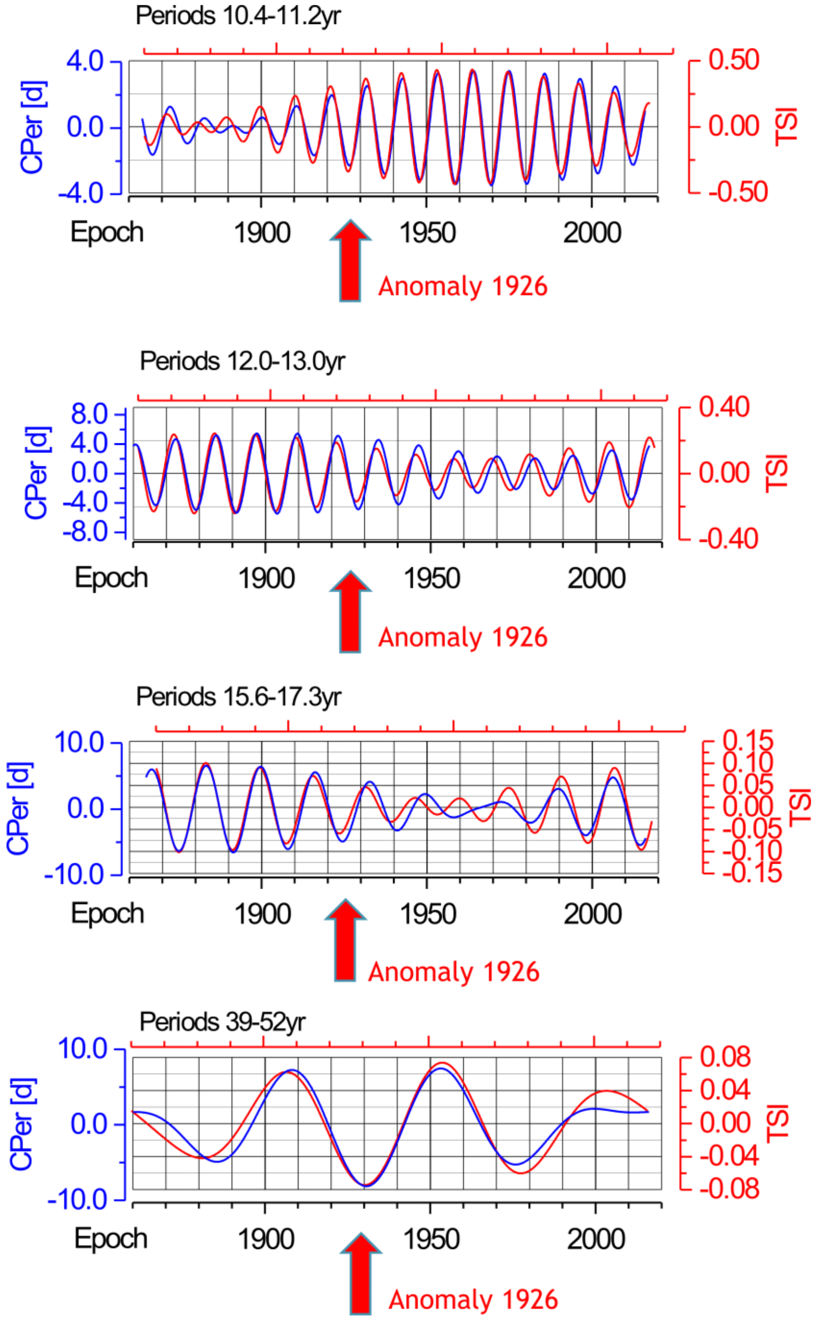

***Figure 6.** Common decadal cycles of TSI and Chandler period. The Anomaly 1926 occurs during local minima of TSI cycles.*

Conclusions

The time series variations are separated in several interannual and decadal frequency bands by PFA with periods 3.4-3.5yr; 3.9-4.0yr; 6.2-6.5yr; 8.2-8.7yr; 10.4-11.2yr; 12.0-13.0yr; 15.6-17.3yr; 39-52yr and 78-156yr, where good correlation exists between solar indices and Chandler period variations. The long-term variations of the Chandler period are affected by N-S solar asymmetry, where the time lag is equal to the 22-year Hale magnetic solar cycle. Excellent agreement between TSI and Chandler period variations exists for oscillations with periodicities 39-52yr and all cycles with periods between 6 and 17 years. The interannual oscillations with periods below 4 years are affected by the SSN variations.

The CW grand minimum in 1926 is strongly connected with all solar harmonics with dominating influence of long-term N-S SA variations (periodicity 78-156yr, CW period decrease - 6d) and TSI variations (periodicity 39-52yr, CW period decrease - 10d; periodicity 15.6-17.3, CW period decrease – 5d; periodicity 12-13yr, CW period decrease – 4d). The TSI influence on CW period variations is non-linear and frequency dependent. The value of CW period increase during the warming cycles of solar activity and decrease during some solar minima. This result means that the solar activity significantly affects the polar motion and CW variations by intermediate climatic variations in ocean and atmosphere.

References

Coddington, O., Lean, J.L., Pilewskie, P., Snow, M. and Lindholm, D.: 2015, A solar irradiance climate data record, Bull. American Meteorological Soc. doi: 10.1175/BAMS-D-14-00265.1

Kopp, G., Krivova, N., Lean, J., and Wu, C.J.: 2016, The Impact of the Revised Sunspot Record on Solar Irradiance Reconstructions, Solar Physics. doi: 10.1007/s11207-016-0853-x

Lean, J.: 2000, Evolution of the Sun's spectral irradiance since the Maunder Minimum. Geophysical Research Letters, 27, 16, 2425-2428. DOI: 10.1029/2000GL000043

Lean, J.L.: 2010, Cycles and Trends in Solar Irradiance and Climate, Wiley Interdisciplinary Reviews, Climate Change 1. doi: 10.1002/wcc.018

Vondrak,C.R.,and C.Ron (2005),The great Chandler wobble change in 1923-1940 re-visited, in Forcing of Polar Motion in the Chandler Frequency Band: A Contribution to Understanding Interannual Climate Variations, edited by H.-PPlag et al.,Cah.du Cent. Eur.de Geodyn.et de Seismol.,vol.24,Walferdange, Luxembourg

Proceedings of
the Sixteenth Workshop "Solar Influences on the Magnetosphere, Ionosphere and Atmosphere"
June, 2024

Hypothetic Explanation of Peculiar Atmospheric Electric Response to SEP at High Latitudes. Experimental Evidence.

Tonev P.

Space Research and Technology Institute BAS, Sofia, Bulgaria, e-mail: peterton@abv.bg

Abstract.

Measurements of atmospheric electric characteristics which have been conducted at high geomagnetic latitudes during several strong solar proton events with ground-level enhancements include in each case a long time interval of unusually large (twice or bigger) increase of the vertical electric current J_z in stratosphere, or of the atmospheric electric field E_z at surface. Since these enhancements are not transient variations they demonstrate presence of an additional electric circuit superimposed to the global atmospheric electric circuit during SPE. An explanation is proposed based on the following processes: *i*) positive charge injection into polar atmospheric regions R_p; *ii*) gradual, yet eventually dramatic decrease of conductivity in R_p due to aerosol increase. This explanation is confirmed by rocket-borne data for electric characteristics in stratosphere and mesosphere during a major solar proton event.

Introduction.

Studied are the results from measurements of the vertical electric field E_z and related current J_z in the stratosphere (*Holzworth et al., 1987*; *Kokorowski et al, 2006*), as well as at surface (*Shumilov et al, 2015*) at high/ sub-high geomagnetic latitudes during four strong solar proton events (SPE) with ground level enhancement (GLE) (*Mironova et al., 2015*). In the first two cases, *S1*, *S2*, we consider the variations of E_z, conductivity σ, and $J_z=\sigma E_z$ in stratosphere during two SPE/GLE, respectively: *S1*) on 16-th February 1874 (*Holzworth et al., 1987*); *S2*) on January 20 2005 (*Kokorowski et al., 2006*). The next two cases concern measurements at surface of the atmospheric electric field E_z during two SPE/GLE in 2001, respectively, on 15-th (case *G1*), and 18-th April (case *G2*) (*Shumilov et al., 2015*). Each of these experiments demonstrate a well-expressed peculiarity of the similar type (*Tonev, 2022; Tonev and Asenovski, 2023*). This peculiarity is represented by unusually large (100% or more) long-term (tens of minutes to several hours) positive deviation of the vertical electric current J_z (and of related electric field E_z) from the electric current J_{FW} ~2 pAm^{-2} Sm^{-1} from the ionosphere to surface by fair-weather conditions (*Tonev, 2022*). These extremely large deviations of J_z and E_z from their typical values occur close to the SPE peak in each case.

The peculiar large deviations of J_z and E_z from their usual values cannot be explained by the theory of an isolated global atmospheric electric circuit (GEC) (Rycroft et al., 2008). Similarly to (*Tonev, 2022*; *Tonev and Asenovski, 2023*) we conclude that an additional electric circuit (current $\mathbf{J}_S$) is created during SPE and is superimposed to GEC. This circuit is responsible for modifications of the vertical electric current J_z in cases *S1,2, G1,2,* as follows:

$$J_z = J_{FW} + J_{Sz} \tag{1}$$

Here J_{Sz} is the vertical component of superimposed current $\mathbf{J}_S$ below ~35 km at high latitudes.

Experimentally determined characteristics of peculiarity in cases *S1,2, G1,2*.

We characterize the peculiarity represented by (1) in each of cases *S1,2, G1,2* by the time interval Δt of the peculiar increase of J_z or E_z, and the maximum deviation J_{zmax} or E_z during Δt, similarly to (*Tonev and Asenovski, 2023*). In case *S1* (*Holzworth et al., 1987*) we study the variations of current $J_z=\sigma E_z$ at altitude 26 km at two balloon stations located at: *a*) (44.6°S, 142.7°E) with invariant latitude Λ= –56.3° (cutoff rigidity 1.4 GV); *b*) (38.7°S, 65.7°E),

Λ=–48.8° (cutoff rigidity 2.8 GV). At location *a*) J_z increases twice (from J_z= 2.25 pAm^{-2} to $J_{z\max}$= 4.5 pAm^{-2}), and remains modified for Δt ~ 0.5 hour. No modifications of σ, E_z and J_z take place at balloon station *b*) located at the lower latitude. This shows that an additional electric current J_{Sz} in (1) is generated only at high latitudes.

In case *S2* for SPE/GLE69 on January 20 2005 we study the variations of electric current J_z obtained by measurements of σ and E_z on the balloon station MINIS Flight 2 in the Antarctic stratosphere (*Kokorowski et al., 2006*) whose drift during that day is from (70.9°S, 10.9°W) at altitude z = 30.9 km to (71.4°S, 21.5°W) at z=33.2 km. The variations of J_z are demonstrated by (*Kokorowski et al., 2006,* their Fig.2d). J_z shows a similar, as in case *S1,* yet better expressed positive deviation from J_{FW}. This deviaiton begins 3.5 hours after the onset of SPE/GLE69 at 06:51 UT, and continues for about Δt = 4.5 hours. This deviation is characterized by $J_{z\max}$ ~ 6.5 pAm^{-2} – about three times bigger than J_z~1 - 2 pAm^{-2} measured before SPE. The average J_z during the deviation for 4.5 hours exceeds 3 pAm^{-2}. Such large increase of J_z cannot be supported by the inner electric generator of GEC only. We conclude that an additional electric source and related additional electric circuit superimposed to GEC are presented in cases *S1,2*.

In cases *G1* (15 April 2001) and *G2* (18 April 2001) measured have been the variations of the atmospheric electric field E_z at ground level in Apatity, Russia (Λ=63.3°) (*Shumilov et al., 2015*). Similar effect of peculiarly big and long-lasting increase of E_z takes place in each case. In case *G1* Δt ~ 45 minutes, $E_{z\max}$ ~ 600 V/m . In case *G2* Δt is more than three hours, $E_{z\max}$ ~ 550 V/m. $E_{z\max}$ is several times bigger than the typical value under fair-weather conditions (E_z < 200 Vm^{-1}). Again, cases *G1,2* demonstrate presence of an additional electric circuit superimposed to GEC during the respective SPE/GLE, similarly to *S1,2*.

Hypothetic mechanism of generation of electric current J_S during SPE/GLE

Here we consider shortly hypothetic processes *P1-3* in polar atmosphere and around during SPE/GLE which can cause generation of the electric current J_{Sz} in stratosphere and below at high latitudes – for more details see (*Tonev, 2022; Tonev and Asenovski, 2023*). Processes *P1-3* are subject of further elaboration in publications to follow.

P1. Injection of positive elementary charges into atmospheric regions R_p situated at high latitudes in each hemisphere together with the penetrating energetic protons. Hence, the proton flux into R_p regardless of their energy is of interest. The lower boundary z_0 of R_p is determined to be z_0~35 km – protons penetrating below z_0 (that is, of energies >~ 100 MeV) can be neglected related to the common flux. Region R_p is within geomagnetic latitudes $\Lambda > \Lambda_p$ where Λ_p is function of geomagnetic activity (*Rodger et al., 2006*). Λ_p=70° is a reasonable latitudinal boundary for quiet geomagnetic conditions. The injected charge is uncompensated positive charge in GEC and should be taken into account. We present an estimation of the total positive uncompensated electric charge Q_I injected into GEC in case *S2*, but only until 14:00 UT when geomagnetic activity is relatively low. By assumption that protons of energies >1 MeV penetrate into region R_p with Λ_p=70°, the total injected charge is at least 8×10^5 C – this is more than the total charge of 5×10^5 C generated by in GEC tropospheric sources (*Rycroft et al., 2008*). Hence, the uncompensated charge Q_{UC} injected into GEC during SPE/GLE should not be neglected.

A simplified representation of GEC during SPE is shown in Fig.1 as an equivalent electric circuit (EEC). The accumulation of uncompensated charge Q_{UC} in both polar regions R_p needs recovery of the impaired global charge balance in GEC by atmospheric electric current $\mathbf{J}_{HL}$ which usually flows from R_p to lower geomagnetic latitudes through the resistance r_{HL}. By non-diminished conductivity σ in the lower ionosphere (>~10^{-8} Sm^{-1}) the recovery of charge balance is actually immediate: within $<\sim 10^{-3}$ s. We show that SPE/GLE can cause modifications in GEC by redirection of current $\mathbf{J}_{\mathrm{HL}}$ as shown in Fig.1 by thick dashed lines.

P2. Hypothetic process of enforced production of aerosol particles (AP) in region R_{p} initiated by the increased ionization during SPE/GLE which eventually leads to decrease of conductivity σ in R_{p} (*Tonev, 2022*; *Tonev and Asenovski, 2023*). Process *P2* includes three simultaneous sub-processes, *P2G*, *P2M*, *P2T*.

P2G. Growth and multi-charging of existing aerosol particles (AP) driven by increased ionization in sub-regions of R_{P} with significant initial density S_0 of APs. Such can be the mesopause, or the upper stratosphere (*Tinsley and Zhou, 2006*). (*Rapp, 2000*) studies this sub-process in the mesosphere by representing any AP as a sphere with a radius r_{AP} and with k elementary electric charges ($k>0$ corresponds to positive charging of AP, and vice/versa). Growth of APs takes place by faster attachment of ions and neutral particles to APs than the loss processes. In the case of mesopause (*Rapp 2000*): 1) The attachment coefficient ν is increasing function of r_{AP} and $|k|$. 2) The mean number of charges $|k_{\mathrm{m}}|$ when $k_{\mathrm{m}}<0$ increases almost proportionally with r_{AP}. We obtain that the AP radius r_{AP} increases with time approximately as t^a where $a>1$ (a is close to 1). Actually, *P2G* is a positive feedback process of growth of APs by increasing of r_{AP} and $|k|$ (*Tonev, 2022*).

P2M. APs undergo multiplication due to segmentation of any AP into two or more separate smaller APs when critical pair of parameters (r_{AP}, k) is reached. As result, the density of APs S increases exponentially with time t: $S\sim S_0\exp(t/t_{\mathrm{S}})$ where t_{S} is the mean time needed by a new-born AP to fulfill the criteria of segmentation.

The result of processes *P2G* and *P2M* is a dramatic decrease of the life time of free electrons and ions to their attachment to APs. This leads to gradual, yet eventually dramatic depletion of electrons and ions, hence, to dramatic decrease of total conductivity σ_{p} in R_{p} (the charges are captured by APs whose mass is many orders of magnitude bigger than those of electrons and ions). The conductivity σ_{p} in R_{p} can become as low as 10^{-15} Sm^{-1}, or even less.

P2T. Transportation of APs from regions with large density S to ones with negligible S_0 before initiation of *P2G, P2M* by electric field $\mathbf{E}_{\mathrm{S}}$ (for multi-charged APs), and sedimentation.

P3. Redistribution of the electric charges injected into the atmosphere at high latitudes to lower latitudes by a superimposed electric current $\mathbf{J}_{\mathrm{HL}}$ in order to re global charge balance. The dramatic decrease of conductivity σ_{p} in region R_{p} by process *P2* during SPE leads to redirection of electric current $\mathbf{J}_{\mathrm{HL}}$ in GEC. Initially, $\mathbf{J}_{\mathrm{HL}}$ flows from high towards lower latitudes through resistance r_{HL} as shown in Fig.1 by thick solid arrow. With the increase of resistance r_{HL} determined by decrease of σ, later electric current $\mathbf{J}_{\mathrm{HL}}$ is redirected essentially into vertical current which flows towards the surface through columnar resistances r_{MH} (for altitudes $z>35$ km at high latitudes) and r_{TH} ($z<35$ km) (shown in Fig.1 by a vertical thick dashed arrow). The redirection of $\mathbf{J}_{\mathrm{HL}}$ is controlled by the increasing resistances r_{TH} and r_{MH}. The total columnar resistance at high latitudes $r_{\mathrm{CH}} = r_{\mathrm{TH}} + r_{\mathrm{MH}}$ is affected by the decrease of conductivity σ_{p} in region R_{p} only when $\sigma_{\mathrm{pmax}} <\sim 10^{-13}$ Sm^{-1}. In order to determine resistance r_{HL} the assumptions is used that the protons with energies >1 MeV penetrate into R_{p} at geomagnetic latitudes $\Lambda>\Lambda_{\mathrm{p}} = 70°$ (Rodger et al., 2006). Then

$$r_{\mathrm{HL}} > (1 - 2^{-1/2})R_{\mathrm{e}}\varphi_{\mathrm{p}}/\sigma_{\mathrm{pmax}} \sim 6\times10^{6}/\sigma_{\mathrm{pmax}}\ \Omega\mathrm{m}^2 \qquad (2)$$

Here $R_{\mathrm{e}}\sim 6.471\ 10^6$ m is the average earth's radius; $\varphi_{\mathrm{p}} = 0.5\pi(1 - \Lambda_{\mathrm{p}}/90°)$ is the geomagnetic co-latitude $90°-\Lambda_{\mathrm{p}}$ represented in radians; σ_{pmax} is the maximum conductivity in region R_{p}. Resistance r_{HL} becomes equal to r_{CL} when $\sigma_{\mathrm{pmax}} \sim 5\times10^{-11}$ S/m. If the following condition is fulfilled at time $t \geq t_{\mathrm{r}}$:

$$\sigma_{\mathrm{pmax}} <\sim 10^{-11}\ \mathrm{S/m}, \qquad (3)$$

actually the whole (>80%) electric current $\mathbf{J}_{\mathrm{HL}}$ will flow towards surface, and then through the earth to lower latitudes (shown in Fig.2 by horizontal thick dashed arrow). It is important to note that below ~35 km where process P2 is not active $\sigma <\sim 10^{-11}$ S/m by undisturbed conditions. The redirection of electric current $\mathbf{J}_{\mathrm{HL}}$ determines appearance of term $J_{\mathrm{S}z} \equiv J_{\mathrm{HL}z}$ in Eq.(1) in atmosphere below region R_{p}. Electric current $J_{\mathrm{S}z}$ in (1) depends by series of parameters and conditions; its model estimation is subject of future publications.

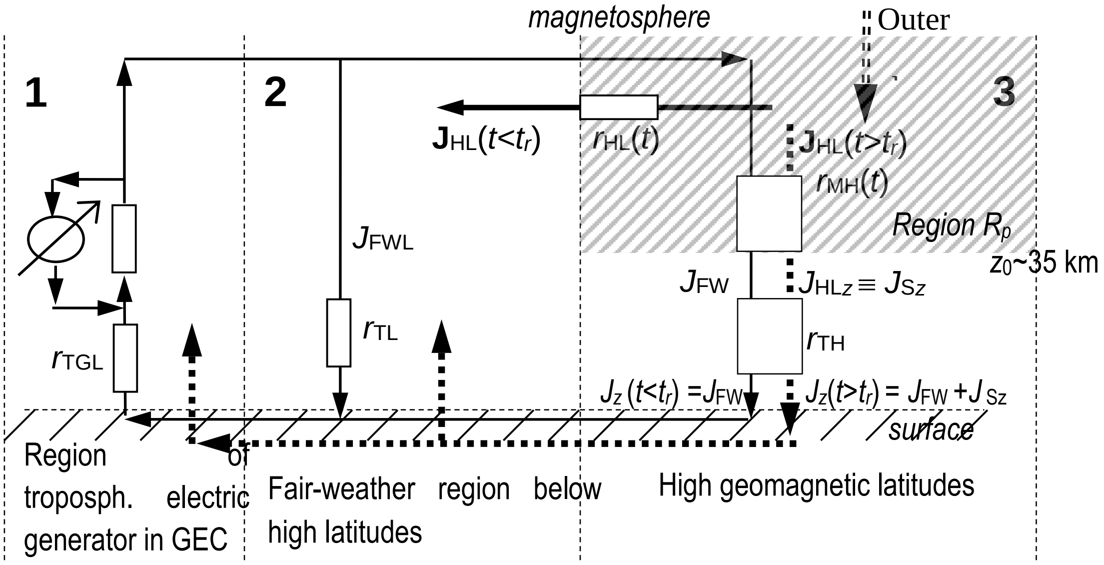

Figure 1*. Representation of GEC by an equivalent electric circuit during SPE/GLE. The dashed vertical lines determine regions 1, 2, 3: 1 is region of thunderstorm activity and electrified clouds (the electric source of GEC); 2 is region with fair-weather conditions below polar latitudes; 3 is region of polar geomagnetic latitudes with shaded segment* R_p *above* z_0*~35 km where uncompensated positive charges are injected (represented by double dashed arrow). The balance of charges in GEC is being recovered by electric current* J_{HL} *shown by horizontal thick arrow by* $t<t_r$*, and by dashed thick arrows at* $t>t_r$*. By* $t>t_r$ *current* $J_{Sz}=J_{HLz}$ *is added to* J_z *below* R_p*. Here* r_{T*} *represent columnar resistances of troposphere in regions 1-3.*

Confirmation by rocket-borne measurements during SPE/GLE from 19 October 1989

We analyze the profile of the vertical electric field E_z which have been measured at altitudes 24 - 70 km within a rocket experiment conducted at 19:31 UT on 21 October 1989 at geographic coordinates (58.5°S, 51.2°E) (*Zadorozhni et al., 1994; 1998*). This experiment is during the strong SPE/GLE on 19-22 October 1989; it is conducted 54.5 hours after the SPE onset. On 20-21 October this SPE/GLE was accompanied by a major geomagnetic storm with planetary geomagnetic index Kp=8 at the time of the rocket flight. Fig.2 (*Zadorozhni et al., 1994*) demonstrates the profile of the vertical electric field E_z (the solid curve) by convention that E_z>0 corresponds to downward electric field. The dashed curve shows the profile of the spatial charge density ρ computed from the profile of E_z by Gauss's law. The profile of ρ forms three main layers: L_{PL} [36-46 km] ($\rho > 0$); L_{N} [46-58 km] ($\rho < 0$); L_{PU} [58-64 km] ($\rho > 0$). By quasi-DC conditions conductivity σ in layers is estimated: in layer L_{N} σ is at least as low as ~10^{-15} S/m (*Tonev, 2022*). As far as we know, there is no satisfying explanation of the most striking feature - existence of negative layer L_{N} (*Zadorozhni et al., 1994*) until now.

The results in Fig.2 agree well with the hypothetic mechanism of generation of the additional current $\mathbf{J}_{\mathrm{S}}$ proposed above at time $t > t_{\mathrm{v}}$ when electric current $\mathbf{J}_{\mathrm{S}}$ is re-oriented vertically towards surface, represented by dashed line in Fig.2. This mechanism can explain the dramatic decrease of conductivity σ in mesosphere and in stratosphere observed at time t_{EXP} of rocket experiment (on a late phase of SPE, 54.5 hours after its onset).

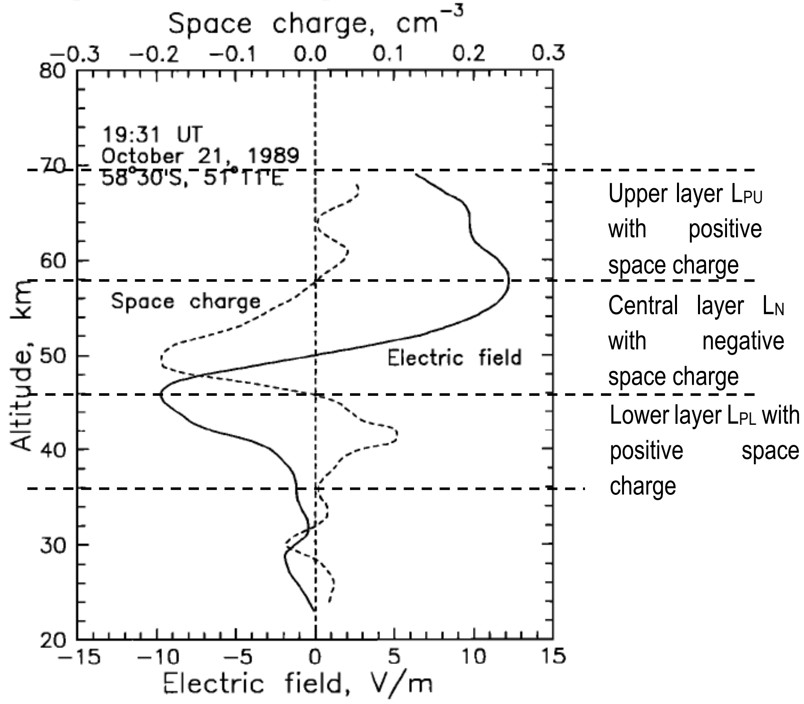

***Figure 2**. Rocket-borne profile (solid curve) of the vertical electric field E_z at (58.5°S, 51.2°E) obtained on October 21 1989 at 19:31 UT (Zadorozhni et al, 1994). The dashed curve shows the profile of the spatial charge density ρ.*

An explanation is given here of the creation of a negative layer L_N. During time a period well preceding t_{EXP} process *P2* causes a gradual decrease of conductivity σ in region R_p situated above z_0~35 km and at geomagnetic latitudes above Λ_p~60° corresponding to major geomagnetic storm with Kp=8 (*Rodger et al., 2006*). We accept that conductivity σ below ~35 km remains unaffected by process *P2*. The profile of spatial charge density ρ in Fig.3 (the dashed curve) shows that the maximum effect of process *P2* on conductivity σ is at altitude z_m=58 km where σ reaches its minimum $\sigma_{\min}$ in the modified conductivity profile. This determines negative conductivity gradient, $d\sigma/dz < 0$, in layer $L= [z_0=36 \text{ km}, z_m=58 \text{ km}]$, and accumulation of negative spatial charge by downward electric current $\mathbf{J}_{\mathrm{HL}}$. We accept that current $J_{\mathrm{S}z}$ is identical to its vertical component: $J_{\mathrm{S}z} \equiv J_{\mathrm{HL}z}$.

During accumulation of negative charge in layer L_N the following expression is valid:

$$|J_{\mathrm{HL}z}\,(z=z_0)| = |J_{\mathrm{HL}z}\,(z=z_m)| - dq_c(t)\,/dt > |J_{\mathrm{HL}z}\,(z=z_m)|, \tag{4}$$

since $dq_c(t)\,/dt < 0$. This demonstrates that at altitudes below z_0=35 km the electric current $J_{\mathrm{S}z}$, hence the total current J_z (1), have significant increase during the formation of layer L_N, if the formation of layer L_N follows that of L_{PU}. The result is redirection of $\mathbf{J}_{\mathrm{HL}}$ into downward electric current $J_{\mathrm{S}z}=J_{\mathrm{HL}z}$ at time t_v which leads to enhancement of current J_z by addition of term $J_{\mathrm{S}z}$ in (1) at altitudes $z<z_0$=35 km and amplification of $J_{\mathrm{S}z}$ according to (4). This gives an explanation of the peculiar enhancement of the electric current J_z and field E_z in each of cases *S1,2, G1,2* considered here. These are not transient variations since their duration is much larger than the relaxation time of GEC ~500 s (*Rycoft et al., 2008*).

The explanation proposed here concerns the peculiarity in the variations of electric characteristics discussed above, as well as the creation of the layer L_N with negative spatial charge in Fig.3 (*Zadorozhni et al., 1994*). The time of accumulation of spatial charge in layer

L_N is much before the rocket launch at t_{EXP}. Similarly, the formation of the upper positive layer L_{PU} is explained by the downward current J_{HLz} along decreasing conductivity σ which is the case in Fig.3 above altitude z_m=58 km. Possibly, the lower positive layer L_{PL} is created after layers L_{PU}, L_N as result of gradual degradation of layer L_N well after time t_r.

Conclusions

- An additional electric circuit is created in GEC during four considered SPE/GLE with significant vertical component in middle stratosphere, and at surface, at high latitudes.
- For explanation of this peculiarity a hypothetic mechanism is proposed which is consistent with the peculiar experimental rocket-borne data of the profile of electric field E_z on high geomagnetic latitude during SPE/GLE October 19 1989.

References:

Holzworth, R.H., K. W. Norville, P. R. Williamson (1987). Solar flare perturbations in stratospheric current systems, Geophys. Res. Lett., 14 (8), 852-855.

Kokorowski, M., Sample, J.G., et al. (2006). Rapid fluctuations of stratospheric electric field following a solar energetic particle event, Geophys. Res. Lett., 33, L20105.

Mironova, I.A., A.L. Aplin, et al. (2015). Energetic Particle Influence on the Earth's Atmosphere, Space. Sci. Rev., Springer doi 10.1007/s11214-015-0185-4
https://www.researchgate.net/publication/283291945

Rapp, M. (2000). Capture rates of electrons and positive ions by mesospheric aerosol particles, J. Aerosol Sci. Vol. 31 (2000), 11, pp. 1367-1369.

Rycroft, M., Harrison, R.G., Nicoll, K.A., Mareev, E.A. (2008). An Overview of Earth's Global Electric Circuit and Atmospheric Conductivity, Space Sci. Rev. (2008) 137: 83–105, doi: 10.1007/s11214-008-9368-6

Rodger, C.J., Clilverd, M.A., Verronen, P.V., Ulich T., Jarvis, M.J., and Turunen, E. (2006). Dynamic geomagnetic rigidity cutoff variations during a solar proton event, J.Geophys.Res., 111, A04222, doi:10.1029/2005JA011395, 2006.

Shumilov O.I., Kasatkina E.A., A. V. Frank-Kamenetsky (2015). Effects of Extraordinary Solar Cosmic Ray Events on Variations in the Atmospheric Electric Field at High Latitudes, Geomag. Aeron., 2015, 55, 666–674, doi: 10.1134/S0016793215050151.

Tinsley, B.A., L. Zhou (2006). Initial results of a global circuit model with variable stratospheric and tropospheric aerosols, J. Geophys. Res., 111, D16205, doi:10.1029/2005JD006988

Tonev, P.T. (2022). Peculiar atmospheric electric field response at high latitude to three major SEP events in 2001 and possible interpretation, Proc. 14-th Workshop "Solar Influences on the Magnetosphere, Ionosphere and Atmosphere" Primorsko, Bulgaria, 6-10 June, 2022.

Tonev P., Asenovski, S. (2023). Hypothetic atmospheric response to SEP explaining peculiar electric fields and currents at high latitudes, Proc. 15-th Workshop "Solar Influences on the Magnetosphere, Ionosphere and Atmosphere" Primorsko, Bulgaria, June, 2023.

Zadorozhni, A.M., A.A. Tyutin (1998). Effects of geomagnetic activity on the mesospheric electric fields, Ann. Geophysicae 16 (1998), 1544-1551.

Zadorozhni, A.M., V.N. Kikhtenko, et al. (1994). Middle atmosphere response to the solar proton events of October 1989 using the results of rocket measurements, J. Geophys. Res., 99, n. D10, pp. 21,059-21,069, 1994.

Proceedings of
the Sixteenth Workshop “Solar Influences on the Magnetosphere, Ionosphere and Atmosphere”
June, 2024

Comparative Analysis of Solar Activity Influences on Trajectories of Extratropical Cyclones in Different Regions of the North Atlantic

Veretenenko S.V., Dmitriev P.B.

Ioffe Institute, Russian Academy of Sciences; s.veretenenko@mail.ioffe.ru

Abstract

Influences of solar activity on the latitudinal position of the main trajectories (storm tracks) of extratropical cyclones were compared in different regions of the North Atlantic: 1) the western North Atlantic (60–40°W), which is a region of intensive cyclone formation and deepening; 2) the Icelandic Low region (30–10°W), where cyclones usually reach their maximum development and their occurrence is maximal; 3) the eastern North Atlantic (0–20°E), where processes of cyclone filling become dominating. It was found that secular oscillations (with periods ~80–90 years) of storm track latitudes, which may be associated with the solar Gleissberg cycle, strongly dominate in the western North Atlantic. These oscillations weaken in the Icelandic Low region and disappear to the east of Greenwich (0–20°E), where multidecadal oscillations (with periods ~60 years) were detected. On the bidecadal time scale, oscillations of storm track latitudes, with periods close to the Sun’s magnetic Hale cycle, were found in all the studied regions of the North Atlantic. Storm tracks noticeably shift to the north in even solar cycles (according to the Zurich numbering) and slightly to the south in odd ones. The 22-year oscillations are most pronounced in the Icelandic Low region and weaken sharply east of Greenwich. The obtained results show that the region of the Icelandic Low seems to be most sensitive to solar activity influences.

Keywords: *solar activity; cyclone trajectories; Icelandic Low.*

Introduction

Extratropical cyclonic activity is known to be an important factor influencing weather and climate at middle latitudes. Deep cyclones coming from the North Atlantic cause many extreme weather events and natural disasters in Europe (hurricane winds, heavy rainfall, floods etc.) So, studying solar activity influences on the development and movement of extratropical cyclones is of significant practical importance, as it helps us to improve the quality of weather and climate forecasts.

In a number of studies, it was shown that cyclonic activity is influenced by solar activity related phenomena, such as solar flares [Schuurmans and Oort, 1969], solar and galactic cosmic ray variations [Veretenenko and Thejll, 2004; Artamonova and Veretenenko, 2011], sector boundaries of interplanetary magnetic field [Wilcox et al., 1974] etc. In the works [Brown and John, 1979; Tinsley, 1988], variations of cyclone trajectories in the 11-year solar cycle were studied. It was found that storm track latitudes in the eastern North Atlantic are lower at maxima of the solar cycle than at minima. A similar storm track variation was detected on a secular time scale in the North Atlantic west of the Greenwich meridian [Veretenenko et al., 2023]. The aim of this work is to study in more detail and compare the manifestations of solar activity influence on cyclone trajectories in three regions of the North Atlantic, including the area lying east of Greenwich.

Experimental data and their analysis

Formation of North Atlantic cyclones usually takes place near the eastern coast of North America, where in the cold half of the year high temperature contrasts and a favorable structure of the thermobaric field are observed. The subsequent movement of cyclones goes, as a rule, northeast through Iceland to the Barents Sea, which results in the formation of an extended low-pressure area (baric trough) on monthly maps of sea level pressure. The axis of the trough (the central line connecting pressure minima) indicates the direction of the predominant movement of cyclones (storm track). So, we determined latitudes of pressure minima at longitudes from 60ºW to 20ºE for the cold months (October-March), which is a period of intense extratropical cyclogenesis. The gridded monthly data from the MSLP (Mean Sea Level Pressure) archives of the Climatic Research Unit (https://crudata.uea.ac.uk/) for 1873–1978 and NCEP/DOE AMIP-II Reanalysis (https://psl.noaa.gov/) for 1979–2021 were used as the experimental base. The obtained latitudes of storm tracks were averaged over three regions: 1) the western North Atlantic (60–40°W), which is a region of intensive cyclone formation and deepening; 2) the Icelandic Low region (30–10°W), where cyclones usually reach their maximum development and their occurrence is maximal; 3) the eastern North Atlantic (0–20°E), where processes of cyclone filling become dominating.

Figure 1 presents the temporal variations of average latitudes of storm tracks in the cold half of the year in different regions of the North Atlantic, as well as their spectral characteristics obtained using the method of a sampling estimate of the normalized spectral density [Jenkins and Watts, 1968].

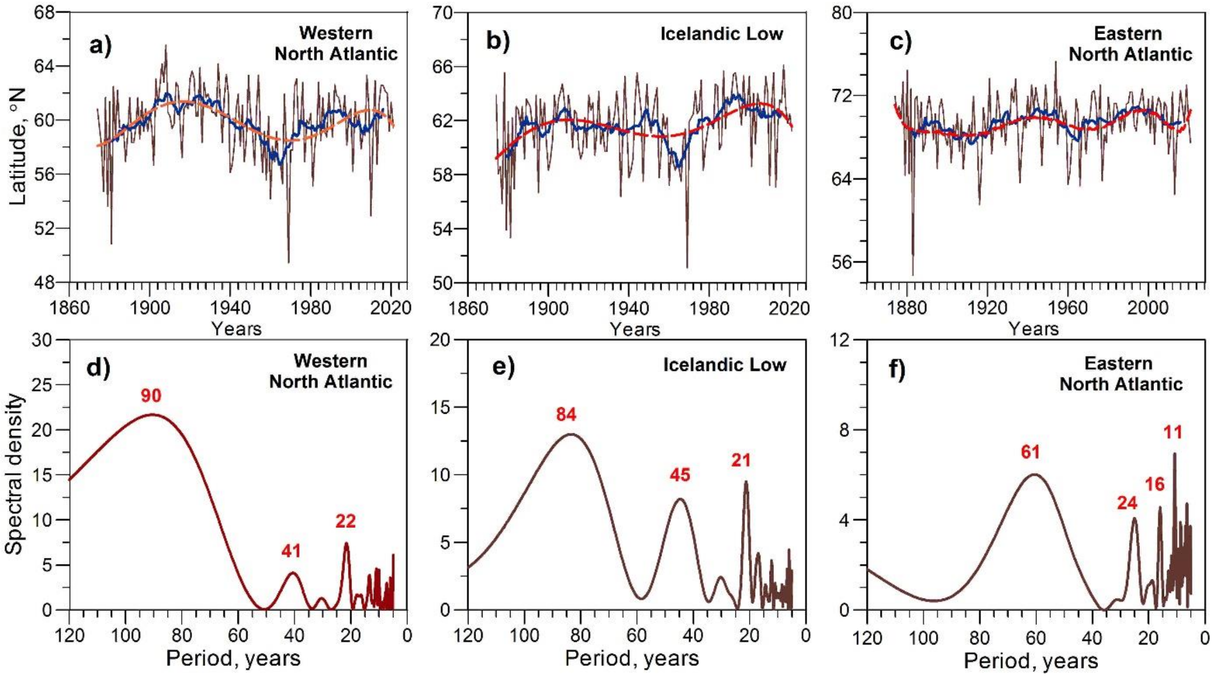

Figure 1. *Top: Temporal variations of average storm track latitudes in the cold months (October-March) in different regions of the North Atlantic. Thick blue lines and dashed red lines show 11-year running averages and the 5th order polynomial approximation, respectively. Bottom: Sampling estimates of the normalized spectral density of storm track latitudes in different regions of the North Atlantic.*

One can see that latitudes of storm tracks in the North Atlantic reveal secular (~80–90 years), multidecadal (~40–45 and ~60 years) and bidecadal (~21–24 years) oscillations which may be associated with solar activity. To assess the amplitudes of the detected oscillations, we carried out an approximation of the studied storm track latitudes by the polyharmonic model [Serebrennikov and Pervozvansky, 1965], which included the main quasi-periods. The initial signal $X(t)$ (storm track latitudes in a given region at time t) was assumed to consist of polyharmonic and noise components:

$$X(t) = A_0 + \sum\nolimits_{k=1}^{\nu} R_k \cos\left(\frac{2\pi t}{T_k} - \varphi_k\right) + n(t),$$

where A_0 is a constant, R_k is the amplitude, ν and Tk (k =1, 2, 3, …) are the number and the value of quasi-periods, respectively, n(t) is a stationary random process ("white noise"). The polyharmonic model for each region included the periods indicated in Figure 1 (bottom panels). The results of the estimates are presented in Figure 2.

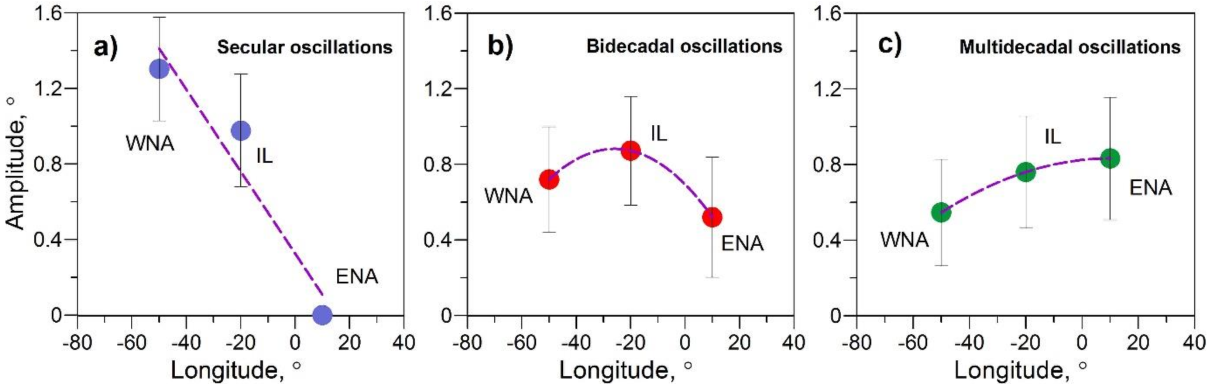

Figure 2. *Amplitudes of secular (a), bidecadal (b) and multidecadal (c) oscillations of storm track latitudes in the western North Atlantic (WNA), the Icelandic Low (IL) and the North Atlantic east of Greenwich (ENA). Thick dashed lines show the linear (a) and the 2nd order polynomial (b, c) approximation. The vertical bars show 2 standard deviations.*

The data in Figure 2 show that secular oscillations in storm track latitudes strongly dominate in the western North Atlantic, where cyclogenetic processes are most intensive. The amplitude of the secular oscillations is ~1.3° in this region and then it decreases to ~1° in the Icelandic Low, where bidecadal and multidecadal oscillations intensify. Secular oscillations disappear completely east of Greenwich. Bidecadal oscillations are a characteristic feature of storm tracks throughout the North Atlantic (Figure 1, bottom panels). They reach the highest amplitude (~0.9°) in the Icelandic Low, where the cyclone occurrence is maximal, and weaken noticeably, with the amplitude decreasing to ~0.5°, in the area east of Greenwich, where cyclone filling (destruction) predominates. One can note that east of Greenwich, oscillations in storm track latitudes differ significantly from those observed west of Greenwich. In this area, secular oscillations disappear and multidecadal oscillations with periods of ~60 years become dominating. Bidecadal oscillations weaken compared with those west of Greenwich and oscillations with shorter periods of ~11 and 16 years become stronger than bidecadal ones. Thus, we can note the attenuation of long-term variations in latitudes of cyclone trajectories and the intensification of short-term ones when cyclones move from the west to the east. The amplitudes of oscillations in storm track latitudes estimated on the base of the polyharmonic model are summarized in Table 1.

Table 1. *Amplitudes of oscillations in storm track latitudes in different regions of the North Atlantic*

Region	**Time scale**			
	Secular	**Multidecadal**	**Bidecadal**	**Decadal**
Western North Atlantic	1.3°	0.55° (41 yrs)	0.72°	–
Icelandic Low	0.98°	0.76° (45 yrs)	0.88°	–
Eastern North Atlantic	–	0.83° (61 yrs)	0.52	0.66° (11 yrs) 0.63 (16 yrs)

Let us consider in more detail bidecadal oscillations in latitudes of the main cyclone trajectories, which are observed throughout the North Atlantic. Figure 3 (top panels) presents the results of an additional spectral analysis of high-frequency components (HFCs) of the studied time series, which allows us to eliminate low-frequency components and to check up the stability of the detected quasi-periods on the periodogram. The HFCs were calculated using the Blackman-Tukey high-frequency filter with different "cut-off" frequencies (periods) $T_{\text{cut-off}}$. The data in Figure 3 demonstrates stable maxima of spectral density at periods of ~22-25 years, which confirms the reliability of bidecadal oscillations in storm track latitudes in all the studied regions.

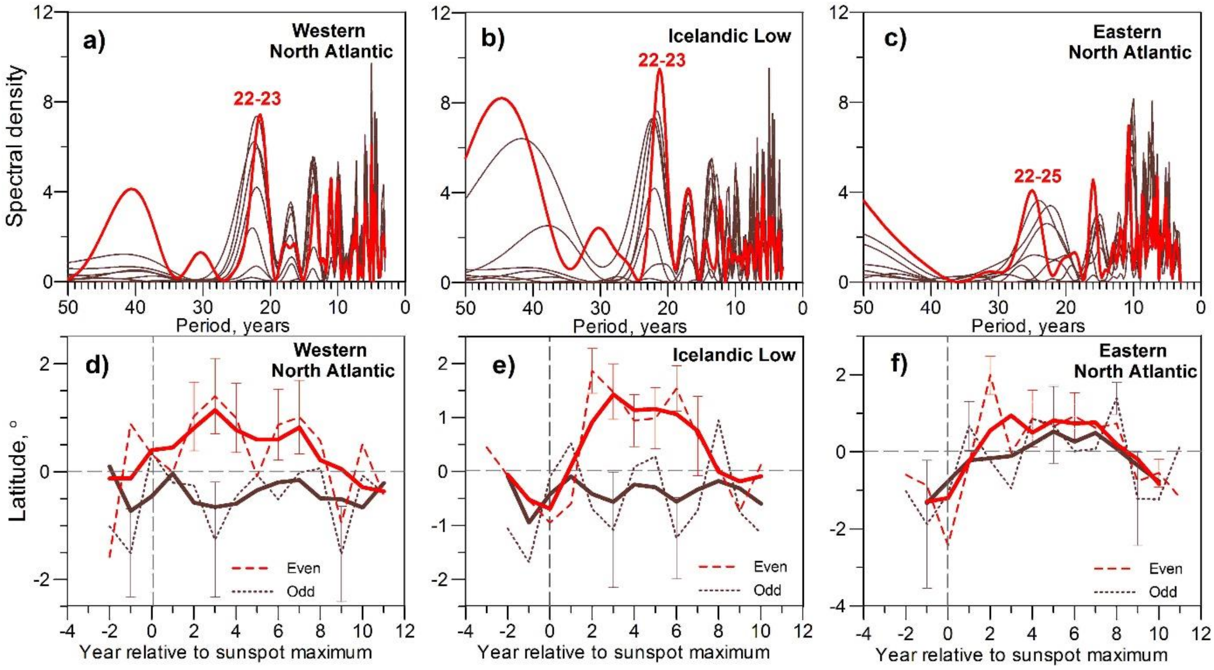

Figure 3. *Top: Sampling estimates of the normalized spectral density of average storm track latitudes in the cold months (October-March) in different regions of the North Atlantic for the initial time series (thick red lines) and their high frequency components with "cut-off" parameter $T_{cut\text{-}off}$ =7, 11, 17, 23, 29, 37 and 43 years (thin brown lines). Bottom: Mean (SPEA) variations of storm track latitudes in 7 even (red dashed lines) and 6 odd (brown dotted lines) solar cycles. Thick lines show 3-year running averages. The vertical bars show two standard errors of the mean.*

The detected bidecadal variations in latitudes of storm tracks are close to the Hale magnetic cycle observed in the polarity of magnetic fields on the Sun. The Hale cycle consists of two consecutive 11-year cycles. At the beginning of each 11-year cycle, the polarity distribution in sunspot groups reverses, whereas near the sunspot maximum, the reversal of the overall magnetic field of the Sun occurs. The Hale cycle is believed to start from an even (according to the Zurich numbering) cycle (e.g., [Nagovitsyn et al., 2009]). Figure 3 (bottom panels) shows the results of the superposed epoch analysis (SPEA) of variations in storm track latitudes (obtained by subtracting a secular variation) for even (12th to 24th) and odd (13th to 23rd) cycles. The year of the sunspot maximum (the overall magnetic field reversal) is taken as a zero year. One can see that, during the declining phase and the minimum of even solar cycles, a noticeable shift of cyclone trajectories to the north (relative to a secular variation) takes place, whereas during the declining phase and the minimum of odd cycles, only an insignificant southward shift is observed. The difference between storm track variations in even and odd cycles is maximal in the Icelandic Low region, where bidecadal oscillations are most pronounced compared with other regions of the North Atlantic (Figure 3b). In the Icelandic Low region, the northward shift reaches ~1–2° from the second to the sixth years after the solar maximum, with the confidence level amounting 0.96–0.98 according to the estimates using the Monte-Carlo method. East of Greenwich, the difference between storm track variations in even and odd solar cycles decreases markedly, so bidecadal oscillations in cyclone trajectories become less pronounced (Figure 3c).

Thus, the above results show that bidecadal oscillations in cyclone trajectories are due to a noticeable northward shift in even solar cycles and a weak southward shift in odd ones. These oscillations are strongest in the Icelandic Low region, which is a particular region of the North Atlantic. It is characterized by the highest occurrence of cyclones, which arrive in this region having reached the stage of their maximum development. However, high temperature contrasts between the icy surface of Greenland and the warmer ocean contribute to cyclone re-deepening (regeneration). In this region, the intensification of cyclone re-deepening was detected in association with energetic Solar Proton Events [Veretenenko and Thejll, 2004]. All this allows suggesting that the Icelandic Low is the most sensitive region to solar activity influences.

As cyclone movement is influenced by the intensity of the stratospheric polar vortex, one can suggest that solar activity influences on cyclone trajectories are realized via variations of the vortex intensity. Cyclone trajectories shift poleward under a strong vortex and equatorward under a weak one [Kidston et al., 2015]. Thus, the detected oscillations in storm track latitudes suggest the corresponding oscillations in the vortex strength. Figure 4 shows the dependence of storm track latitudes in the Icelandic Low region on maximal values of zonal wind velocity in the stratosphere over the North Atlantic. One can see that an increase of zonal wind velocity contributes to the northward shift of cyclone trajectories, the highest correlation being observed between storm track latitudes and wind velocity at the stratospheric levels 70 and 50 hPa (~18–20 km), which is a region of maximal ionization by galactic cosmic rays (GCRs) [Bazilevskaya et al., 2000].

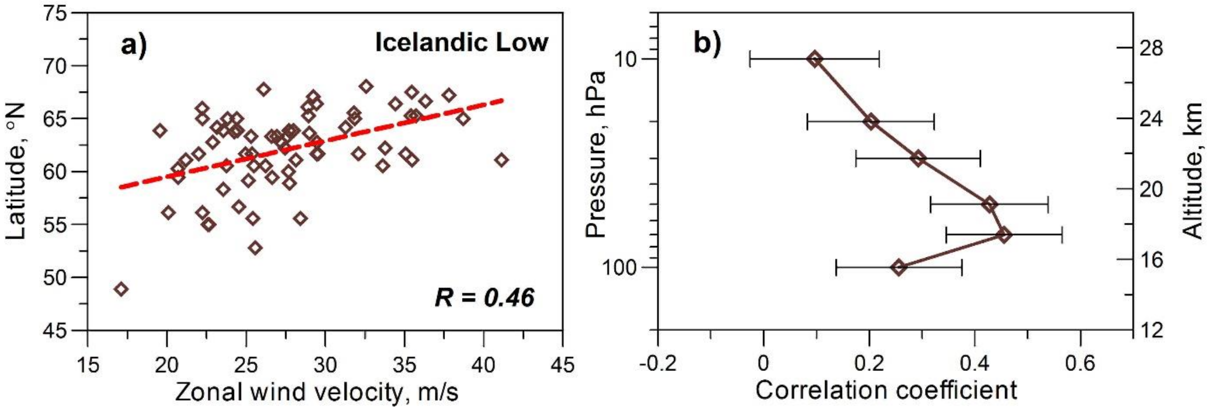

Figure 4. *a) Average storm track latitudes in the Icelandic Low in the winter months (December-January) versus maximal values of zonal wind velocity at the level 70 hPa over the North Atlantic; b) correlation coefficients between storm track latitudes in the Icelandic Low in winter and maximal zonal wind velocity over the North Atlantic at different stratospheric levels. The horizontal bars show two standard errors of the correlation coefficient.*

Thus, the shift of cyclone trajectories to the north provides evidence for intensification of the stratospheric polar vortex, whereas the southward shift indicates the vortex weakening. A possible reason for the northward shift is the influence of increases in ionization rate due to GCRs on the vortex intensity. The data in [Veretenenko et al., 2023] showed that the northward shift of storm tracks both on the secular and bidecadal time scales takes place under an enhanced intensity of galactic cosmic rays. On a secular time scale, storm tracks were shifted northward when GCR intensity (characterized by the concentration of the cosmogenic isotope ^{10}Be in polar ice) reached maximal values at the minimum of the Gleissberg cycle. On a bidecadal time scale, the northward shift is observed during the declining phase of even cycles when GCR fluxes are enhanced compared with those in odd ones. This allows suggesting that the northward shift of cyclone trajectories is caused by the polar vortex intensification due to GCR flux increases.

A mechanism of the polar vortex intensification under ionization increases may involve changes in the temperature regime of the polar middle atmosphere resulting from changes in its chemical composition (ozone depletion due to enhanced production of odd hydrogen HO_x ($H+OH+HO_2$) and odd nitrogen NO_x ($N+NO+NO_2$) families, which catalytically destroy ozone. Under polar night conditions, ozone acts as a greenhouse gas, absorbing the outgoing long-wave radiation of the Earth and the atmosphere. So, ozone destruction may contribute to a cooling of the polar middle atmosphere, which, in turn, may result in the increase of temperature contrasts between middle and high latitudes and the polar vortex intensification.

Conclusions

Latitudinal position of the main directions of cyclone movement (storm tracks) reveals variations, which may be associated with solar activity, in all the studied regions of the North Atlantic. Secular oscillations in storm track latitudes close to the solar Gleissberg cycle are most pronounced in the areas west of Greenwich where cyclones usually arise and develop most intensively. In the area east of Greenwich, where processes of cyclone destruction are more frequent, secular oscillations disappear and multidecadal ones become dominating. Bidecadal oscillations in storm track latitudes close to the magnetic Hale cycle are due to a noticeable northward shift of cyclone trajectories during the declining phase of even solar cycles. These oscillations are observed throughout the North Atlantic, but they are most expressed in the Icelandic Low area. East of Greenwich, bidecadal oscillations weaken sharply, but those with shorter periods intensify. The obtained results suggest that the Icelandic Low area, which is characterized by the highest occurrence of cyclones in the North Atlantic, is most sensitive to solar activity influences.

References

Artamonova, I., Veretenenko, S. (2011). Galactic cosmic ray variation influence on baric system dynamics at middle latitudes, J. Atmos. Solar-Terr. Phys., Vol. 73, pp. 366-370, DOI: 10.1016/j.jastp.2010.05.004

Bazilevskaya, G.A., Krainev, M.B., Makhmutov, V.S. (2000). Effects of cosmic rays on the Earth's environment, J. Atm. Sol.-Terr. Phys., Vol. 62, pp. 1577-1586.

Brown, G.M., John, J.I. (1979). Solar cycle influences on tropospheric circulation, J. Atmos. Terr. Phys., Vol. 41, pp. 43-52.

Jenkins, G., Watts, D. (1968). Spectral Analysis and Its Application; Holden-Day: San Francisco, CA, USA.

Kidston, J., Scaife, A.A., Hardiman, S.C. et al. (2015). Stratospheric influence on tropospheric jet streams, storm tracks and surface weather, Nature Geoscience, Vol. 8, No 6, pp. 433-440, DOI: 10.1038/ngeo2424.

Nagovitsyn, Yu.A., Nagovitsyna, E.Yu., Makarova, V.V. (2009). The Gnevyshev–Ohl rule for physical parameters of the solar magnetic field: The 400-year interval, Astron. Lett., Vol. 35, No 8, pp.564-571.

Schuurmans, C.J.E., Oort, A.H. (1969). A statistical study of pressure changes in the troposphere and lower stratosphere after strong solar flares, Pure Appl. Geophys., Vol. 75, pp. 233-246.

Serebrennikov, M. G., Pervozvansky, A.A. (1965). Hidden periodicity determination; Nauka, Moscow.

Tinsley, B.A. (1988). The solar cycle and the QBO influences on the latitude of storm tracks in the North Atlantic, Geophys. Res. Lett., Vol. 15, No 5, pp. 409-412.

Veretenenko, S.V., Dmitriev, P.B., Dergachev, V.A. (2023). Long-Term Changes in Main Trajectories of Extratropical Cyclones in the North Atlantic and Their Possible Association with Solar Activity, Geomagn. Aeron., V. 63, No 7, pp. 953-965, DOI: 10.1134/S0016793223070265.

Veretenenko, S., Thejll, P. (2004). Effects of energetic solar proton events on the cyclone development in the North Atlantic, J. Atm. Sol.-Terr. Phys., Vol. 66, No 5, pp. 393-405.

Wilcox, J.M., Scherre,r P.H., Svalgaard, L., et al. (1974). Influence of solar magnetic sector structure on terrestrial atmospheric vorticity, J. Atm. Sci. Vol. 31, No 2, pp. 581-588.

Proceedings of
the Sixteenth Workshop “Solar Influences on the Magnetosphere, Ionosphere and Atmosphere”
June, 2024

Potential Candidates for Cut-off Dense Plasma Modeling

Sakan N.M.[1], *Simić Z.*[2], *Srećković V.A.*[1], *and Dechev M.*[3]

[1]University of Belgrade, Institute of Physics Belgrade, PO Box 57, 11001 Belgrade, Serbia;
nsakan@ipb.ac.rs
[2]Astronomical Observatory, Volgina 7, 11060 Belgrade, Serbia;
[3]Institute of Astronomy and National Astronomical Observatory, Bulgarian Academy of Sciences, 72,
Tsarigradsko chaussee Blvd. Sofia, Bulgaria;

Abstract

The modeling of plasma behavior from mid up to strong non-ideality, e.g. plasma with a dominant Coulomb interaction is of interest. The micro field is strongly dependent on a form of used pseudo-potential. It is important to have in mind that the plasma behavior is considered as a variation to the main form of a potential. It was obvious from previous papers that the pseudo-potentials used in solid state physics, e.g. ab-initio ones, could be used successfully in describing of a dense plasma. Here we present the candidates potentials calculated with ab-initio method that should be analyzed in order to be used for describing a dense plasma. As a result, after studying of the potentials, it is expected to have a method of introducing a more complex atoms and ions in existing plasma model.

Keywords: astrophysical plasma modeling; dense plasma; optical properties.

Introduction

In the dense plasma the inter-particle Coulomb interaction becomes dominant over the thermal kinetic energy (Fortov et al. 2006). In such conditions a coupled system of particles behaves partially like a crystal. The simplified version, for hydrogen case, of non-ideality parameter **Γ** is given by:

$$\Gamma = \frac{E_p}{E_k} = \frac{e^2}{kTr_{WS}} \sim e^2 N_e^{1/3} \beta \qquad (1)$$

Where $\beta = 1/(kT)$, and r_{WS} is a Wiegner Seits radius given by:

$$r_{WS} = \left(\frac{3}{4\pi N_e}\right)^{1/3}$$

The plasma interaction, cut-off Coulomb potential, was used successfully previously for describing of dense plasma in Vitel Y. (2004), and for more details see later papers for example Dimitrijević, et al (2018), Srećković, et al. (2018), Mihajlov, et al. (2015), Ignjatović, et al. (2009). Although the expected plasma influence should be governed in the far field concerning a ionic core radius, it is expected to have a strong influence of the form of a ab-initio yielded pseudopotential. The area of interest in Hydrogen model is in range of 0.1 < Γ < 1.5, while for other species the thourough investigation of model behavior is needed.

Pseudopotentials, link between the dense plasma and condensed matter

The describing plasma depends of two parts, the atom/ion content, as well as plasma influence. While the plasma influence is described as a collective phenomenon, the atom and ion influence is described with the help of pseudo-potential. The idea of describing a complex atom dense plasma as well as describing of complex atom mixtures plasma arises. The atom and ion influence should be described by the ionic core of the adequate complex atom and ion, while the plasma influence is described with the collective phenomena modeling

There are several ab-initio calculations that are potential candidates for generating a pseudo-potentials capable for being used in dense plasma modeling. Our choice was ATOM, the program originally written by Sverre Froyen at the University of California at Berkeley, and now maintained by Alberto Garcia, see Soler et al. (2002).

It is expected that this approach could enable an inclusion of more complex atom and ion plasma models. A first step the comparison of exact model for Hydrogen with previously used Opium code generated one as well as ATOM generated should be carried out.

Results

The investigation of usability of ab-initio calculated pseudo-potentials is still work in progress. Two ab-initio programs were used in the presented topic, Opium, pseudo potential generation code, and the mentioned ATOM. The simplicity of inclusion ions as well as maturity of the code is leading towards ATOM. At this moment a intensive check of the ability of using ab-initio generated pseudo-potentials is a work in progress. Since now, the Opium generated ones are in focus.

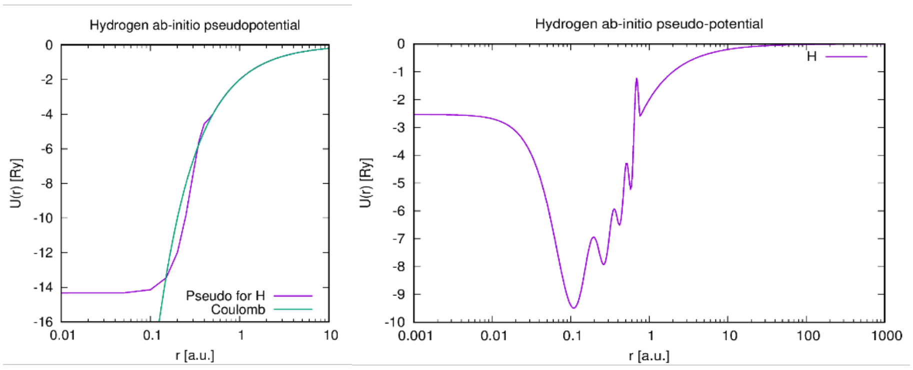

Figure 1. *Comparison of hydrogen pseudo-potential generated with ATOM code, left side figure, with opium generated one, on the right.*

As it could be seen from the Figure 1. the two different forms of the pseudo-potential yields a entirely good solution for the bond states for hydrogen atom. All bind energies are well within expected 0.1% error, that was expected with the solving procedure. Similarly, on Figure 2. a set of pseudo-potentials for He are given.

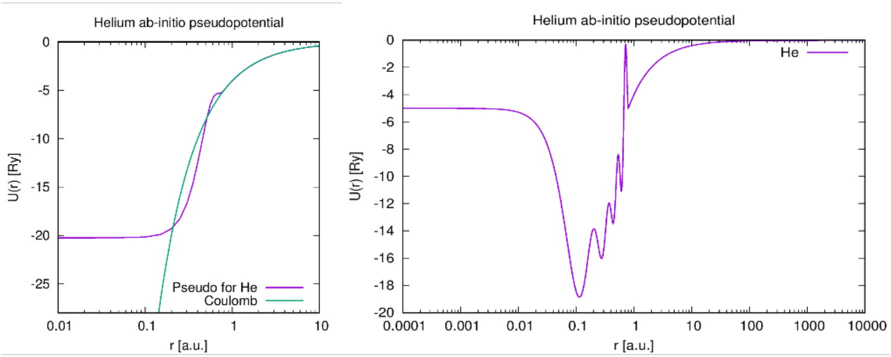

Figure 2. *Comparison of He pseudo-potential generated with ATOM code, left side figure, with opium generated one, on the right.*

The form of pseudo-potentials generated by the opium code for both hydrogen as well as helium is similar in form, but complex. It led to the conclusion that much more precaution should be taken before promoting final results. The experience in both varying parameters of the initial guess fir the levels as well as a form of ab-initio potentials is needed.

The next step is the simulation of the influence of ionic component in plasma, one of the collective plasma effect. It is simulated by the means of dense packing model. The ions are considered motionless, and their inter-ionic distance is exact Wiegner-Seits one. The screening is modeled as Debye one, although the model is not applicable to dense plasma the results are good enough, the work on better screening model is in progress. This step is step further in comparison to previous work. In this step a electron density and electron temperature are converted to inter-ionic distance, e.g. the Wiegner-Seitz radius. Based on those facts a averaged potential of emmiter is calculated.

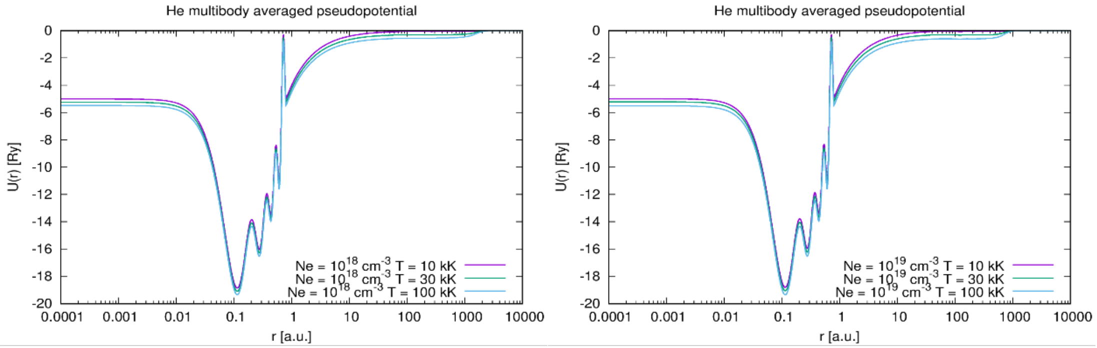

Figure 3. *The generation of cut-off platou as a consequence of multiple coupled ionic fields in plasma, left figure Ne = 10^{18} cm^{-3}, right Ne=10^{19} cm^{-3}, various temperatures*.

From Figure 3. it could be seen that the cut-off radius, that exists as the consequence of the mean plasma interaction is generated by the means of simple model. Also the other effect of additional lowering of the bound energy could be observed as a lowering of potential well, especially in a area of small radii. Previously this effect was a parameter in model, and now it is expected to have not only physical meaning but also a model for it’s estimating.

It is obvious that there is a need for further describing of inclusion of more precise screening model as well as modeling of the influence of the thermal energies of each of plasma components. The presented potentials are solvable by the means of numerical integration of Schrodinger equation. Since a work on test procedure for the final results is also a work in progress it is expected to have the data on dipole matrix elements as well as oscillator strengths for complex emitters in dense plasma presented in near future.

Conclusion

From presented results it is obvious that the proposed method of inclusion of complex atoms and ions in plasma could lead to a usable model potential. The benefits of proposed model in contrast to the more widely used, molecular dynamics coupled with the exact Schrodinger solver, is a computing power relaxed calculations that are applicable on any desktop system and could be used as such. After this test of the code the inclusion of bond-free and free-free transitions should take place.

A describing of broadening mechanisms for described plasma are still needed, and it is expected to be a one of the further steps. After all the presented research shows that the simplified approach could lead to good, applicable results for both experimental as well as stellar/Solar plasma in areas of moderate as well as relatively high densities. The automatic generation of mean plasma influence as a mean of multi-body averaged potential gives an idea of introducing more complex models of influence of separate plasma components

The test and inclusion of model for helium, that is a first step in progress, could lead to a better modeling of a Solar and stellar dense plasmas.

It is expected that in further work an method for describing a plasma in initial LIBS breakdown of complex targets and mixtures could help with better understanding of laboratory plasma as well as diagnostic one, like in NOVA2LIBS4fusion project.

Acknowledgment

This research was supported by the Ministry of Science, Technological Development and Innovation of the Republic of Serbia (MSTDIRS) through contract no. 451-03-66/2024 03/200002 made with Astronomical Observatory (Belgrade), 451-03-47/2023-01/200024 made with Institute of physics, NOVA2LIBS4fusion Grant no. 3108/2021 and with the financial support from the Bulgarian Academy of Sciences (Bilateral grant agreement between BAS and Astronomical Observatory, Belgrade), that is gratefully acknowledged.

References

Vitel Y.: 2004., J. Quant. Spectrosc. Radiat. Transf., 83, (3-4):387–405.

Chabrier G., SaumonD., and Potekhin A. Y.: 2006., J. Phys. A, 39(17):4411–4419.

Fortov V., Iakubov I., and Khrapak A: 2006., Physics of Strongly Coupled Plasma, International Series of Monographs on Physics. OUP Oxford.

Dimitrijević M. S., Srećković V. A., Sakan N. M., Bezuglov N. N., and Klyucharev A. N.: 2018., Geomagn. Aeron., 58(8):1067–1072.

Srećković V A, Sakan N, Šulić D, Jevremović D, Ignjatović Lj M, and Dimitrijević M S: 2018., Mon. Not. R. Astron. Soc., 475(1):1131–1136.

Mihajlov A. A., Srećković V. A., and Sakan N. M.: 2015., J. Astrophys. Astron., 36(4):0.

Ignjatović Lj. M., Mihajlov A. A., Sakan N. M., Dimitrijević M. S., and Metropoulos A.: 2009., Mon. Not. R. Astron. Soc., 396(4):2201–2210.

Soler J.M., Artacho E., Gale J.D., Garcia A., Junquera J., Ordejon P., Sanchez-Portal D., "The SIESTA method for ab initio O(N) materials simulation", Jour. Phys.: Condens. Matter, 14, 2745-2779 (2002).